Dielectric functions and optical bandgaps of high-K dielectrics by far ultraviolet spectroscopic ellipsometry

Elizabeth Cicerrella
B.S. University of Portland, 1999
M.S. Rensselaer Polytechnic Institute 2002

A dissertation submitted to the faculty of the
OGI School of Science & Engineering
at Oregon Health & Science University
in partial fulfillment of the
requirements for the degree
Doctor of Philosophy
in
Electrical Engineering

March 2006

The dissertation "Dielectric functions and optical bandgaps of high-K dielectrics by far ultraviolet spectroscopic ellipsometry" by Elizabeth Cicerrella has been examined and approved by the following Examination Committee:

John Freeouf
Professor
Thesis Research Adviser

Rajendra Solanki
Professor

Jack McCarthy
Assistant Professor

Shankar Rananavare
Research Associate Professor
Portland State University

Andres La Rosa
Assistant Professor
Portland State University

Acknowledgements

It has been my pleasure to work with my advisor, John Freeouf. During the years his input and guidance has reshaped me as an engineer profoundly. I would also like to acknowledge that this material is based upon work supported by the National Science Foundation under Grant No. 0218288. I would like to thank our collaborators Professor D.G. Schlom and Lisa Edge at Pennsylvania State University, and also Oak Ridge National Laboratories for providing many of the samples.

Contents

List of Tables

List of Figures

Abstract

Dielectric functions and optical bandgaps of high-K dielectrics by far ultraviolet spectroscopic ellipsometry

Elizabeth Cicerrella

Supervising Professor: John Freeouf

A far ultraviolet (UV) spectroscopic ellipsometer system working up to 9 eV has been developed and applied to characterize high-K-dielectric materials. These materials have been gaining greater attention as possible substitutes for SiO_2 as gate dielectrics in aggressively scaled silicon devices. The optical properties of representative high-K bulk crystalline, epitaxial, and amorphous films, were investigated with far UV spectroscopic ellipsometry and some by visible-near UV optical transmission measurements. Optical dielectric functions and optical band gap energies for these materials are obtained from these studies. The spectroscopic data and results provide information that is needed to select viable alternative dielectric candidate materials with adequate band gaps, and conduction and valence band offset energies for this application, and additionally to provide an optical metrology for gate dielectric films on silicon substrates. For materials with anisotropic structure such as single crystal $DyScO_3$ and $GdScO_3$ an analysis process was developed to determine the optical constant tensor.

Chapter 1.

Ellipsometry

1.1 Historical Origins

Ellipsometry has a long history in science and technology. The first pioneer in this field was Paul Drude in the late 1800s. In his early work he applied the equations of Fresnel to determine why the reflectance of p-polarized light from water didn't go to zero at Brewster's angle as expected[1]. Drude provided not only the theoretical background for ellipsometry but he also produced the first experimental results[2]. By using the null method he determined the optical properties of 18 metals[3], including Sb_2S_3, an orthorhombic crystal. His results are in close agreement with current known values[4-6]. This period of time when ellipsometric technology was limited to manual null ellipsometer was what some call the 'dark ages' of ellipsometry[7-9]. But these 'dark ages' did produce the basic principles of ellipsometry. By the use of Maxwell's equations, Drude showed that the real and imaginary components of the dielectric function could be determined by the polarization dependence of non-normal incidence reflectance. Both the magnitude and the phase of light reflected from a surface depend on the polarization of light: the incident linearly polarized light is converted to elliptically polarized light depending on the dielectric function of the material it is reflected from. Therefore if you can measure the change in polarization of the light reflected from the material you can determine the dielectric function of the material. The basic schematic is illustrated in Figure 1. The linearly polarized incident light with electric field components J_{ip} and J_{is}, which represent the components parallel and perpendicular to the plane of incidence, is reflected from the surface at angle N. The reflected light is elliptically polarized with electric field components J_{rp} and J_{rs}, which represent the components parallel and perpendicular to the plane of

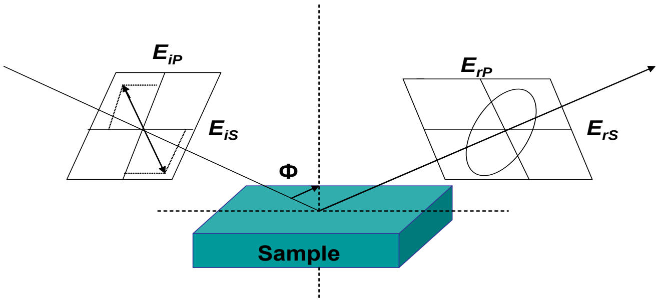

Figure 1: Ellipsometry Schematic

propagation. The elliptically polarized electric field components are usually out of phase with each other.

From Drude up until about 1975 manual null ellipsometry was the dominant technology. Some important results that came out of this time would be Tronstad's application of ellipsometry to electrochemistry in 1933[10], and also Kent and Lawson's first photometric instrument in 1937[11]. The photometric instrument reportedly operated in a pseudo null mode with a rotating analyzer.

By adjusting the compensator and polarizer they produced circularly polarized light on the reflection from the sample. By rotating the analyzer at 40Hz, and amplifying the output of the photocell detector they could detect the pseudo null condition through the 80 Hz components on a pair of headphones.

The term ellipsometry was not used until Rothen in 1945 introduced it[12], and the first paper written with the term ellipsometry was not published until 1958[13]. The first Ellipsometry Conference took place in Washington D.C. in 1963. The Proceeding[14] comprised three review papers, five papers on instrumentation and calculation methods, and 11 papers dealing with various applications.

The modern era begins approximately in the mid 70's; in this era photometric designs were implemented. Designs were primarily rotating-polarizer (RPE), and rotating-analyzer (RAE) ellipsometers, though there were also photoelastic-modulator (PEM) and rotating-compensator (RCE) ellipsometers. The first rotating-compensator polarimeter used for ellipsometric applications was developed by Hauge and Dill in 1975[15]. But the addition of another wavelength-dependent element besides the sample increased the complexity of calibration and data analysis, and an absence of enhanced diagnostic power repressed widespread application. The configuration however is gaining interest as the power of PC's to handle the requisite data analysis becomes clear, and applications to semiconductor technology are reported as in a recent Opsal paper on broadband spectroscopic applications[16]. In regards to the photoelastic modulator designs, a great deal of work has been done on phase-modulated ellipsometers[17-20] which rely on a PEM instead of a rotating compensator. But with the high modulation frequency (50 kHz) of the PEM, the design is too fast to be used with semiconductor array detectors.

In 1973 a major advance took place simultaneously by Hauge and Dill at IBM[21], and Aspnes at Bell Laboratories[22]. They both developed a fully digital rotating analyzer system. The new RAE was able to evaluate sample cleaning in real time, which made it a perfect fit for the time. The new systems were also able to avoid the Kramers-Kronig transformations required in reflectometry, and were more rapid and automated than the earlier null systems, easing the way for spectroscopic studies. This new technology has dominated the field for 30 years.

1.2 Measurement Technique

1.2.1 Ellipsometry

Ellipsometry measures two values, Psi and Delta which describe the polarization change of the light beam after interaction with the sample. Psi and Delta are related to the ratio of Fresnel reflection coefficients, Rp and Rs for p- and s- polarized light. The Fresnel reflection coefficients are described as the convergence of an infinite series of multiple reflections. As shown in Figure 2 a light beam experiences multiple reflections in a thin film which lead to an infinite series for transmitted and reflected light. Where the total Reflectance is equal to an infinite series:

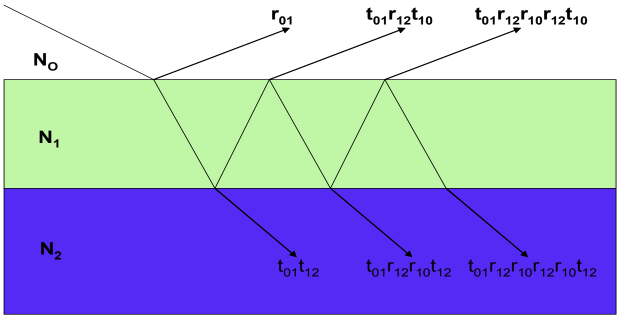

Figure 2: multiple reflections of light beam

$$r_{tot} = r_{01} + t_{01}r_{12}t_{10}e^{-2iT} + t_{01}\, r_{12}\, r_{10}\, t_{10}e^{-4iT} + \ldots \qquad (1)$$

with T being the thickness of the film:

$$T = 2\pi(d_1/\lambda)n_1\cos\theta_1 \qquad (2)$$

The infinite series converges into Fresnel Reflection Coefficients:

$$R_p = (\, r_{p01} + r_{p12}e^{-2iT}\,)/(\, 1 + r_{p01}r_{p12}e^{-2iT}\,) \qquad (3)$$

$$R_s = (\, r_{s01} + r_{s12}e^{-2iT}\,)/(\, 1 + r_{s01}r_{s12}e^{-2iT}\,)$$

These coefficients are related to the ellipsometric parameter Psi and Delta in the following way:

$$\rho = \tan(\Psi)e^{i\Delta} = R_p/R_s \quad (4)$$

Since ellipsometry measures ratios it can be very accurate and reproducible. The measurement provides two data points per measurement, since the ratio is a complex number and therefore contains phase information (delta). This means extra information is obtained at each wavelength as compared with conventional reflectivity measurements which measure a single intensity value.

1.2.2 Generalized Ellipsometry

The wave vectors of the incident and emerging waves define the plane of incidence Figure 3. Here the p and s modes represent the electric wave vector **E**

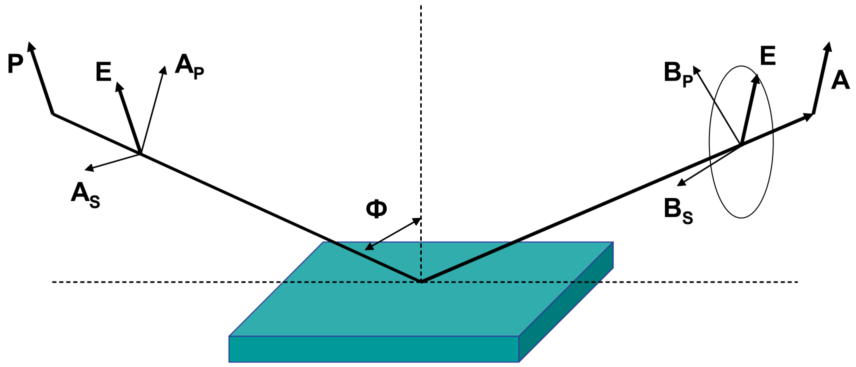

Figure 3. A_P, A_S, B_P, and B_S represent the complex amplitudes of the p and the s modes before and after the sample. P and A are the azimuth angles of the Linear polarizers used in the standard arrangement of RAE.

parallel and perpendicular to the plane of incidence. The Jones matrix **J** is related to the plane waves before and after the optical system by the equation:

$$\begin{pmatrix} B_p \\ B_s \end{pmatrix} = \mathbf{J} \begin{pmatrix} A_p \\ A_s \end{pmatrix} - \begin{pmatrix} j_{pp} & j_{sp} \\ j_{ps} & j_{ss} \end{pmatrix} \begin{pmatrix} A_p \\ A_s \end{pmatrix} \qquad (5)$$

The p and the s modes of the incident and the emerging waves are denoted by Ap, As, Bp, and Bs. In the case of reflection ellipsometry the Jones matrix is equal to the reflection matrix **r**. The matrix elements provide the complex reflectance coefficients for incident light that is either s or p polarized into reflected s- or p-polarized light**.** The complex reflectance ratio is most commonly defined as[23]:

$$\Delta / \tan \Theta \exp(i)) \, / \, ./\Pi, \qquad \Pi = A_p/A_s, \qquad .= B_p/B_s, \qquad (6)$$

For nonvanishing off-diagonal reflection coefficients this depends on the ratio of the incident wave amplitudes Π by way of the Jones reflection matrix:

$$\Delta = ./\Pi = [(r_{pp}/r_{ss}) + (r_{sp}/r_{ss})\Pi^{1}]/[1+(r_{pp}/r_{ss})(r_{ps}/r_{pp})\Pi] \qquad (7)$$

The complex reflectance ratio Δ is written this way to illustrate that it is a combination of three ratios formed by the elements of the Jones reflection matrix. These three ratios are defined as:

$$\begin{aligned} r_{pp}/r_{ss} \, / \, R_{pp} &= \tan \Theta_{pp} \exp(i)_{pp}) \\ r_{ps}/r_{pp} \, / \, R_{ps} &= \tan \Theta_{ps} \exp(i)_{ps}) \qquad (8) \\ r_{sp}/r_{ss} \, / \, R_{sp} &= \tan \Theta_{sp} \exp(i)_{sp}) \end{aligned}$$

Using this result we get the following for the complex reflectance ratio,

$$\Delta = (R_{pp} + R_{sp}\Pi^{-1})/(1+R_{pp}R_{ps}\Pi) \, . \qquad (9)$$

1.2.3 Rotating Analyzer Ellipsometry

To extend Rotating Analyzer Ellipsometry to General Ellipsometry let's refer back to Figure 3. A nonpolarized monochromatic light beam passes through a linear polarizer P and becomes linearly polarized. The light beam is reflected from the sample due to this interaction the light beam generally changes its state of polarization. To determine the new polarization, the light beam is passed through a second linear polarizer which acts as an analyzer. The intensity of the light beam is then measured and this intensity can be expressed as a function of sample properties, the angle of incidence, and the analyzer and polarizer azimuth angle *A* and *P*.

The polarization state transfer can be described by the matrix multiplication below, with $\mathbf{E}^{\mathrm{i}}$ and $\mathbf{E}^{\mathrm{det}}$ indicating the electric field components of the polarizer incident beam and the detected beam.

$$\mathbf{E}^{\mathrm{det}} = \mathbf{R}(\mathrm{A})\ \mathrm{A}\ \vartheta\ \mathrm{A}\ \mathbf{R}(\mathrm{-A})\ \mathrm{A}\ \mathbf{r}\ \mathrm{A}\ \mathbf{R}(\mathrm{P})\ \mathrm{A}\ \vartheta\ \mathrm{A}\ \mathbf{R}(\mathrm{-P})\ \mathrm{A}\ \mathbf{E}^{\mathrm{i}}. \tag{10}$$

The projection matrix of the linear polarizer ϑ, and the rotation matrices are defined as:

$$\vartheta = \begin{pmatrix} 1\ 0 \\ 0\ 0 \end{pmatrix} \qquad \mathbf{R}(\forall) = \begin{pmatrix} \cos\alpha & -\sin\alpha \\ \sin\alpha & \cos\alpha \end{pmatrix} \tag{11}$$

The optical properties are characterized by the Jones reflection matrix **r**,

$$\mathbf{r} = \begin{pmatrix} r_{pp} & r_{sp} \\ r_{ps} & r_{ss} \end{pmatrix} \tag{12}$$

The analyzer is kept at a constant angular frequency A = Σ*t*. Now equation (6) becomes:

$$\begin{pmatrix} E_{\mathrm{p}} \\ E_{\mathrm{s}} \end{pmatrix}^{\mathrm{det}} - E_p{}^{i} \begin{pmatrix} \mathrm{R}_1 \cos \Sigma\, t + \mathrm{R}_2 \sin \Sigma\, t \\ 0 \end{pmatrix} \tag{13}$$

Where:

$$R_1 = r_{pp} \cos P + r_{sp} \sin P, \qquad (14)$$
$$R_2 = r_{ps} \cos P + r_{ss} \sin P.$$

After Fourier analysis on the time-dependent intensity with respect to the analyzer angular frequency, the only nonvanishing Fourier coefficients become ∀ and ∃ which are defined as:

$$I\,(\,\Sigma\, t\,) = I_o\{1 + \forall \cos 2\Sigma t + \exists \sin 2\Sigma t\}\ , \qquad (15)$$

with

$$\forall \;/\; \frac{(*R_1*^2 - *R_2*^2)}{(*R_1*^2 + *R_2*^2)}$$
$$\exists \;/\; \frac{(\bar{R}_1\bar{R}_2 + R_2R_1)}{(*R_1*^2 + *R_2*^2)} \qquad (16)$$

The overbar represents the complex conjugate. For systems with diagonal Jones matrices Equations (6)-(12) simplify and Equation (12) can be directly applied to Equation (2) to determine the complex reflectance ratio Δ in terms of the ellipsometric parameters Θ and):

$$\tan \Theta = \left(\frac{(1 + \forall)}{(1 - \forall)}\right)^{1/2} \tan P$$
$$\cos\,) = \frac{\exists}{(1 - \forall)^{1/2}} \qquad (17)$$

In this example the assumption was that the sample is isotropic therefore the complex reflectance ratio Δ is independent of the polarizer azimuth *P*.

For the general case the Jones matrix of a sample may be nondiagonal. In this case the Fourier coefficients α and β become more complex,

$$\forall = \frac{{*}R_{pp} + R_{sp} \tan P{*}^2 - {*}R_{pp}R_{ps} + \tan P{*}^2}{{*}R_{pp} + R_{sp} \tan P{*}^2 + {*}R_{pp}R_{ps} + \tan P{*}^2}$$

$$\rfloor = \frac{2\mathrm{Re}[(R_{pp} + R_{sp} \tan P) * (R_{pp} R_{sp} + \tan P)]}{{*}R_{pp} + R_{sp} \tan P{*}^2 + {*}R_{pp}R_{ps} + \tan P{*}^2} \qquad (18)$$

where Re[] represents the real part of a complex number. The general case of nondiagonal Jones matrix elements will be discussed more the anisotropic chapter.

1.3 Experimental Equipment: Spectroscopic Ellipsometer

1.3.1 System atmosphere

A custom fabricated far UV spectroscopic ellipsometer with rotating analyzer was used for the characterization of the high-K dielectric materials. A schematic of the far UV spectroscopic ellipsometer system is shown in Figure 4.

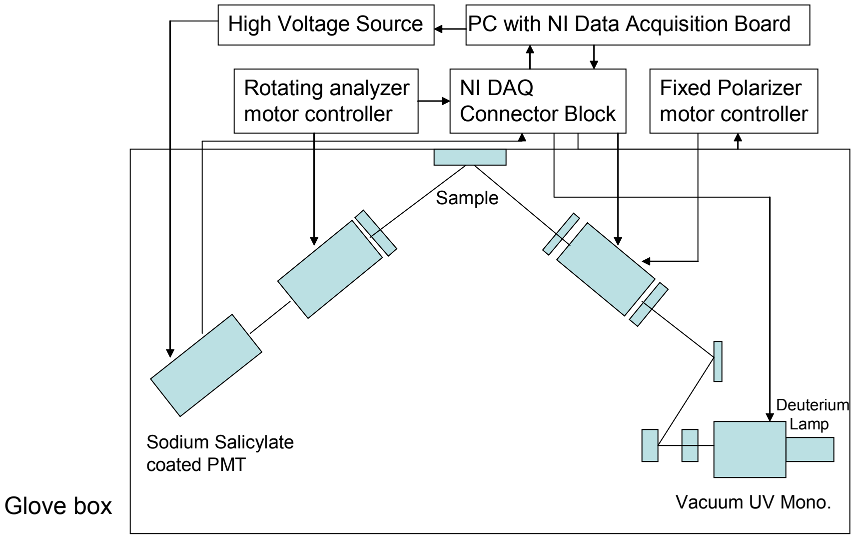

Figure 4: Far UV Block Diagram

Since oxygen and its radicals have absorption bands below approximately 190 nm it was necessary that the system operate in an oxygen free and therefore UV-transparent atmosphere. To achieve this, the system was surrounded by dry nitrogen gas inside a glove box.

1.3.2 Optical System

The optical components and lamp were also selected for UV use. All mirrors were coated with MgF_2, and the polarizers were made from MgF_2 Rochon prisms. Also selected were a deuterium lamp (3-9 eV) with a MgF_2 window as the light source, and a vacuum UV monochromator. Since the photomultiplier tube (PMT) will only detect light in the visible spectrum, the window of the PMT was coated with sodium salicylate[24,25] to convert the UV light to fluorescent light in the visible spectrum. The Rochon prisms used for the polarizer and analyzer prisms were constructed by optically contacting the prism halves[26]. Therefore they only produce minor deviations of the transmitted beam. Rochon prisms are in effect beam-splitting devices, so it was therefore essential to provide spatial filtering of the unwanted beam in the form of apertures. The apertures were placed after the sample mount and before the PMT to prohibit the unwanted beam from passing to the detector. We found that the aperture openings either needed to be large enough to pass the entire desired beam or else a very small centered cross-section. However intermediate beam obstruction by an aperture led to excessive noise.

During operation the polarizer prism was set to an azimuth of 30 degrees. This angle is found to optimize precision for wide range of substrate materials in RAE systems[27]. The analyzer prism rotates at a mechanical frequency of approximately 1 Hz, which results in a time-dependent flux I(t) incident on the PMT. The variation of the flux has the mathematical form:

$$I(t) = I_0(1 + \alpha \cos 2A + \beta \sin 2A) \tag{19}$$

where

$$A = A_r(t) - A_{rs} \tag{20}$$

The average intensity is represented by I_0; α and β are the normalized Fourier coefficients which describe the phase and relative amplitude of the ac component of the flux incident on the detector; A describes the instantaneous analyzer azimuth angle; $A_r(t)$ and A_{rs} are an experimentally defined analyzer azimuth, and phase angle determined in calibration.

1.3.3 Optical bandpass filters

Bandpass filters designed to transmit a specific waveband were used in many of the measurements to filter unwanted stray light. They are made of many thin layers of dielectric materials, which have differing refractive indices to generate constructive and destructive interference in the transmitted light. In this way optical bandpass filters can be designed to transmit a specific waveband only.

Optical bandpass filters are designed to pass only a specific wavelength range. The range is dependant upon the interference filters lens, and the composition of the thin-film filter material. Optical bandpass filters designed to transmit ultra-violet wavelengths are tuned for use in the 130 nm to 380 nm wavelength range.

In optical bandpass filters, wavelength selection is often based on the property of destructive light interference. Incident light is passed through two coated reflecting surfaces. The distance between the reflective coatings determines which wavelengths will destructively interfere and which wavelengths will be allowed to pass through the coated surfaces. In situations where the reflected beams are in phase, the light will pass through the two reflective surfaces. However, if the wavelengths are out of phase, destructive interference will block most of the reflections, allowing almost nothing to transmit through. In this way, interference filters are able to attenuate the intensity of transmitted light at wavelengths that are higher or lower than desired.

The gap between the two reflecting surfaces houses the spacer, a thin film of dielectric material. The spacer has a thickness of one-half of the desired peak transmission wavelength, as opposed to the two outer, reflective layers, which are usually a quarter wave thick. This entire layer is often referred to as the stack, which in conjunction with the spacer formed a bandpass filter. The width of the bandpass can be adjusted based upon the number of stacks present within the interference filter.

1.4 Calibration Procedure

The calibration procedure used was first described by Aspnes[22] in 1974. In his method the calibration is done in the polarizer-sample-rotating analyzer configuration. The sample is mounted and aligned for normal measurement, therefore there is no adjustment of the ellipsometer needed besides a stepping motor attached to the fixed polarizer rotator.

We will look at Aspens approach without the optical activity corrections, which do not apply to MgF_2-based prisms. Starting with the irradiance found in Eq.(19), we convert this to an electrical signal assuming that the detector is linear, and taking into account that the noise reduce filtering will cause a frequency-dependent gain and phase shift. This leads to an electrical signal of

$$I_e(t)=I_{eo}\{1+\eta^{-1}\alpha\cos2[A_r(t)-A_r-\varphi/2]+\eta^{-1}\beta\sin2[A_r(t)-A_{rs}-\varphi/2]\} \qquad (21)$$

with η-1 being the attenuation of the ac component of the signal voltage with respect to the ac component of the intensity. I_{eo} represents the average irradiance, α and β are the normalized Fourier coefficients, $A_r(t)$ and A_{rs} are experimentally defined analyzer azimuth, and a phase angle found in calibration. The ellipsometric angles Ψ and Δ are related to the normalized Fourier coefficients and the polarizer azimuth in the form:

$$\tan\Psi = \left(\frac{(1+\forall)}{(1-\forall)}\right)^{1/2} |\tan(P - P_s)| \qquad (22a)$$

$$\cos(\Delta) = \frac{\exists}{(1-\forall)^{1/2}} \qquad (22b)$$

It should be noted that Eqs. (21), (22a), and (22b) show theoretical relationships that lead to predictions of the ellipsometer performance. The normalized Fourier coefficients α and β which allow us to determine Ψ and Δ, can not be determined due to the number of unknown quantities η, $(A_{rs} + \varphi/2)$, and P_s. However if we let α' and β' be the measured normalized Fourier coefficients where:

$$I'(t) = I'_o \, (1 + \alpha' \cos\omega t + \beta' \sin\omega t) \tag{23}$$

Also note that $Ar(t) = \omega t$ which is defined as the azimuth of the analyzer transmission axis. The unknown parameters from equation (21) can be determined by equating Eqs (23) and (21) in the following calibration procedures. $I'(t)$ shows maximum modulation $(\alpha'^2 + \beta'^2 = 1)$ when the wave emergent from the sample is linearly polarized. When the emergent wave deviates from this 100% ideal modulation it is defined as the "residual function" R(p)[23]

$$\begin{aligned} R(p) &= 1 - (\alpha'^2 + \beta'^2) \\ &= 1 - \eta^{-2}(\alpha^2 + \beta^2) && (24a) \\ &= (1 - \eta^{-2}) + \eta^{-2}\{\sin 2\Psi \sin\Delta \sin 2(P - P_s)/[1 - \cos 2\Psi \cos 2(P - P_s)]\}^2 \\ & && (24b) \end{aligned}$$

$$\approx (1 - \eta^{-2}) + \eta^{-2}(2\sin\Delta\cot\Psi)^2 \times (P - P_s), \ \Vert P - P_s| \ll 1 \tag{24c}$$

To obtain Eq. (24b) the inverted forms of Eqs. (22a) and (22b) where used.

The calibration is then carried out by measuring the normalized Fourier coefficients α' and β' for a series of closely spaced polarizer azimuth angles P near P_s. A range of ± 5 degrees is taken around the estimated P_s and measurements are taken every .5 degrees for a total of 20 measurements. Using the measured values of α' and β' the residual function R(p) is fit with a least-squares regression to the quadratic formula of Eq. (24c). The optimal polarizer position P_s is produced by finding the value of P so that the best-fit function is minimum, and similarly η is found from the value of $R(P_s)$ for the best fit.

To determine the combined calibration angle $A_{rs} + \varphi/2$, and therefore the "phase function" $\Theta(P)$ Eqs. (23) and (21) are once again equating with respect to the phases. This gives the phase functions as

$$\Theta(P) = [\tan^{-1}(\beta'/\alpha')]/2$$

$$= (A_{rs} + \varphi/2) + [\tan^{-1}(\beta/\alpha)]/2 \qquad (25a)$$

$$= (A_{rs} + \varphi/2) + (\tan^{-1}\{\sin2\Psi\cos\Delta\sin2(P-P_s)/[\cos2(P-P_s)-\cos2\Psi]\})/2 \qquad (25b)$$

$$\approx (A_{rs} + \varphi/2) + (\cot\Psi\cos\Delta)(P-P_s), \quad |P - P_s| \ll 1. \qquad (25c)$$

The measured values α' and β' are used to determine the measure phase function $[\tan^{-1}(\beta'/\alpha')]/2$, which is then fit to a linear relationship evaluated at the known value of $P = P_s$ to find the combined calibration angle $A_{rs} + \varphi/2$.

During operation a determined fixed polarizer angle is used which yields a single pair of measured Fourier coefficients α' and β', and the information deduced of η and $A_{rs} + \varphi/2$ from the calibration provides the tools necessary to determine the normalized Fourier coefficients α and β using the following relationships:

$$\alpha = \eta[\alpha'\cos2(A_{rs} + \varphi/2) + \beta'\sin2(A_{rs} + \varphi/2)] \qquad (26a)$$

$$\beta = \eta[-\alpha'\sin2(A_{rs} + \varphi/2) + \beta'\cos2(A_{rs} + \varphi/2)] \qquad (26b)$$

To determine the ellipsometric angles Ψ and Δ, the Fourier coefficients α and β along with P_s and the fixed polarizer angle P from Eqs. (21) and (23) are used.

There is variation of the orientation of the plane of incidence due to slight deviations in the alignment from one sample to the next. Therefore calibration is done from each sample after it is mounted and aligned.

1.5 Physical Models

1.5.1 Modeling

To study materials of unknown dielectric responds we would either use a model for fitting or use known dielectric data from a similar material as a starting point.

1.5.2 Sellmeier

The Sellmeier Formula was developed by Sellmeier in 1871. It is suitable for modeling transparent materials and transparent dielectric materials. The optical constants for the Sellmeier material are defined in the following equations:

$$n(8) = (A_n + B_n\, \lambda^2/(\lambda^2-C_n^2))^{1/2} \qquad (27)$$

$$k(8) = 0$$

The units of C_n are the same as the wavelength either nm or µm. Since $k = 0$; n is restricted to be greater than or equal to 1. With this restriction we can conclude the following conditions of the coefficients:

$$8 = C_n / \surd(1 + (B_n /(A_n - 1))) \qquad (28a)$$

$$A_n \geq 1 - B_n \qquad (28b)$$

$$8 \neq C_n \qquad (28c)$$

1.5.3 Lorentz Oscillator Model

The Lorentz Oscillator Model is suitable for modeling of both semiconductor and crystalline materials (lattice dispersion). When restatrahlen contributions of the lattice is important the Lorentz Oscillator Model gives a superior approximation as compared to other models. For example when $\omega_T \leq \omega \leq \omega_L$, where ω_L and ω_T are the angular frequencies of the longitudinal and transverse optical phonons. The general equation used in the modeling is:

$$\gamma =\gamma_4[1 + 3\, A_j^2 / \{(E_{center})_j^2 - E^2 + iE<_j\}] \qquad (29)$$

Where γ_4 represent the high frequency lattice dielectric constant of the material. The center energy of each oscillation is shown as $(E_{center})_j$ and is given in eV. The physical meaning described by the center energy depends on the material studied and the spectral range. With semiconductors the center energy is associated to the transverse phonon frequency. The amplitude A_j or strength of each oscillation for semiconductors is associated with the transverse and longitudinal phonon frequencies:

$$\text{Amplitude} = \sqrt{(\omega_L^2 - \omega_T^2)} \tag{30}$$

The broadening of the "j" oscillator is represented by the vibration frequency ν in eV.

1.5.4 EMA

This model allows one to find layers that may be a mixture of two other layered materials. It also can be used to determine if there is a surface roughness layer by mixing the top most layer with Void. There are three different EMA models:

Maxwell-Garnett

$$(\varepsilon - \varepsilon_1)/(\varepsilon + y\varepsilon_1) = \sum f_j (\varepsilon_j - \varepsilon_1)/(\varepsilon_j + y\varepsilon_1) \tag{31}$$

Bruggeman Model

$$\sum f_j (\varepsilon_j - \varepsilon)/(\varepsilon_j + y\varepsilon) = 0, \tag{32}$$

Lorentz-Lorenz Model

$$(\varepsilon - 1)/(\varepsilon + y) = \sum f_j (\varepsilon_j - 1)/(\varepsilon_j + y). \tag{33}$$

In these EMA models there is a screening factor or depolarization factor which represents the microstructure of the mixtures in the material. The parameter y in the above equations is related to the screening factor in the following way:

$$y = (1/\text{Screening factor}) - 1. \tag{34}$$

The screening factor has a range between 0 and 1. For a spherical microstructure it would be set to 1/3. At the extremes it has a value of 1 for a flat disk, and a 0 for a columnar microstructure.

Chapter 2
Transmission

2.1 Basic Theory

For transmission measurements light is incident on the sample and the transmitted light is measured as a function of wavelength. The transmittance *T* of a sample for light incident normal to the sample surface is given as

$$T = \frac{(1 - R)^2 e^{-\alpha d}}{1 + R^2 e^{-2\alpha d} - 2Re^{-\alpha d}\cos(\gamma)}. \tag{35}$$

Where *R* and α are the reflection and absorption coefficients, and $\gamma = 4\pi n_1 d/\lambda$, with n_1 as the real part of the complex refractive index ($n_1 - jk_1$). The reflectance *R* is given by

$$R = \frac{(n_o - n_1)^2 + k_1^2}{(n_o + n_1)^2 + k_1^2}. \tag{36}$$

Our measurements are external, therefore we do not correct for reflective losses. The extinction coefficient k_1 is related to the absorption coefficient by the equation

$$\alpha = \frac{4\pi k_1}{\lambda} \tag{37}$$

The absorption coefficient can be used to determine the semiconductor band gap by measuring the absorption coefficient as a function of the photon energy. If the incident light has higher energy that the band gap of the material then the light will be absorbed. For incident photon energies less than the band gap energy the semiconductor is transparent ($\alpha = 0$) and thus the transmittance becomes

$$T = \frac{(1-R)^2}{1 + R^2 - 2R\cos(\gamma)} \tag{38}$$

The "cos" term can be written in terms of frequency, so that cos(γ) = col(f/f_1) with $f = 2\pi/\lambda$. The characteristic spatial frequency is given as $f_1 = 1/2n_1d$.

2.2 Instrumentation

The transmission measurements were taken on a Lambda 9 spectrometer. The instrumentation is based on the use of a monochromator, a basic schematic is seen in Fig.(5). The source is focused onto the narrow entrance slit. The light is then collimated (made parallel) by a concave mirror so that parallel light is incident upon the plane grating.

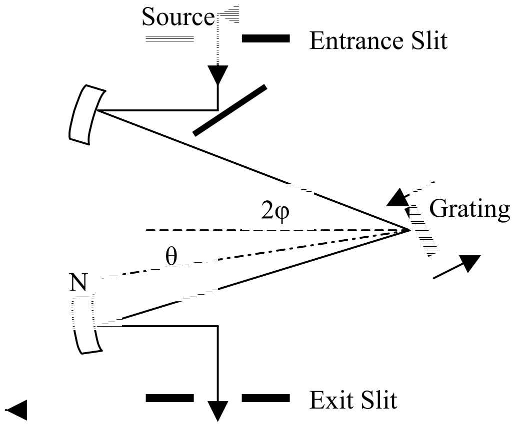

Figure 5: Monochromator illustration

The grating then disperses the light breaking it into its spectral components. The dispersed light then passes through the exit slit, and only the wavelengths that pass through this slit will be incident on the sample. The entrance and exit slits control the spectral resolution, therefore the narrower the slit, the narrower the wavelength range that reaches the detector. The wavelength of the incident light is controlled by the angular position of the grating.

Chapter 3

Dielectric Function Theory

One of the material properties we extract from the obtained ellipsometric data is the dielectric response of the material. Therefore in this chapter we will discuss the background for a theoretical model of the dielectric function. This material was presented in a graduate course by Prof. S. Nayak at Rensselaer Polytechnic Institute[28]. The first section will review the relations between different optical properties. The second section will cover the allowed energy states for an electron in a periodic crystal in other words the band structure. The third section will discuss the effective mass approximation and its use in interpreting different perturbations to the ideal one electron states given by band structure calculations. The last section will correlate band structure to the dielectric function.

3.1 Optical Properties

The optical properties discussed most regularly are the complex index of refraction (ň), the complex dielectric function (ĕ), the absorption coefficient (α), and the complex wave propagation vector (**k**). If we look at the macroscopic Maxwell equations and their solution for plane waves propagating through a medium we see that all these properties are related. The macroscopic Maxwell equations are:

$$\bigtriangledown \bullet \mathbf{D} = 4\pi\rho \qquad \bigtriangledown \times \mathbf{H} = \frac{4\pi\mathbf{J}}{c} + \frac{1}{\boldsymbol{c}}\frac{\delta\mathbf{D}}{\delta t}$$

$$\bigtriangledown \cdot \mathbf{B} = 0 \qquad \bigtriangledown \times \mathbf{E} + \frac{1}{\boldsymbol{c}}\frac{\delta\mathbf{B}}{\delta t} = 0 \qquad (39)$$

where **E** and **H** are the electric and magnetic field, **B** is the magnetic induction, **D** is the electric displacement, and **J** is the current density vector. The free charge density is represented by ρ, and the *c* represents the speed of light in vacuum.

The ancillary definitions are as follows:

$$\mathbf{D} = \varepsilon(\omega)\mathbf{E} = \mathbf{E} + 4\pi\mathbf{P} = [1 + 4\boldsymbol{\pi\chi(\omega)}]\mathbf{E}$$

$$\mathbf{B} = \mu(\omega)\mathbf{H} \qquad (40)$$

P represents the averaged polarization or average dipole, and ε(ω) and μ(ω) are the Fourier transforms of the real values ε(*x,t;x',t'*) and μ(*x,t;x',t'*). However ε(ω) and μ(ω) are complex, such that:

$$\varepsilon(\omega) = \varepsilon_1(\omega) + i\varepsilon_2(\omega) \qquad (41)$$

If the imaginary part of ε(ω) which is ε_2 returns a non-zero value that indicates that **D** is out of phase with **E**.

If we take the example of an infinite material with no free charge or current (ρ = 0, **J** = 0), then Eq. (39) becomes the familiar wave equation for **E**:

$$\mathbf{E} = \mathbf{E}_0 e^{i\boldsymbol{\kappa}\cdot\mathbf{r}-i\omega t} \qquad (42)$$

where the electric field is the real part of Eq. (42), **r** is the position vector, and $\mathbf{E}_0$ is the electric field intensity at **r** = 0, *t* = 0 and

$$||\mathbf{k}(\omega)|| = k(\omega) = k_1 + k_2 = \sqrt{[\varepsilon(\omega)\mu(\omega)]}\ \frac{\omega}{c} \qquad (43)$$

where κ is in the same direction as the traveling wave. The velocity *v* of the wave is:

$$v(\omega) = c/\sqrt{[\varepsilon(\omega)\mu(\omega)]} \qquad (44)$$

The complex velocity can be broken into its real part, the normal phase velocity of propagating wave, and the imaginary part, which represents the exponential damping of the wave with time as the wave propagates through the medium.

Using Eq.(40) we define the complex index of refraction as:

$$n(\omega) = \mathrm{n}(\omega) + i\kappa(\omega) = c/v(\omega) = \sqrt{[\varepsilon(\omega)\mu(\omega)]} \qquad (45)$$

To find the absorption coefficient consider the time averaged energy density, *u*, of a wave traveling into the material[29].

$$u \approx \|\mathbf{E}\|^2 = \|\mathbf{E}_0\|^2 e^{-2k_2 d} \qquad (46)$$

The distance the wave has traveled into the medium is represented by *d*. The absorption coefficient,α, and the skin depth, δ, can be determined from Eq.(46) and are found to be:

$$\alpha = 1/\delta = 2k_2 \qquad (47)$$

Now we can consider the relationship between the imaginary part of the dielectric function and the conductivity for low frequencies. Following Ohm's law:

$$\mathbf{J} = \sigma\mathbf{E} \qquad (48)$$

and letting ε_0 correspond to the dielectric function neglecting any effects of the conductivity, then the Maxwell-Ampère equation is written as:

$$\nabla \times \mathrm{H} = \frac{4\pi}{c}\sigma\mathbf{E} + \frac{-i\omega\varepsilon_0(\omega)}{c}\mathbf{E} = -\left(\frac{i\omega}{c}\varepsilon_0(\omega) + i\right)\frac{4\pi\sigma\mathbf{E}}{\omega} \qquad (49)$$

If we take the terms in parentheses on the right hand side of Eq.(49) as a result of the dielectric properties of the medium rather than due to Ohm's law then we determine:

$$\varepsilon(\omega) = \varepsilon_0(\omega) + i\frac{4\pi\sigma}{\omega} \qquad (50)$$

Since all of the dissipation of the electric field is due to the conductivity of the material at low frequencies then, as expected, $\varepsilon_0(\omega)$ is real. Therefore:

$$\varepsilon_2(\omega \approx 0) = \frac{4\pi\sigma}{\omega} \qquad (51)$$

As shown in Eq.(51) the dielectric function of a conducting medium has a singularity at $\omega = 0$.

Assuming we have non-magnetic materials ($\mu = 1$), we can derive several relations between the optical functions using Eqs.(41), (43), (44), (47) and the relation for the speed of light $c = \omega\lambda/2\pi$.

$$\varepsilon_1 = n^2 - \kappa^2$$
$$\varepsilon_2 = 2n\kappa$$
$$n = \sqrt{\frac{\sqrt{(\varepsilon_1^2 + \varepsilon_2^2)} + \varepsilon_1}{2}}$$
$$\kappa = \sqrt{\frac{\sqrt{(\varepsilon_1^2 + \varepsilon_2^2)} + \varepsilon_1}{2}} \qquad (52)$$
$$k = \frac{n\omega}{c}$$
$$\alpha = \frac{1}{\delta} = 2k_2 = \frac{2\omega\kappa}{c} = \frac{4\pi\kappa}{\lambda} = \frac{2\pi\varepsilon_2}{n\lambda} = \frac{\omega\varepsilon_2}{nc}$$

3.1.1 Band Structure/Critical Points

The allowed energy states of a material as a function of the wave vector **k** is the band structure. Solving the problem of the crystalline band structure has been a subject of investigated for years. Such approaches include **k·p**[30], tight binding, and semi-empirical pseudopotential[31,32]. To illustrate the fundament principles of this problem we will look at the adiabatic approximation which follows that the atomic nuclei and core electrons are at rest in comparison to the valence electrons. We will also apply the mean-field approximation which assumed the same average potential $V(\mathbf{r})$ is felt by each valence electron. By utilizing all these approximations, the Schrödinger equation is indistinguishable for each electron and is written as:

$$H_{1e}\Psi_{l,\mathbf{k}}(\mathbf{r}) = \left(-\frac{\hbar^2\nabla^2}{2m_0} + V(\mathbf{r})\right)\Psi_{l,\mathbf{k}}(\mathbf{r}) = E_{l,\mathbf{k}}\,\Psi_{l,\mathbf{k}}(\mathbf{r}) \qquad (53)$$

The one-electron Hamiltonian is represented by H_{1e}. The wavefunction and energy for a particular eigenstate are expressed as $\Psi_{l,\mathbf{k}}(\mathbf{r})$ and $E_{l,\mathbf{k}}$, with the band index l and the wavevector $\mathbf{k}$. The other terms $V(\mathbf{r})$, and m_0 are the crystal periodic potential and the free electron mass. Because of the lattice periodicity the solutions are required to be Bloch functions[32], such that:

$$\Psi_{l,\mathbf{k}}(\mathbf{r}) = e^{i\mathbf{k}\cdot\mathbf{r}} u_{l,\mathbf{k}}(\mathbf{r}) \tag{54}$$

where the periodic function $u_{l,\mathbf{k}}(\mathbf{r})$ has the same periodicity as $V(\mathbf{r})$ according to the lattice, this is a consequence of the translation symmetry of the crystal. However, for amorphous materials there is no such long-range order so the Bloch function is inapplicable this will be discussed further in the Amorphous Material section. For a crystalline material, if $\mathbf{R}$ is the lattice vector then $u_{l,\mathbf{k}}(\mathbf{r} + \mathbf{R}) = u_{l,\mathbf{k}}(\mathbf{r})$. Next we will utilize the reduced zone scheme, which takes into account that both $\mathbf{k}$ and $\mathbf{k} + \mathbf{G}$ will satisfy Eq.(54) because of the translational symmetry of the crystal. With $\mathbf{G}$ being the reciprocal lattice vector, such that $e^{i\mathbf{G}\cdot\mathbf{R}} = 1$. By replacing $\mathbf{k}$ by $\mathbf{k}' = \mathbf{k} - \mathbf{G}$ with $\mathbf{G}$ limiting $\mathbf{k}'$ to the first Brillouin zone, every $\mathbf{G}$ now corresponds to a different band indicated by the band index l.

With semi-empirical approaches, energy gaps, oscillator strength, and other experimental data are used as input parameter to determine approximate solution to Eq. (53). The semi-empirical pseudopotential method takes advantage of the fact that since $V(\mathbf{r})$ is a periodic function and therefore can only have Fourier components corresponding to reciprocal lattice vectors, then it can be expressed in terms of a few Fourier coefficients corresponding to the shortest reciprocal lattice vectors. Since the valence electrons are forbidden from the regions nearest to the nuclei by Pauli's exclusion principle, this approximation is viable. Consequently, the potential can be approximated with a weak slow varying "effective potential" or pseudopotential for the valence electrons. Note that this approach fails for the core electron states.

A direct optical interband transition is described as an excitation of an electron from a valence band to a conduction band with only an electron and a photon. The direct optical interband transitions are the main factor in determining the structure of the optical functions. The photon involved in the direct transition has very little momentum compared to the size of the Brillouin zone, therefore the electron and hole states have nearly identical $\mathbf{k}$ values and this process is described as a vertical transition.

An indirect transition involves electron, photon, phonon interactions. Unlike the photons, the phonons have momentum comparable to the Brillouin zone, and therefore the interaction can involve electron states of different **k** values. Because of this, the indirect transitions typically have a much smaller effect on the dielectric function than the direct transitions.

The **k·p** approach treats band structure near a critical point by perturbation theory for small **k**. In this method the electronic band structure is just a plot of the electron energies in Eq.(53) as a function of **k**. By substituting Eq.(54) into Eq.(53) we get:

$$\left(\frac{p^2}{2m_0} + V(\mathbf{r}) + \frac{\hbar}{m_0}\mathbf{k}\cdot\mathbf{p}\right) u_{l,k}(\mathbf{r}) = \left(E_l(\mathbf{k}) - \frac{\hbar^2 k^2}{2m_0}\right) u_{l,k}(\mathbf{r}) \qquad (55)$$

with $\mathbf{p} = - i\hbar\ \nabla$. Next treating the **k·p** proportional term as a perturbation we get:

$$H = H_0 + H_1 \qquad (56)$$

with

$$H_0 = \frac{p^2}{2m_0} + V(\mathbf{r})\ , \qquad \mathrm{H}_1 = \frac{\hbar}{m_0}\mathbf{k}\cdot\mathbf{p}$$

at $\mathbf{k}_0 = (0,0,0)$, Eq. (55) will reduce to:

$$\left(\frac{p^2}{2m_0} + V(\mathbf{r})\right) u_{l,0}(\mathbf{r}) = [E_l(0)]\ u_{l,0}(\mathbf{r}) \qquad (57)$$

To find the secular equation for the system from Eq.(55) we use the orthonormality of the $u_{l,\mathbf{k}}$ and Eq.(57) to get:

$$\langle u_{l',\mathbf{k}}|H_1|\ u_{l,\mathbf{k}}\rangle = \left(E_l(\mathrm{k}) - \mathrm{E}_l(0) - \frac{\hbar^2 k^2}{2m_0}\right)\delta_{l,l'} \qquad (58)$$

For simplicity, the Dirac bra-ket notation is used. For Eq.(58) to have solutions the secular determinant must be zero, therefore the standard perturbation results are:

$$E_l(\mathrm{k}) - \mathrm{E}_l(0) - \frac{\hbar^2 k^2}{2m_0} = \langle u_{l',0}|H_1|\, u_{l,0}\rangle + \frac{\hbar^2}{m_0{}^2}\sum \frac{|\langle u_{l',0}|H_1|\, u_{l,0}\rangle|^2}{E_{l'}(0) - E_l(0)} + \ldots \qquad (59)$$

Since H_1 has odd parity the first term on the right hand side of Eq.(59) will be zero, therefore the final result for the energy and effective mass is:

$$E_l(\mathbf{k}) = E_l(0) + \frac{\hbar^2 k^2}{2m_0} + \frac{\hbar^2}{m_0}\sum \frac{|\langle u_{l',0}|H_1|\, u_{l,0}\rangle|^2}{E_{l'}(0) - E_l(0)} + \ldots \qquad (60)$$

solving for the curvature of the *E* versus **k** dispersion curve we find the effective mass tensor:

$$\left(\frac{1}{m^*}\right)_{ij} = \frac{1}{\hbar^2}\frac{\delta^2 E}{\delta k_i \delta k_j} = \frac{1}{m_0}\left(\delta_{ij} + \frac{2}{m_0}\sum \frac{\langle u_{l',0}|p_i|\, u_{l,0}\rangle\langle u_{l',0}|p_j|\, u_{l,0}\rangle}{E_{l'}(0) - E_l(0)}\right) \qquad (61)$$

Examining Eqs.(60) and (61) we see that the wave function $u_{l,0}$ can only couple to another wavefunction $u_{l',0}$ if the matrix element $\langle u_{l',0}|H_1|\, u_{l,0}\rangle$ is nonzero. Therefore when determining the effective mass using Eq.(61) many of the term will become zero due to symmetry. Also the relative importance of the contribution of the *l*’ state to the effective mass of the *l* state is determined by the energy separation $E_{l'}(0) - E_l(0)$.

To make things simpler lets make the assumption that we’re dealing with a two-band model, therefore we only have two bands interacting with each other. From Eq.(58) we’ll define the states as 1 and 2, now the secular determinant comes out as:

$$\det \begin{vmatrix} E_1(0) + \frac{\hbar^2 k^2}{2m_0} - E & \frac{\hbar}{m_0} Pk \\ \frac{\hbar}{m_0} Pk & E_2(0) + \frac{\hbar^2 k^2}{2m_0} - E \end{vmatrix} = 0 \qquad (62)$$

where

$$P = \langle u_{2,k} | \, -i\hbar \, \nabla | \, u_{1,k} \rangle \tag{63}$$

Solving the determinant in Eq.(57) with $E_g = E_1(0) - E_2(0)$ and also assuming $\frac{4\hbar^2P^2k^2}{m_0^2E_g} << 1$ then we find:

$$E_l(\mathrm{k}) = E_l(0)\frac{\hbar^2k^2}{2m_0} \pm \frac{2\hbar^2P^2k^2}{m_0^2E_g} \qquad l = 1,2 \tag{64}$$

As stated previously the effective mass tensor is defined as the E versus **k** dispersion, which in this two band model we see that the effective mass becomes:

$$\left(\frac{1}{m^*}\right)_l = \frac{1}{m_0} \cdot \left(1 + \frac{4P^2}{m_0E_g}\right) \qquad l = 1,2 \tag{65}$$

Therefore, the higher lying state has a lower effective mass while the lower lying state has an increased and possibly negative effective mass. Also note that for a small E_g the effect of m^* is greater.

It is clear that without the two band simplification that band structure calculations can be very difficult. The crystalline symmetry does simplify the equations, however early empirical band structure calculations were heavily based on experimentally determined data[33]. With the use of extended computer calculations, realistic first principles calculations of band structures have been determined[34,35].

3.1.2 Envelope Function

This section will illustrate the usefulness of the effective mass equations defined in the previous section. We show that the effective mass definition, along with a few approximations, will lead to a straightforward way of evaluating the small perturbation effects near critical points in the band structure with the use of envelope functions.

The envelope functions can only be applied to small local perturbations in the crystal potential.

$$H = \frac{-i\hbar^2\nabla^2}{2m_0} + V(\mathrm{r}) + V_p(\mathrm{r}) = H_0 + V_p(\mathrm{r}) \qquad (66)$$

The local perturbation of the crystal potential is represents by $V_p(\mathrm{r})$**.** The final state is found be superposition of the Bloch functions. Since the functions are a complete orthonormal set the final set comes out as:

$$\Psi(\mathbf{r}) = \sum_{l,\mathbf{k}} A_l(\mathrm{k})\Psi_{l,\mathbf{k}}(\mathbf{r}) = \sum_{l,\mathbf{k}} A_l(\mathbf{k})e^{i\mathbf{k}\cdot\mathbf{r}}u_{l,\mathbf{k}}(\mathbf{r}) \qquad (67)$$

Here we are using a reduced zone scheme with the Bloch function $\Psi_{l,\mathbf{k}}(\mathbf{r})$, so that the summation in **k** is over the first Brillouin zone and the different zone-folded bands are referenced by the index *l*.

We are interested in a state near a critical point, $\mathbf{k} = \mathbf{k}_0$. In the limit $V_p(\mathrm{r}) = 0$, the state would reduce to the single Bloch state at $\mathbf{k}_0$ in the band with index $l = 0$. The following approximations should hold for small $V_p(\mathrm{r})$:

$$\mathbf{k} - \mathbf{k}_0 << \frac{\Pi}{a} \qquad (68)$$

$$A_l(\mathbf{k}) \approx \delta_{l,0}\delta_{\mathbf{k},\mathbf{k}0}$$

As expected for a weak $V_p(\mathrm{r})$ we see in the second line of Eq.(68) that the wavefunction $\Psi(\mathbf{r})$ in **k** space is sharply peaked and therefore broad in **r** space. For a shallow dopant, the 0 band would be the highest lying valence band in the case of an acceptor, and the lowest lying conduction band in case of a donor. If we want to examine an exciton we need to look at the state in which a single electron has been excited from the conduction to the valence band. With this the index 0 will refer to the electron hole state near the critical point $\mathbf{k} = \mathbf{k}_0$.

Transfering Eq.(67) to the Dirac bra-ket notation we get:

$$|\Psi(\mathbf{r})\rangle = \sum_{l,\mathbf{k}} A_l(\mathbf{k})|\Psi_{l,\mathbf{k}}(\mathbf{r})\rangle = \sum_{l,\mathbf{k}} A_l(\mathbf{k})e^{i\mathbf{k}\cdot\mathrm{r}}|u_{l,\mathbf{k}}(\mathbf{r})\rangle \qquad (69)$$

By making use of the Hamiltonian from Eq.(66), and the wavefunction in Eq.(69), the Schrödinger equation becomes:

$$\frac{-\hbar^2\nabla^2}{2m_0} + V(\mathrm{r}) + V_p(\mathrm{r}) \sum_{l,\mathbf{k}} A_l(\mathbf{k})|\Psi_{l,\mathbf{k}}(\mathbf{r})\rangle = E\sum_{l,\mathbf{k}} A_l(\mathbf{k})|\Psi_{l,\mathbf{k}}(\mathbf{r})\rangle \qquad (70)$$

With the use of Eq. (66) and the scalar product $\langle\Psi_{l,\mathbf{k}}(\mathbf{r})|$ from the above equation, the Schrödinger equation now becomes:

$$\langle\Psi_{l',\mathbf{k}'}(\mathbf{r})|(\mathrm{H}_0+V_p(\mathrm{r}))\sum_{l,\mathbf{k}} A_l(\mathbf{k})|\Psi_{l,\mathbf{k}}(\mathbf{r})\rangle = E\langle\Psi_{l',\mathbf{k}'}(\mathbf{r})|(\sum_{l,\mathbf{k}} A_l(\mathbf{k})|\Psi_{l,\mathbf{k}}(\mathbf{r})\rangle$$

$$\sum_{l,\mathbf{k}}\langle\Psi_{l',\mathbf{k}'}(\mathbf{r})|(E_l(\mathbf{k}')+V_p(\mathrm{r}))A_l(\mathbf{k})|\Psi_{l,\mathbf{k}}(\mathbf{r})\rangle = \sum_{l,\mathbf{k}} E\langle\Psi_{l',\mathbf{k}'}(\mathbf{r})|(A_l(\mathbf{k})|\Psi_{l,\mathbf{k}}(\mathbf{r})\rangle \qquad (71)$$

where: $\mathrm{H}_0 = \frac{-\hbar^2\nabla^2}{2m_0} + V(\mathbf{r})$

With further reductions this becomes:

$$\sum_{l,\mathbf{k}} A_l(\mathbf{k})E_l(\mathbf{k})\delta_{l,l'}\delta_{\mathbf{k},\mathbf{k}'} + \sum_{l,\mathbf{k}}\langle\Psi_{l',\mathbf{k}'}(\mathbf{r})|V_p(\mathrm{r})|\Psi_{l,\mathbf{k}}(\mathbf{r})\rangle A_l(\mathbf{k}) = \sum_{l,\mathbf{k}} E A_l(\mathbf{k})\delta_{l,l'}\delta_{\mathbf{k},\mathbf{k}'} \qquad (72)$$

The delta functions are now evaluated over the sums and the **k** and **k**’ are exchanged to obtain:

$$\sum_{l',\mathbf{k}'}\langle\Psi_{l,\mathbf{k}}(\mathbf{r})|V_p(\mathrm{r})|\Psi_{l',\mathbf{k}'}(\mathbf{r})\rangle A_{l'}(\mathbf{k}') = [E - E_l(\mathbf{k})]\, A_l(\mathbf{k}) \qquad (73)$$

Recalling that the $l = 0$ band is of great importance Eq.(73) is rewritten to highlight this:

$$\sum_{\mathbf{k}'}\langle\Psi_{0,\mathbf{k}}(\mathbf{r})|V_p(\mathrm{r})|\Psi_{0,\mathbf{k}'}(\mathbf{r})\rangle A_0(\mathbf{k}')+\sum_{l'\neq 0,\mathbf{k}'}\langle\Psi_{0,\mathbf{k}}(\mathbf{r})|V_p(\mathrm{r})|\Psi_{l',\mathbf{k}'}(\mathbf{r})\rangle A_{l'}(\mathbf{k}') = [E - E_0(\mathbf{k})]\, A_0(\mathbf{k})$$

$$(l = 0) \qquad (74)$$

$$\sum_{\mathbf{k}'}\langle\Psi_{l,\mathbf{k}}(\mathbf{r})|V_p(\mathrm{r})|\Psi_{0,\mathbf{k}'}(\mathbf{r})\rangle A_0(\mathbf{k}')+\sum_{l'\neq 0,\mathbf{k}}\langle\Psi_{l,\mathbf{k}}(\mathbf{r})|V_p(\mathrm{r})|\Psi_{l',\mathbf{k}'}(\mathbf{r})\rangle A_{l'}(\mathbf{k}') = [E - E_l(\mathbf{k})]\, A_l(\mathbf{k})$$

$$(l \neq 0) \qquad (75)$$

Looking at Eq.(74) more closely we see that the second term can be described in another way such that:

$$\langle\Psi_{l,\mathbf{k}}(\mathbf{r})|V_p(\mathrm{r})|\Psi_{l',\mathbf{k'}}(\mathbf{r})\rangle = \frac{1}{\Omega}\int u^*_{l,\mathbf{k}}u_{l',\mathbf{k'}}\, e^{i(\mathbf{k'}-\mathbf{k})\cdot\mathrm{r}}\, V_p(\mathrm{r})d^3\mathrm{r} \tag{76}$$

The new term Ω is the volume of the crystal. The term $u^*_{l,\mathbf{k}}u_{l',\mathbf{k'}}$ can be written as the following sum since it is a periodic function:

$$u^*_{l,\mathbf{k}}u_{l',\mathbf{k'}} = \sum_{\mathbf{G}} C_{l,\mathbf{k};l',\mathbf{k'}}e^{i\mathbf{G}\cdot\mathrm{r}} \tag{77}$$

With **G** representing the reciprocal lattice vectors. Also it is worth noting, that from orthonormality, with **k’** = **k**:

$$C_{l,\mathbf{k};l',\mathbf{k}} = \delta_{l,l'} \tag{78}$$

Now Eq.(76) becomes:

$$\langle\Psi_{l,\mathbf{k}}(\mathbf{r})|V_p(\mathrm{r})|\Psi_{l',\mathbf{k'}}(\mathbf{r})\rangle = \int\sum_{\mathbf{G}} C^G_{l,\mathbf{k};l',\mathbf{k'}}e^{i(\mathbf{G}+\mathbf{k'}-\mathbf{k})\cdot\mathrm{r}}\, V_p(\mathrm{r})d^3\mathrm{r} \tag{79}$$

The Fourier transform of $V_p(\mathrm{r})$ is defined as:

$$\begin{aligned} V_p(\mathrm{k}) &= \frac{1}{\Omega}\int e^{i\mathbf{k}\cdot\mathrm{r}}\, V_p(\mathrm{r})d^3\mathrm{r} \\ V_p(\mathrm{r}) &= \sum_{\text{all }\mathbf{k}} e^{i\mathbf{k}\cdot\mathrm{r}}\, V_p(\mathrm{k}) \end{aligned} \tag{80}$$

Now:

$$\sum_{\mathbf{k'}}\langle\Psi_{0,\mathbf{k}}(\mathbf{r})|V_p(\mathrm{r})|\Psi_{0,\mathbf{k'}}(\mathbf{r})\rangle A_0(\mathbf{k'}) \approx \sum_{\mathbf{k'}}\sum_{\mathbf{G}} C^G_{l,\mathbf{k};l',\mathbf{k'}}\, V_p(\mathbf{k}-\mathbf{k'}-\mathbf{G})\, A_0(\mathbf{k'}) \tag{81}$$

If we assume that $Vp(\mathbf{r})$ is a slow varying function with respect to the lattice constant a, such that:

$$a|\nabla V_p(\mathrm{r})| \ll V_p(\mathrm{r}) \tag{82}$$

then for **k ~ G,** V_p(k) will be negligible. Now, by assuming **k** is near the center of the Brillouin zone, only the left side terms of Eq.(81) will be negligible, however this will not hold if **G** = 0 since **k**' is confined to the first Brillouin zone. Recall that $A_0(\mathbf{k}')$ around $\mathbf{k}' = \mathbf{k}_0$ is sharply peaked, along with Eqs.(78) and (79), and keeping in mind that the region consider is near $\mathbf{k} = \mathbf{k}_0$, thus:

$$\sum_{\mathbf{k}'} \langle \Psi_{0,\mathbf{k}}(\mathbf{r}) | V_p(\mathrm{r}) | \Psi_{0,\mathbf{k}'}(\mathbf{r}) \rangle \approx \sum_{\mathbf{k}'} V_p(\mathbf{k}\text{-}\mathbf{k}') \tag{83}$$

Using this and according to Eq.(68), letting $A_l(\mathbf{k}) = 0$ for $l \neq 0$, Eq.(70) becomes:

$$\sum_{\mathbf{k}'} V_p(\mathbf{k}\text{-}\mathbf{k}')\, A_0(\mathbf{k}') = [E - E_0(\mathbf{k})]\, A_0(\mathbf{k}) \tag{84}$$

Assuming $\mathbf{k} \approx \mathbf{k}_0$ we have:

$$E_0(\mathbf{k}) \approx E_0(\mathbf{k}_0) + \frac{\hbar^2 (\mathbf{k} - \mathbf{k}_0)^2}{2m^*} \tag{85}$$

To simplify, we let $\mathbf{k}_0 = 0$, now Eq.(64) can be written as:

$$\frac{\hbar^2 (\mathbf{k})^2}{2m^*} A_0(\mathbf{k}) + \sum_{\mathbf{k}'} V_p(\mathbf{k}\text{-}\mathbf{k}')\, A_0(\mathbf{k}') = [E - E_0(\mathbf{k})]\, A_0(\mathbf{k}) \tag{86}$$

With the assumption expressed in Eq.(82) we know that $V_p(\mathbf{k}\text{-}\mathbf{k}')$ is close to zero outside the first Brillion zone, therefore the sum in Eq.(84) can run over all **k'**. Now Eq.(84) becomes the Schrödinger equation in momentum space of an electron of mass m* moving in the potential V_p, with the energy relative to $E_0(0)$.

By utilizing the Fourier transform of $A_l(\mathbf{k})$ Eq.(84) can be transformed to coordinate space:

$$A_l(\mathbf{k}) = \frac{1}{\Omega} \int e^{i\mathbf{k}\cdot\mathrm{r}}\, F_l(\mathbf{r})\, d^3\mathrm{r}$$

$$F_l(\mathbf{r}) = \sum_{\mathbf{k}} e^{i\mathbf{k}\cdot\mathrm{r}}\, A_l(\mathbf{k}) \tag{87}$$

Returning to Eq.(84), multiplying by $e^{i\mathbf{k}\cdot\mathrm{r}}$ and summing over **k,** this is know as the effective mass approximation:

$$\frac{-\hbar^2\nabla^2}{2m^*}F_l(\mathbf{r}) + V_p(\mathbf{r})F_l(\mathbf{r}) = [E - E_0(0)]\,F_l(\mathbf{r}) \qquad (88)$$

Eq.(88) represent the Schrödinger equation for a particle of mass m^* in a potential of $F_l(\mathbf{r})$. The potential is screened by the static dielectric constant ε_0, since, compared to the lattice constant, the wavefunction is spread out. Therefore the Coulomb potential can be described as:

$$V_p(\mathbf{r}) = -\frac{e^2}{\varepsilon_0 r} \qquad (89)$$

The total wavefunction is now:

$$|\Psi_{0,\mathbf{k}'}(\mathbf{r})\rangle = \sum_{\mathbf{k}} A_0(\mathbf{k})|\Psi_{0,\mathbf{k}}(\mathbf{r})\rangle = \sum_{\mathbf{k}} A_0(\mathbf{k})\, e^{i\mathbf{k}\cdot\mathrm{r}} u_{0,\mathbf{k}}(\mathbf{r}) \qquad (90)$$

Again, recalling that $A_0(\mathbf{k})$ is sharply peaked around $\mathbf{k} = \mathbf{k}_0$, we can make a Taylor series expansion:

$$u_{0,\mathbf{k}}(\mathbf{r}) \approx u_{0,\mathbf{k}0}(\mathbf{r}) + (\mathbf{k} - \mathbf{k}_0)\cdot\nabla u_{0,\mathbf{k}}(\mathbf{r}) + \ldots \qquad (91)$$

Using only the first term Eq.(90) now becomes:

$$|\Psi_{0,\mathbf{k}'}(\mathbf{r})\rangle = u_{0,\mathbf{k}0}(\mathbf{r})\sum_{\mathbf{k}} A_0(\mathbf{k})\, e^{i\mathbf{k}\cdot\mathrm{r}} = u_{0,\mathbf{k}0}(\mathbf{r})\, F_l(\mathbf{r}) \qquad (92)$$

For this statement to be true, and therefore the effective mass approximation to be valid, we must verify that the Fourier transform $A_l(\mathbf{k})$ only stretch over a small component of the first Brillouin zone and that the amplitudes $A_{l'}(\mathbf{k})$ ($l' \neq l$) are negligible compared to $A_l(\mathbf{k})$. This is the same as showing that, compared to the size of a unit cell, the wavefunction $F_l(\mathbf{r})$ is expansive in space. Therefore Eq.(92) is only valid if the following is true:

$$A_l(\mathbf{k}) = \frac{1}{E_l - E_l(\mathbf{k})} \sum_{\mathbf{k}'} \langle\Psi_{l,\mathbf{k}}(\mathbf{r})|V_p(\mathbf{r})|\Psi_{0,\mathbf{k}'}(\mathbf{r})\rangle\, A_0(\mathbf{k}') << A_0(\mathbf{k}_0)$$

$$A_0\left(\mathbf{k}_0 + \frac{1}{a}\right) >> A_0(\mathbf{k}_0) \qquad (93)$$

$$V_p(\mathbf{k} = 0) >> V_p\left(\mathbf{k} - \frac{1}{a}\right)$$

The first Brioullin zone on the order of 1/a, with a equal to the lattice constant.

3.1.3 Quantum Transitions

Quantum Transitions such as direct interband transitions, indirect interband transitions, exciton interactions, phonons, and free electron effects are the main processes that give us the dielectric function. For an interband transition, an electron from a valence band is excited into a conduction band, leaving behind a positively charge hole in the valence band. Only a photon and an electron are involved in a direct interband transition, while with a indirect interband transition a scattered phonon is also part of the process. With regards to the direct transitions the electron and hole states have nearly identical **k** values; this is due to the fact that the photon involved carries very little momentum compared to the size of the Brillion zone. However, since an indirect transition involves a phonon, that can carry momentum of the order of the Brillion zone, the electron states can have different **k** values. The indirect transitions have a smaller effect to the optical structure compared with the direct transitions, since they involve three particle interactions. An interband transition has two main effects on the optical function, due to the interaction of the generated electron-hole pair through the Coulomb potential. The first effect is the formation of resonance peaks below the critical points due to discrete bound two-particle states formed by the Coulomb attraction called bound excitons. The other effect is the enhancement of interband transition probability for transition energies at or above the critical points, this is referred to as band to band Coulomb enhancement or also called continuum exciton.

The relation between the imaginary part of the dielectric function and the transitions between band structure states are due to oscillating transverse electric field.

The vector potential, $\mathbf{A}(\mathbf{r},t)$, and a scalar potential, $\Phi(\mathbf{r},t)$, are introduced to describe the electromagnetic fields. By choosing the Coulomb gauge, these potentials take the form:

$$\Phi = 0 \text{ and } \nabla \cdot \mathbf{A} = 0 \tag{94}$$

Therefore:

$$\mathbf{E} = -\frac{1}{c}\frac{\delta \mathbf{A}}{\delta t} \text{ and } \quad \mathbf{B} = \nabla \times \mathbf{A} \tag{95}$$

The motion of a charge $-e$ in an external electromagnetic field is describe by the Hamiltonian, found by making the substitution for the electron momentum operator:

$$-i\hbar\nabla \rightarrow -i\hbar\nabla + \frac{e\mathbf{A}}{c} \tag{96}$$

Now the Hamiltonian becomes:

$$\begin{aligned} H &= \frac{1}{2m_0}\left(-i\hbar\nabla + \frac{e\mathbf{A}}{c}\right)^2 + V(\mathbf{r}) \\ &= \frac{1}{2m_0}\left(-\hbar^2\nabla^2 - \frac{e}{c}\mathbf{A}\cdot i\hbar\nabla - \frac{e}{c} i\hbar\nabla\cdot\mathbf{A} + \frac{e^2\mathbf{A}^2}{2c^2} + V(\mathbf{r})\right) \\ &= \frac{1}{2m_0}\left(-\hbar^2\nabla^2 - \frac{2e}{c}\mathbf{A}\cdot i\hbar\nabla + \frac{e^2\mathbf{A}^2}{2c^2} + V(\mathbf{r})\right) \\ &\approx \frac{1}{2m_0}\left(-\hbar^2\nabla^2 - \frac{2e}{c}\mathbf{A}\cdot i\hbar\nabla + V(\mathbf{r})\right) \end{aligned} \tag{97}$$

The approximation in the fourth line comes from neglecting the quadratic term $e^2\mathbf{A}^2/(2m_0c^2)$ since we are looking only at the linear or low field optical properties. The term $e/m_0c\ \mathbf{A}\cdot i\hbar\nabla$ will be treated as a perturbation. The vector potential $\mathbf{A}(\mathbf{r},t)$ for an electric field of magnitude E, wavevector $\mathbf{k}^{\mathbf{L}}$, frequency ω, and polarization vector $\check{\mathbf{e}}$ is written in the form:

$$\mathbf{A}(\mathbf{r},t) = -\frac{Ec}{2\omega}\hat{e}\left(e^{i(\mathbf{k}_{\mathbf{L}}\cdot\mathbf{r}-\omega t)} + e^{-i(\mathbf{k}_{\mathbf{L}}\cdot\mathbf{r}-\omega t)}\right) \tag{98}$$

The absorption process is described by the term containing $e^{i(\mathbf{k}_{\mathbf{L}}\cdot\mathbf{r}-\omega t)}$, and the term containing $e^{-i(\mathbf{k}_{\mathbf{L}}\cdot\mathbf{r}-\omega t)}$ represents the stimulated emission in the presence of an electric field. For this heavily time dependent perturbation, the probability of transition per unit time is:

$$P_{v,c} = \left|\int_{-\infty}^{\infty} \langle \Psi_{c,\mathbf{k}_c}(\mathbf{r})|\mathbf{A}(\mathbf{r},t)\cdot i\hbar\nabla|\Psi_{v,\mathbf{k}_v}\rangle e^{i\omega_{cv}t}\,dt\right|^2 \tag{99}$$

The conduction and valence bands correspond to the subscripts c and v with:

$$\omega_{cv} = \frac{E_c - E_v}{\hbar} \tag{100}$$

and the time independent Bloch functions:

$$|\Psi_{v,\mathbf{k}_v}\rangle = e^{i\mathbf{k}_v\cdot\mathbf{r}}\,u_{v,\mathbf{k}_v} \tag{101}$$

$$|\Psi_{c,\mathbf{k}_c}\rangle = e^{i\mathbf{k}_c\cdot\mathbf{r}}\,u_{c,\mathbf{k}_c}$$

Eq.(99) is only valid in the normal linear optic regime, that is when $P_{v,c} << 1$. This is when most of the electrons are in their ground state. For the term corresponding to absorption in Eq.(99), the integration over time becomes:

$$\int e^{i\omega_{cv}t}e^{-i\omega t}\,dt = \frac{2\pi}{\hbar}\delta[E_c(\mathbf{k}_c) - E_v(\mathbf{k}_v) - \hbar\omega] \tag{102}$$

As expected from the conservation of energy, the photon energy must be exactly the energy difference between the conduction and valence bands. Examining the time independent part of Eq.(99) we get:

$$\langle \Psi_{c,\mathbf{k}_c}(\mathbf{r})|\mathbf{A}(\mathbf{r},t)\cdot i\hbar\nabla|\Psi_{v,\mathbf{k}_v}\rangle = -\frac{Ei\hbar}{2k_R}\int u^*_{c,\mathbf{k}_c}e^{i(\mathbf{k}_{\mathbf{L}}-\mathbf{k}_c)\cdot\mathbf{r}}(\hat{e}\cdot\nabla)\,e^{i\mathbf{k}\cdot\mathbf{r}}u_{v,\mathbf{k}_v}d\mathbf{r}$$

$$= -\frac{Ei\hbar}{2k_R}\ \check{e}\cdot\int u^*_{c,\mathbf{k}}\, e^{i(\mathbf{k}\,-\,\mathbf{k})\cdot\mathbf{r}}(e^{i\mathbf{k}\cdot\mathbf{r}}\nabla\ u_{v,\mathbf{k}_v} + \hbar\mathbf{k}_v\, u_{v,\mathbf{k}}\, e^{i\mathbf{k}\cdot\mathbf{r}})d\mathbf{r} \qquad (103)$$

Since both $u_{v,\mathbf{k}_v}$ and $u_{c,\mathbf{k}_c}$ are orthogonal the second term in the last line of Eq.(103) will vanish. Also, because of their periodicity, the integral of the first term in the last line can be rewritten using $\mathbf{r} = \mathbf{R}_j + \mathbf{r}'$, with $\mathbf{r}'$ lying in one unit cell and $\mathbf{R}_j$ as a reciprocal lattice vector:

$$\int u^*_{c,\mathbf{k}_c} e^{i(\mathbf{k}_v-\mathbf{k}_c-\mathbf{k})\cdot\mathbf{r}}\ \nabla u_{v,\mathbf{k}_v}\, d\mathbf{r} = \int_{\substack{\text{unit}\\\text{cell}}} u^*_{c,\mathbf{k}+\mathbf{k}}\nabla\ u_{v,\mathbf{k}_v}\, d\mathbf{r}' \qquad (104)$$

This expression can be simplified even further since $\mathbf{k}^{\mathrm{L}}$ is three to four orders of magnitude smaller than the size of the Brillouin zone for visible light, therefore:

$$u_{\mathbf{k}_v+\mathbf{k}^{\mathbf{L}}} = u_{\mathbf{k}_v} + \mathbf{k}^{\mathrm{L}}\cdot\nabla_{\mathbf{k}} u_{\mathbf{k}_v} + \ldots \approx u_{\mathbf{k}_v} \qquad (105)$$

Now Eq.(104) can be written as:

$$\int u^*_{c,\mathbf{k}} e^{i(\mathbf{k}_{\mathbf{R}}-\mathbf{k}_v-\mathbf{k}_c)\cdot\mathbf{r}}\ \nabla u_{v,\mathbf{k}_v} d\mathbf{r} = \int u^*_{c,\mathbf{k}}\nabla u_{v,\mathbf{k}}\, d\mathbf{r}' \qquad (106)$$

Now combining Eqs.(98), (99), (102), (103), and (106), we can determine the final expression for the transition probability per unit time:

$$P_{v,c} = \frac{2\pi}{\hbar}\left(\frac{e\,.}{m_0\omega}\right)^2 \left|\frac{E(\omega)}{2}\right|^2 \sum_{\mathbf{k}}\|\mathbf{M}_{cv}(\mathbf{k})\|^2\delta[E_c(\mathbf{k}_c) - E_v(\mathbf{k}_v) - \hbar\omega] \qquad (107)$$

with

$$\|\mathbf{M}_{cv}(\mathbf{k})\|^2 = \hbar^2\|\langle\Psi_{c,\mathbf{k}}|\check{\mathbf{e}}\cdot\nabla\|\Psi_{v,\mathbf{k}}\rangle\|^2 = \left(\hbar\int_{\substack{\text{unit}\\\text{cell}}} u^*_{\mathbf{k}}\,\check{\mathbf{e}}\cdot\nabla u_{\mathbf{k}}\, d\mathbf{r}'\right)^2 \qquad (108)$$

The absorption transition rate per unit volume of the crystal is given by Eq.(107), by restricting the summation over $\mathbf{k}$ to only those $\mathbf{k}$'s allowed per unit volume of the crystal. The Probability times the energy for each photon will give the power loss per unit volume, which can also be in terms of the imaginary dielectric function:

$$\text{Power loss} = P_{v,c}\,\hbar\omega = -\frac{dI}{dt} = -\left(\frac{dI}{dx}\right)\left(\frac{dx}{dt}\right) = (I\alpha)\frac{c}{n} = \frac{\alpha c I}{n} = \frac{\varepsilon_i c I}{n^2} \tag{109}$$

where the intensity of the incident beam is represented by I :

$$I = \frac{n^2}{8\pi}\,\|E(\omega)\|^2 \tag{110}$$

Now we find:

$$\varepsilon_2(\mathrm{E}) = \left(\frac{2\pi e\hbar}{m_0 E}\right)^2 \sum_{c,v}\sum_{\mathbf{k}} \|\mathbf{M}_{cv}(\mathbf{k})\|^2\,\delta[E_c(\mathbf{k}) - E_v(\mathbf{k}) - E] \tag{111}$$

With the photon energy $\hbar\omega = E$. For allowed transitions $\mathbf{M}_{cv}$ is typically constant near a critical point $\mathbf{k} \approx \mathbf{k}_0$, since our interest is in the contribution to the dielectric function near a critical point, we will let $\mathbf{M}_{cv}(\mathbf{k}) \approx \mathbf{M}_{cv}(\mathbf{k}_0)$. With this simplification we can see that the dielectric function merely comes from the sum over the allowed transition energies, this is also known as the interband or joint density of states (JDOS). The JDOS will vary depending on the nature of the critical point.

$$\varepsilon_2(\mathrm{E}) = \left(\frac{2\pi e\hbar}{m_0 E}\right)^2 \|\mathbf{M}_{cv}(\mathbf{k}_0)\|^2 \sum_{c,v}\sum_{\mathbf{k}} \delta[E_c(\mathbf{k}) - E_v(\mathbf{k}) - E] \tag{112}$$

To find the real part of the dielectric function, the Kramers-Kronig relation for ε_1 must be used:

$$\varepsilon_1(\mathrm{E}) - 1 = \frac{1}{\pi} P\int_{-\infty}^{\infty} \frac{\varepsilon_2(E')}{E' - E}\,dE' \tag{113}$$

Implementing this relation we find the form of the real dielectric function:

$$\varepsilon_1(\mathrm{E}) = 1 + \frac{8\pi e\hbar^2}{m_0^2} \sum_{\mathbf{k}} \frac{\|\mathbf{M}_{cv}\|^2}{[E_c(\mathbf{k}) - E_v(\mathbf{k})]\{[E_c(\mathbf{k}) - E_v(\mathbf{k})]^2 - E^2\}} \tag{114}$$

Expressing the JDOS term from Eq.(112) using the quasi-continuous approximation we obtain:

$$\sum\delta[E_c(\mathbf{k}) - E_v(\mathbf{k}) - E] \rightarrow D(E)dE \tag{115}$$

With the integral becoming:

$$\int D(E)dE = 2\int \frac{d^3k}{(2\pi)^3} = \frac{2}{(2\pi)^3}\int \frac{dS_{\mathbf{k}}}{\|\nabla_{\mathbf{k}}E\|}\, dE \tag{116}$$

The JDOS is represented as a function of energy in *D(E)dE*, and $S_{\mathbf{k}}$ is the constant energy surface defined with $E(\mathbf{k})$ = constant. Since this can be evaluated for a variety of critical points, to continue, we will assume we are dealing with a 3D M_0 type critical point, this is described as a parabolic E vs. **k** bands in 3 dimensions. Now the energy as a function of **k** is described by:

$$E(\mathbf{k}) = \frac{\hbar^2\mathbf{k}^2}{2\mu^*} + E_g \tag{117}$$

With μ* representing the reduced interband effective mass, and the bandgap of interest is E_g. Now the JDOS becomes:

$$D_{3D}(E) = \begin{cases} \dfrac{\mu^{*3/2}\,[2(E - E_g)]^{1/2}}{\pi^2\hbar^3} & E > E_g \\ 0 & E < E_g \end{cases} \tag{118}$$

With a 2D M_0 critical point, that is a parabolic E vs. **k** bands in two dimensions with no dispersion in the third, the energy as a function of **k** is then described by:

$$E(\mathbf{k}) = E_g + \frac{\hbar^2\mathbf{k}^2}{2\mu_p^*} \tag{119}$$

With μ_p* as the reduced effective mass in the direction perpendicular to the direction that has no dispersion. With the 2D M_0 critical point the JDOS new becomes:

$$D_{2D}(E) = \begin{cases} \dfrac{\mu_p^*}{\pi^2\hbar^3} & E > E_g \\ 0 & E < E_g \end{cases} \tag{120}$$

3.1.4 Quantum Transitions Considering Excitonic Effects

If we want to examine the excitonic effects on the absorption coefficient, the formalism described in the previous section must be altered. In the previous section we considered a transition of an electron from a valence state to a conduction state, in this section we instead consider that a photon excites the crystal from its ground state to a state with one hole in the valence band and one electron in the conduction band. Therefore with no electron-hole interaction, the process is written as:

$$|0\rangle \xrightarrow[photon]{} |\mathbf{k}_e, \mathbf{k}_h, \mathbf{r}\rangle = |\Psi^e{}_{c,\mathbf{k}_e}(\mathbf{r})\rangle|\Psi^h{}_{v,\mathbf{k}_h}(\mathbf{r})\rangle \tag{121}$$

With the electron in the conduction band represented by $|\Psi^e{}_{c,\mathbf{k}}(\mathbf{r})\rangle$ with a Bloch function of wavevector $\mathbf{k}_e$, and the hole in the valence band represented by $|\Psi^h{}_{v,\mathbf{k}}(\mathbf{r})\rangle$ with a Bloch function of wavevector $\mathbf{k}_h$. For now Eq.(121) is constructed from Bloch function, however, once the Coulomb attraction is added, following the envelope function formalism, the excited state will be given as an expansion of the state as a superposition of the states given in Eq.(121). If the total wavevector of the electron-hole pair is $\mathbf{k}_{ex} = \mathbf{k}_e + \mathbf{k}_h$ then the expansion of the exciton state is:

$$|\Psi_{ex}(\mathbf{r})\rangle = \sum_{\mathbf{k}} A(\mathbf{k})\, |\Psi^e{}_{c,\mathbf{k}+\mathbf{k}_e}(\mathbf{r}_e)\rangle|\Psi^h{}_{v,\mathbf{k}-\mathbf{k}_h}(\mathbf{r}_h)\rangle \tag{122}$$

Since, as stated previously, the momentum of the photon is negligible with comparison to the size of the first Brillouin zone, we can assume $\mathbf{k}_{ex} \approx 0$. With a two particle state, we therefore consider the two particle Hamiltonian:

$$H = -\frac{i\hbar^2\nabla_e^2}{2m} + \frac{i\hbar^2\ \nabla_h^2}{2m} + V_c(\mathbf{r}_e) - V_c(\mathbf{r}_h) - \frac{e^2}{\varepsilon_0|\mathbf{r}_e - \mathbf{r}_h|}.$$

$$= H^e{}_0(\mathbf{r}_e) - H^h{}_0(\mathbf{r}_h) + V_p(r) \tag{123}$$

Where $r = |\mathbf{r}_e - \mathbf{r}_h|$, and the free electron Hamiltonian, free hole Hamiltonian and the Coulomb potential are defined as:

$$H^e{}_0(\mathbf{r}_e) = -\frac{i\hbar^2\nabla_e^2}{2m} + V_c(\mathbf{r}_e)$$

$$H^h{}_0(\mathbf{r}_h) = -\frac{i\hbar^2\nabla_h^2}{2m} + V_c(\mathbf{r}_h) \tag{124}$$

$$V_p(r) = -\frac{e^2}{\varepsilon_0|\mathbf{r}_e - \mathbf{r}_h|}.$$

Notice that the hole's energy is negative, which is expected since it represents the absence of the electron's energy for that state. The energy is lowered since the perturbative Coulomb potential is attractive. Following this notation the Schrödinger equation for the exciton becomes:

$$H^e{}_0(\mathbf{r}_e) - H^h{}_0(\mathbf{r}_h) + V_p(r)|\Psi_{ex}(\mathbf{r})\rangle = E|\Psi_{ex}(\mathbf{r})\rangle \tag{125}$$

By multiplying the right hand side by $\langle\Psi^h{}_{c,\mathbf{k+k}}(\mathbf{r}_h)|\langle\Psi^e{}_{c,\mathbf{k\text{-}k}}(\mathbf{r}_e)|$ and summing over $\mathbf{k}$ we obtain:

$$\sum\langle\Psi_{0,\mathbf{k}}(\mathbf{r})|V_p(r)|\Psi_{0,\mathbf{k}'}(\mathbf{r})\rangle\, A(\mathbf{k'}) = \{E - [E_c(0) - E_v(0)]\}\, A(\mathbf{k}) \tag{126}$$

This, as seen in the previous section, leads to the effective mass approximation which takes the form:

$$-\left(\frac{i\hbar^2\nabla^2}{2\mu^*} \quad \frac{e^2}{\varepsilon_0 r}. \right) F(\mathbf{r}) = \{E - [E_c(0) - E_v(0)]\}\ F(\mathbf{r}) = E_{ex}\, F(\mathbf{r}) \tag{127}$$

With μ^* as the effective mass tensor and the critical point is at $\mathbf{k} = \mathbf{k}_0$, and the defined exciton energy E_{ex} is compared to the bandgap energy by, $E_{ex} = E - [E_c(0) - E_v(0)] = E - E_g$.

To account for the modified wavefunction we must reconsider the dipole transition matrix in the area of the critical point:

$$\|\mathbf{M}_{cv}(\mathbf{k})\|^2 \rightarrow \|\sum_{\mathbf{k}} A(\mathbf{k})\mathbf{M}_{cv}(\mathbf{k})\|^2 \tag{128}$$

If we again assume in the area of the critical point at $\mathbf{k} = \mathbf{k}_0$ that $\mathbf{M}_{cv}(\mathbf{k}) \approx \mathbf{M}_{cv}(\mathbf{k}_0)$ then Eq.(128) will now become:

$$\|\sum_{\mathbf{k}} A(\mathbf{k})\mathbf{M}_{cv}(\mathbf{k})\|^2 \approx \|\mathbf{M}_{cv}(\mathbf{k}_0)\sum_{\mathbf{k}} A(\mathbf{k})\|^2 = \|\mathbf{M}_{cv}(\mathbf{k_0})\|^2\|F(0)\|^2 \tag{129}$$

To determine the imaginary part of the dielectric function we multiply the square of the magnitude of the envelope function at $\mathbf{r} = 0$ by Eq.(112) to get:

$$\varepsilon_2^{exciton}(E) = \|F(0)\|^2\, \varepsilon_2^{SP}(E) \tag{130}$$

From Eq.(112) we get the single particle function $\varepsilon_2^{SP}(E)$, with $\varepsilon_2^{exciton}(E)$ as the imaginary dielectric function including the exciton interaction. Using the expression for the single particle function with obtain:

$$\varepsilon_2^{exciton}(E) = \|F(0)\|^2 \left(\frac{2\pi e\hbar}{m_0 E}\right)^2 \|\mathbf{M}_{cv}(\mathbf{k}_0)\|^2 \sum_{all\ states} \delta[E_{ex} + E_g - E] \tag{131}$$

Notice that the sum now runs over all allowed energies, for photon energies above the bandgap the results will agree with the interband density of states given is Eq.(117), for photon energies below the bandgap the results will give the discrete bound states.

3.1.5 Indirect Transitions

When considering interactions between electrons with phonons (vibrations of the lattice) the assumption taken in the previous section that transitions between valence and conduction states are nearly vertical ($\mathbf{k}_v \approx \mathbf{k}_c$) is no longer valid. Now we are dealing with a photon exciting an electron from the valence band to the conduction band with the help of a phonon, therefore the transformation in the electron's wavevector is done by the phonon.

Since the indirect transitions involve a three particle interaction, they are less likely than a direct transition. However one of the most likely indirect gap absorptions processes can be seen in Fig. 6. The electron is excited by a non-energy conserving (virtual) transition by the absorption of a photon, path (1). Although the transition is non-energy conserving, it still conserves momentum through the translation symmetry of the crystal. The path (1') illustrates the second virtual transition which takes the electron to the final state with a different **k** vector, $\mathbf{q} = \mathbf{k}_c = \mathbf{k}_v$ through the emission or absorption of a phonon.

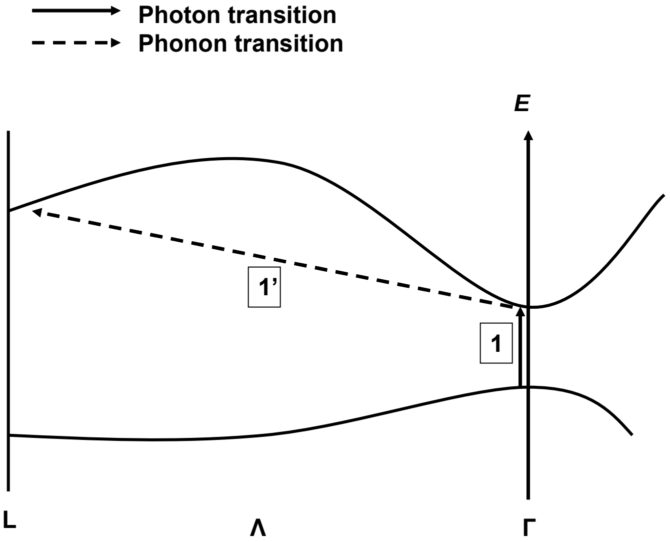

Figure 6: indirect gap absorptions processes

Starting with the Hamiltonian we can investigate this transition analytically. The Hamiltonian is perturbed by both an electric field and a phonon interation such that:

$$H = H_0 + H_{eR} + H_{ep} \tag{132}$$

The unperturbed Hamiltonian H_0 has eigenfunctions which are Bloch states, H_{ep} represents the electron-phonon interaction, and the perturbation due to the electromagnetic radiation field is given by H_{eR} which is written as:

$$H_{eR} = -\frac{e}{mc}\mathbf{A}\cdot i\hbar\nabla \qquad (133)$$

Beginning with the perturbation of the electron-phonon interaction H_{ep}, which will mix Bloch states at **k** and **k**’, the states now are given by second order perturbation theory:

$$|l,\mathbf{k}\rangle = |l^0,\mathbf{k}\rangle + \sum_{m\neq l}\frac{|m^0,\mathbf{k}\rangle\langle m^0,\mathbf{k}'|H_{ep}|\,l^0,\mathbf{k}\rangle}{E_0(l^0,\mathbf{k}) - E_0(m^0,\mathbf{k}')\pm\hbar\omega_p} \qquad (134)$$

The new perturbed wavefuction is represented by $|l,\mathbf{k}\rangle$, and $|l^0,\mathbf{k}\rangle$is the unperturbed Bloch function of wavevector **k** and band index *l*. The energy of the unperturbed state is shown as $E_0(l^0,\mathbf{k})$, and $E_0(m^0,\mathbf{k}')$ is the energy of the unperturbed intermediate state $|m^0,\mathbf{k}\rangle$. This expression is valid when:

$$\frac{\langle m^0,\mathbf{k}'|H_{ep}|\,l^0,\mathbf{k}\rangle}{E_0(l^0,\mathbf{k}) - E_0(m^0,\mathbf{k}')\pm\hbar\omega_p} << 1 \qquad (135)$$

Therefore

$$\langle c,\mathbf{k}'|e\cdot\mathbf{p}|\,v,\mathbf{k}\rangle = \sum_{m\neq v}\sum_{\mathbf{k}m}\frac{\langle c^0,\mathbf{k}'|e\cdot\mathbf{p}|\,m^0,\mathbf{k}_m\rangle\langle m^0,\mathbf{k}_m|H_{ep}|\,v^0,\mathbf{k}\rangle}{E_0(v^0,\mathbf{k}) - E_0(m^0,\mathbf{k}_m)\pm\hbar\omega_p}$$

$$+\sum_{l\neq v}\sum_{\mathbf{k}l}\frac{\langle c^0,\mathbf{k}'|H_{ep}|\,l^0,\mathbf{k}_l\rangle\langle l^0,\mathbf{k}_l|e\cdot\mathbf{p}|\,v^0,\mathbf{k}\rangle}{E_0(v^0,\mathbf{k}) - E_0(l^0,\mathbf{k}_l)\pm\hbar\omega_p} \qquad (136)$$

The perturbation $e\cdot\mathbf{p}$ preserves **k**, so that $\mathbf{k}_m = \mathbf{k}'$ and $\mathbf{k}_l = \mathbf{k}$ which was seen in Eq.(106), and by using the definition from Eq.(108) the following can be determined:

$$\mathbf{M}_{eR,ep}(\mathbf{k},\mathbf{k}') \equiv \langle c,\mathbf{k}'|e\cdot\mathbf{p}|\, v,\mathbf{k}\rangle = \sum_{m\neq v} \frac{e\cdot \mathbf{M}_{cm}(\mathbf{k}')\langle m^0,\mathbf{k}_m|H_{ep}|\, v^0,\mathbf{k}\rangle}{E_0(v^0,\mathbf{k}) - E_0(m^0,\mathbf{k}_m)\pm\hbar\omega_p} + \sum_{l\neq v} \frac{\langle c^0,\mathbf{k}'|H_{ep}|\, l^0,\mathbf{k}_l\rangle e\cdot \mathbf{M}_{lv}(\mathbf{k})}{E_0(v^0,\mathbf{k}) - E_0(l^0,\mathbf{k}_l)\pm\hbar\omega_p} \tag{137}$$

By summing the contributions from all possible transitions within the first Brillioun zone, and by following the step leading up to Eq.(111), the imaginary part of the dielectric function due to an indirect transitions becomes:

$$\varepsilon_2(E) = \left(\frac{2\pi e\hbar}{m_0 E}\right)^2 \sum_{\mathbf{k}}\sum_{\mathbf{k}'} \|\mathbf{M}_{eR,ep}(\mathbf{k},\mathbf{k}')\|^2 \sum \delta[E_c(\mathbf{k}') - E_v(\mathbf{k}) - E + \hbar\omega_p] \tag{138}$$

If we assume that the matrix elements $\mathbf{M}_{eR,ep}(\mathbf{k},\mathbf{k}')$ is constant in the region of the indirect bandgap, which is the case for many semiconductors, we can convert the sums in Eq.(138) to integrals over the density of states. Now the structure of the indirect gap becomes:

$$\sum_{\mathbf{k}}\sum_{\mathbf{k}'} \delta[E_c(\mathbf{k}') - E_v(\mathbf{k}) - E + \hbar\omega_p] = \iint D_v(E_v)D_c(E_c)\, \delta[E_c(\mathbf{k}') - E_v(\mathbf{k}) - E + \hbar\omega_p]\,dE_c dE_v \tag{139}$$

If the bands are parabolic:

$$E_c(\mathbf{k}') = E_{ind} + \frac{\hbar^2\mathbf{k}'^2}{2m_c^*}$$
$$E_v(\mathbf{k}) = \frac{\hbar^2\mathbf{k}^2}{2m_v^*} \tag{140}$$

Both **k** , **k**’, and the effective masses are referenced to their own extrema, with the zero energy at the top of the valence band. With the use of Eq.(117), the densities of states are:

$$D_v(E_v) = \begin{cases} \dfrac{m_v^{*3/2}\,[-2E_v]^{1/2}}{\pi^2\hbar^3} & E_v < 0 \\ 0 & E_v > 0 \end{cases} \qquad (141)$$

$$D_c(E_c) = \begin{cases} \dfrac{m_c^{*3/2}\,[-2(E_c - E_{ind}]^{1/2}}{\pi^2\hbar^3} & E_c < E_{ind} \\ 0 & E_c > E_{ind} \end{cases}$$

Working through the integral we obtain:

$$\iint D_v(E_v)D_c(E_c)\delta[E_c(\mathbf{k}') - E_v(\mathbf{k}) - E \pm \hbar\omega_p]dE_c dE_v$$

$$= \frac{2(m_c^* m_v^*)^{3/2}}{\pi^4\hbar^6} \int_{Eg}^{\hbar\omega\pm\hbar\omega p} [E \pm \hbar\omega_p \quad E_c]^{1/2}[E_c - E_{ind}]^{1/2}\, dE_c \qquad (142)$$

If we change the integration variable to x = $E_c - E_{ind}/E\pm\hbar\omega_p - E_c$ then the integral becomes:

$$\int [E \pm \hbar\omega_p - E_c]^{1/2}[E_c - E_{ind}]^{1/2}\, dE_c = (E_c - E_{ind} \pm\hbar\omega_p)^2 \qquad (143)$$

Now the expression for the imaginary part of the dielectric function becomes:

$$\varepsilon_2(E) = \left(\frac{2\pi e\hbar}{m^0 E}\right)^2 \frac{(m_c^* m_v^*)^{3/2}}{4\pi^3\hbar^6} \times \|M_{eR,ep}(\mathbf{k}_{0,v}, \mathbf{k}_{0,c})\|^2 [E - E_{ind} \pm \hbar\omega_p]^2 \theta\left(1 - \frac{E_{ind} \pm \hbar\omega_p}{E}\right) \qquad (144)$$

With θ as the unit step function, and the **k** vectors at the critical point extrema of the conduction and valence band are $\mathbf{k}_{0,v}$, $\mathbf{k}_{0,c}$.

3.1.6 Dielectric Function Symmetries and the Kramers-Kronig Relation

We again return to Jackson[29], for the description of the dielectric function:

$$\mathbf{D}(\mathbf{r},\omega) = \varepsilon^*(\omega)\mathbf{E}(\mathbf{r},\omega) = \mathbf{E}(\mathbf{r},\omega) + 4\pi\chi^*(\omega)\mathbf{E}(\mathbf{r},\omega) \tag{145}$$

With the complex frequency dependent dielectric function and polarizability represented by $\varepsilon^*(\omega)$ and $\chi^*(\omega)$. Using Fourier transformations we can relate $\mathbf{D}(\mathbf{r},\omega)$ and $\mathbf{E}(\mathbf{r},\omega)$ to the time dependent expressions:

$$\begin{aligned}
\mathbf{D}(\mathbf{r},t) &= \frac{1}{\sqrt{2\pi}} \int_{-\infty}^{\infty} \mathbf{D}(\mathbf{r},\omega)e^{-i\omega t}d\omega \\
\mathbf{D}(\mathbf{r},\omega) &= \frac{1}{\sqrt{2\pi}} \int_{-\infty}^{\infty} \mathbf{D}(\mathbf{r},t)e^{-i\omega t}dt \\
\mathbf{E}(\mathbf{r},t) &= \frac{1}{\sqrt{2\pi}} \int_{-\infty}^{\infty} \mathbf{E}(\mathbf{r},\omega)e^{-i\omega t}d\omega \\
\mathbf{E}(\mathbf{r},\omega) &= \frac{1}{\sqrt{2\pi}} \int_{-\infty}^{\infty} \mathbf{E}(\mathbf{r},t)e^{-i\omega t}dt
\end{aligned} \tag{146}$$

With these expressions we can write

$$\begin{aligned}
\mathbf{D}(\mathbf{r},t) &= \mathbf{E}(\mathbf{r},t) + \frac{1}{\sqrt{2\pi}} \int_{-\infty}^{\infty} 4\pi\chi^*(\omega)\mathbf{E}(\mathbf{r},\omega)e^{-i\omega t}d\omega \\
&= \mathbf{E}(\mathbf{r},t) + 2\int_{-\infty}^{\infty}\chi^*(\omega)\, e^{-i\omega t} \int_{-\infty}^{\infty}\mathbf{E}(\mathbf{r},t')e^{-i\omega t'}dt'd\omega
\end{aligned} \tag{147}$$

By making the substitution $\tau = t - t'$ and integration over ω we find:

$$\mathbf{D}(\mathbf{r},t) = \mathbf{E}(\mathbf{r},t) + \frac{1}{\sqrt{2\pi}} \int_{-\infty}^{\infty} G(\tau)\, \mathbf{E}(\mathbf{r},t - \tau)d\tau \tag{148}$$

With the Fourier transform of $4\pi\chi^*(\omega) = \varepsilon^*(\omega) - 1$ as:

$$\begin{aligned}
G(\tau) &= \frac{1}{\sqrt{2\pi}} \int_{-\infty}^{\infty} [\varepsilon^*(\omega) - 1]e^{-i\omega\tau}d\omega \\
\varepsilon^*(\omega) &= 1 + \int_{-\infty}^{\infty} G(\tau)e^{-i\omega\tau}d\tau
\end{aligned} \tag{149}$$

The argument of causality is that the electric displacement **D** at a time *t* is only determined by the electric fields that have occurred up to that time, therefore $G(\tau) = 0$ for $\tau < 0$. If we apply this argument to Eq. (148) we find:

$$\mathbf{D}(\mathbf{r},t) = \mathbf{E}(\mathbf{r},t) + \frac{1}{\sqrt{2\pi}} \int_0^{\infty} G(\tau)\, \mathbf{E}(\mathbf{r},t - \tau)\, d\tau \qquad (150)$$

Also the second part of Eq.(149) can be written as:

$$\varepsilon^*(\omega) = 1 + \int_0^{\infty} G(\tau) e^{-i\omega\tau} d\tau \qquad (151)$$

From Eq.(150) and from the nature of $\mathbf{D}(\mathbf{r},t)$ and $\mathbf{E}(\mathbf{r},t)$ we can deduce that $G(\tau)$ must be real. With Eqs.(146) and (151) we find that:

$$\begin{aligned} \mathbf{D}(-\omega) &= \mathbf{D}'(\omega') \\ \mathbf{E}(-\omega) &= \mathbf{E}'(\omega') \\ \varepsilon^*(-\omega) &= \varepsilon^{*\prime}(\omega') \end{aligned} \qquad (152)$$

These equations demonstrate that for real ω, the real and imaginary parts of the dielectric function are even and odd. Also, we see that with a finite $G(\tau)$, $\varepsilon^*(\omega)$ is an analytic function in the complex upper half plane, Im $\omega>0$. Along the real axis $\varepsilon^*(\omega)$ is analytic, if $G(\tau)\to 0$ as $\tau\to\infty$. An important Kramers-Kronig relation comes out of the analyticity of $\varepsilon^*(\omega)$. This relation relates the real and imaginary parts of $\varepsilon^*(\omega)$. We'll start with Cauchy's theorem states for any point ω in the upper half plane:

$$\varepsilon^*(\omega) - 1 = \frac{1}{2\pi i} \int_C \frac{\varepsilon^*(\omega') - 1}{\omega' - \omega}\, d\omega' \qquad (153)$$

By taking the contour to consist of the real ω axis and a semicircle at infinity in the upper half plane, then $\varepsilon^*(\omega) \to 0$ as $||\omega|| \to \infty$. Therefore there will be no contribution to the integral from the semicircle. Now Eq.(153) becomes:

$$\varepsilon^*(\omega) - 1 = \frac{1}{2\pi i} \int_{-\infty}^{\infty} \frac{\varepsilon^*(\omega') - 1}{\omega' - \omega}\, d\omega' \qquad (154)$$

Eq.(150) has only a single pole at ω = ω', therefore it now becomes:

$$\varepsilon^*(\omega) - 1 = \frac{1}{\pi i} P\int_{-\infty}^{\infty} \frac{\varepsilon^*(\omega') - 1}{\omega' - \omega} d\omega' \tag{155}$$

With *P* as the Cauchy principal part of the integral. Now the real and imaginary parts of Eq.(155) become:

$$\begin{aligned} \varepsilon_1(E) - 1 &= \frac{1}{\pi} P\int_{-\infty}^{\infty} \frac{\varepsilon_2(E')}{E' - E} dE' \\ \varepsilon_2(E) - 1 &= \frac{1}{\pi} P\int_{-\infty}^{\infty} \frac{\varepsilon_1(E') - 1}{E' - E} dE' \end{aligned} \tag{156}$$

By using the symmetry property of the dielectric function Eq.(156) becomes:

$$\begin{aligned} \varepsilon_1(E) - 1 &= \frac{2}{\pi} P\int_{0}^{\infty} \frac{E'\varepsilon_2(E')}{\omega'^2 - \omega^2} dE' \\ \varepsilon_2(E) - 1 &= \frac{2E}{\pi} P\int_{0}^{\infty} \frac{\varepsilon_1(E')-1}{E'^2 - E^2} dE' \end{aligned} \tag{157}$$

These equations are known as the Kramers-Kronig relations.

3.2 Dielectric Function Theory: Amorphous Materials

As mentioned in section 3.1, the absence of long-range order in amorphous materials renders the Bloch theorem inapplicable. In this section we will discuss the optical band gap and model dielectric function of amorphous materials.

3.2.1 Optical Band Gap

To describe the optical transitions in amorphous semiconductors Pierce and Spicer[37] suggested that to a first approximation the transitions could be described by the non-direct transition model in which conservation of energy but not wave vector is significant. With the absence of ***k*** space in amorphous semiconductors it would seem that the density of electronic state is not a meaningful concept, however this is not the case. The density of states $N(E)$ for an amorphous semiconductor compared to that for a crystal is shown in Fig.(7). Note, the lack of sharp band edges and tailing of $N(E)$ into the gap, and the localization of states in energy regions where $N(E)$ is low, also the existence of

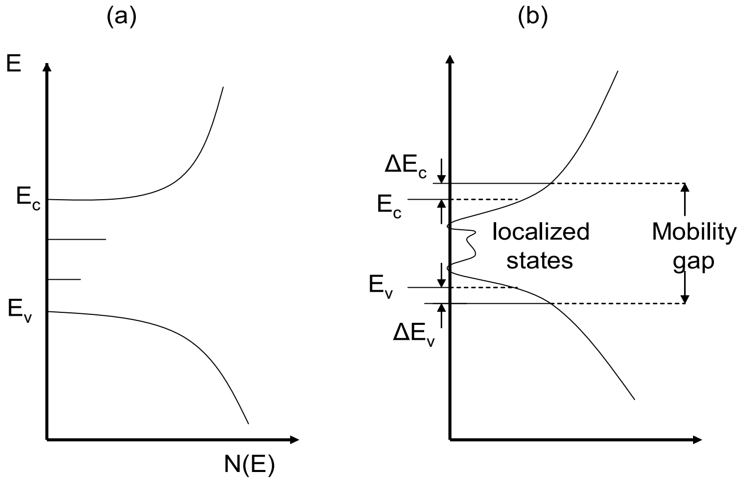

Figure 7: Density of states for (a) crystalline and (b) amorphous semiconduct ΔE_c and ΔE_v are band tails due to disorder.

broad bands of defect levels in the gap compared to the sharp discrete levels in the crystal. The absorption coefficient α can be described by the relation

$$E\alpha \sim (E - E_o)^n \qquad (158)$$

with the constant n usually equal to 2 or 3, and E_o as the optical band-gap energy. This relation is not based on a rigid theoretical model therefore it is somewhat semiempirical. Consequently E_o is deduced from experimental data.

In Chapter 5 High-k Dielectric Film results, we will discuss further how indirect bandgap information from the absorption coefficient is obtained. In Section 5.2.1 we seek an indirect bandgap for $LaAlO_3$ by plotting the square root of the absorption coefficient ($\alpha^{1/2}$) *versus* photon energy. This process is also implemented by C.K. Kwok and C.R. Aita[52] to observe an indirect band gap in ZrO_2.

The real part of the frequency-dependent electrical conductivity $\sigma(E)$ is described by[38].

$$\mathrm{Re}\,\sigma(E) = \frac{2\pi e^2\hbar^3\Omega}{m^2}\int N_v(E')N_c(E'+E)|P_{cv}|^2 dE'/E \tag{159}$$

Where $N_v(E')$ is the density of the initial states, and $N_c(E'+E)$ is the density of the final states. $|P_{cv}|^2$ is the squared momentum-matrix element, and Ω is the volume of the specimen. The absorption coefficient $\alpha(E)$ is defined through electromagnetic theory in terms of $\mathrm{Re}\,\sigma(E)$ as

$$\alpha(E) = \frac{4\pi}{n(E)c}\,\mathrm{Re}\,\sigma(E) \tag{160}$$

with the refractive index of the material as $n(E)$ and c as the light velocity in vacuum. By substituting Eq.(159) in Eq.(160) we see that

$$\alpha(E) = \frac{8\pi^2 e^2\hbar^3\Omega}{n(E)cm^2}\int N_v(E')N_c(E'+E)|P_{cv}|^2 dE'/E \tag{161}$$

by assuming that $N(E)$ behaves like some power of E at the extremity of the band we find

$$N_c(E) = N_c^0[(E - E_c)/\Delta E]^{r1} \tag{162a}$$

$$N_v(E) = N_v^0[(E_v - E)/\Delta E]^{r2} \tag{162b}$$

where ΔE is the band-tail widths due to disorder seen in Fig(7). If the bands are identical so that $r1 = r2 \equiv r$, $N_c^0 = N_v^0$, and $\Delta E_c = \Delta E_v \equiv \Delta E$ and $|P_{cv}|^2$ is assumed to be energy-independent then

$$\alpha(E) = \frac{8\pi^2 e^2\hbar^3\Omega|P_{cv}|^2}{n(E)cm^2}\,2\int(N_c^0)^2[(E_v - E)(E - E - E_c)/(\Delta E)^2]^r dE'/E \tag{163}$$

Eq.(125) can be modified so that

$$\alpha(E) = \frac{16\pi e^2\hbar^3\Omega|P_{cv}|^2}{n(E)cm^2}\,\frac{(E - E_v - E_c)^{2r+1}}{E(\Delta E)^{2r}}\,\frac{[\Gamma(r+1)]^2}{\Gamma(2r+2)} \tag{164}$$

where $[\Gamma(r+1)]^2/\Gamma(2r+2)$ is a solution of the integral in Eq.(163).

If the distribution is parabolic as in a crystal r = ½, however Davis and Mott[39] assumed that N(E) ~ E at the band edges. The Davis-Mott expression has r = 1 so that

$$E\alpha(E)\mathrm{n}(E) = \frac{8\pi e^2\hbar^3\Omega|\,\mathrm{P}_{cv}|^2}{3cm^2(\Delta E)^2}(E - E_0)^3 \tag{165}$$

and the value of the optical band gap E_0 depends greatly on the theoretical model used. Unfortunately, there is no well-established physical model because of the complexity of the electronic states in disordered systems.

3.2.2 Dielectric Function Model

This section will extend the Model Dielectric Function established by Tauc, Grigorovici, and Vancu[40,41]. In this model $\varepsilon_2(E)$ is assumed to yield a continuous absorption obeying the power law of $1/E^2(E - E_0)^2$ and also have a steep high-energy end at the high-energy cutoff E_{hc}. Also $\varepsilon_1(E)$ has clear structures both at the E_0 and at the E_{hc} edges. By introducing the damping effect in to model, the optical spectra become structureless which are typically observed in amorphous semiconductors.

As stated in the first part of Section 3.1.5 the optical transitions in amorphous semiconductors are described, to a first approximation, by the nondirect transition model in which the conservation of energy but not wave vector is significant. Tauc[40-41] obtained a linear variation of $E\varepsilon_2(E)$ by assuming that the conduction and valence bands are parabolic

$$E\varepsilon_2(E)^{1/2} = D_a^{1/2}(E - E_0)H(E - E_0) \tag{166}$$

with D_a as the nondimensional strength parameter and H(z) as the Heaviside function defined as

$$H(z) = \begin{cases} 1 & \text{for } z \geq 0 \\ 0 & \text{for } z < 0 \end{cases} \tag{167}$$

now from Eq.(166) we find

$$\varepsilon_2(E) = (D_a/E^2)(E - E_0)^2 H(E - E_0) H(E_{hc} - E) \tag{168}$$

Assuming that the strength parameter D_a is independent of the photon energy, the Kramers-Kronig transformation gives

$$\varepsilon(E) = 1 + \frac{2D_a}{\pi}\left[-\frac{E_0^2}{(E+i\Gamma)^2}\ln\left(\frac{E_{hc}}{E_0}\right) + \frac{1}{2}\left(1+\frac{E_0}{E+i\Gamma}\right)^2 \ln\frac{E+i\Gamma+E_{hc}}{E+i\Gamma+E_0} + \frac{1}{2}\left(1-\frac{E_0}{E+i\Gamma}\right)^2 \ln\frac{E+i\Gamma+E_{hc}}{E+i\Gamma+E_0}\right] \tag{169}$$

the damping effect (Γ) is taken into consideration in a manner such that ($E \rightarrow E + i\Gamma$).

If we take into consideration the Davis-Mott cubic law as shown in Eq.(165) then we obtain

$$\varepsilon_2(E) = (D_a/E^2)(E - E_0)^3 H(E - E_0) H(E_{hc} - E) \tag{170}$$

the Kramers-Kronig transformation of Eq.(132) gives an expression for both $\varepsilon_1(E)$ [Re $\varepsilon(E)$] and $\varepsilon_2(E)$ [Im $\varepsilon(E)$]

$$\varepsilon(E) = 1 + \frac{2D_a}{\pi}\left[(E_{hc} - E_0) + \frac{E_0^3}{(E+i\Gamma)^2}\ln\left(\frac{E_{hc}}{E_0}\right) - \frac{E+i\Gamma}{2}\left(1+\frac{E_0}{E+i\Gamma}\right)^3 \ln\frac{E+i\Gamma+E_{hc}}{E+i\Gamma+E_0}\right.$$
$$\left. + \frac{E+i\Gamma}{2}\left(1-\frac{E_0}{E+i\Gamma}\right)^3 \ln\frac{E+i\Gamma+E_{hc}}{E+i\Gamma+E_0}\right] \tag{171}$$

The strength parameter D_a in the MDF model, for pair states between the conduction and valence bands, is taken to be constant. This assumption is generally seen in the theory of optical properties of crystals, if D_a is a proper function of energy the fit would be improved. However, to confirm the energy dependence it would require an exact electronic energy-band structure of amorphous materials.

Chapter 4

Samples Preparation

4.1 Single Crystal Bulk samples

The single crystal bulk samples, $DyScO_3$ and $GdScO_3$, were grown using the automated Czochralski technique with RF-induction heating[42]. For starting materials pre-dried powders of Dy_2O_3, Gd_2O_3, and Sc_2O_3 were mixed in the stoichiometric ratio, pressed, and sintered at approximately 1400°C for 15 hours. An afterheater and crucible made of iridium were used due to $DyScO_3$ and $GdScO_3$ high melting temperatures of approximately 2100°C. The grown atmosphere consisted of either nitrogen or argon. Initial seed crystals of $DyScO_3$ and $GdScO_3$ were not available; therefore the early experiments were done using an iridium seed rod. Both $DyScO_3$ and $GdScO_3$ have a tendency to grow in large single crystalline grains, therefore these early stage experiments provided suitable seeds. The pulling rate for both crystals was 1.5-2 mm/hour and the rotation was 10/min. The $DyScO_3$ was pulled along the [010] orientation and the $GdScO_3$ was pulled along the [001] orientation. Figure 8 shows the two crystals which were 35-50 in length and 18 mm in diameter. As shown the $DyScO_3$ has a light yellow tint and the $GdScO_3$ was colorless.

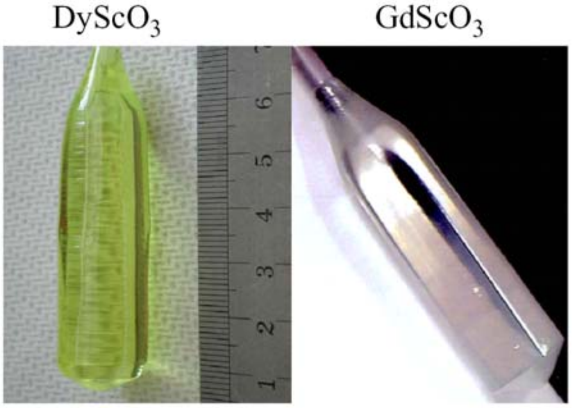
$DyScO_3$ $GdScO_3$

Figure 8:$DyScO_3$ and $GdScO_3$ crystals

4.2 Epitaxial and Amorphous films on MgO

Both epitaxial and amorphous films of $LaScO_3$, $GdScO_3$, and $DyScO_3$ were grown by pulsed laser deposition (PLD). The process utilized a KrF excimer laser with a wavelength of 248 nm, a pulse width of 20 ns, and a fluence of 2.5 J/cm^2. The starting materials were targets made from sintered powder of stoichometric composition. The thin films were deposited in an on-axis geometry, in which the substrate is centered in the PLD plasma plume. This allows for a high-deposition rate with a limited area of uniformity, approximately 1x1 cm^2. MgO (100) was used as a substrate with a 10 nm thick $BaTiO_3$ interlayer, which is necessary for epitaxial growth on MgO. The substrates were place directly onto a SiC resistive heater with an oxygen gas partial pressure of $2\text{-}10^{-3}$ mbar maintained during the deposition. For epitaxial growth of $LaScO_3$ and $GdScO_3$ the MgO substrate was held at a substrate temperature of 750°C, and for epitaxial growth of $DyScO_3$, the substrate temperature was held at 850°C during deposition.

4.3 Epitaxial Films on $LaAlO_3$

The entire rare earth scandate serious including: $DyScO_3$, $SmScO_3$, $HoScO_3$, $TbScO_3$, $PrScO_3$, $NdScO_3$, $GdScO_3$, $LaScO_3$, and also alloys of: $SrTiO_3/LaAlO_3$, $GdScO_3/LaAlO_3$, $LaScO_3/LaAlO_3$, $LaMgZrO/LaAlO_3$ were grown on top of (100) $LaAlO_3$ single crystal substrates by Hans Christen at Oak Ridge National Laboratory. These films were grown by pulsed laser deposition (PLD). A substrate heater with a built-in temperature gradient was used so that the effect of the substrate/crystallization temperature could be seen.

4.4 Amorphous Films on Si

Films of $LaScO_3$ were deposited by MBD on Si (100) substrate[43]. The amorphous $LaScO_3$ films were grown by molecular-beam depositon (MBD) in an EPI 930 molecular-beam epitaxy chamber modified for the growth of oxides. The films were grown on n- and p-type Si (001) wafers. The native SiO_2 on the silicon wafer was thermally removed in UHV at a temperature of 900°C, measured with an optical pyrometer. Two films had nominal thicknesses of 30 nm and 100 nm. The thicknesses were determined by calibrating the fluxes using a quartz crystal microbalance and assuming the films had the bulk density of single crystal $LaScO_3$.

The amorphous $LaAlO_3$ films were grown by molecular-beam depositon (MBD) in an EPI 930 molecular-beam epitaxy chamber modified for the growth of oxides. The films were grown on n- and p-type Si (001) wafers. The native SiO_2 on the silicon wafer was thermally removed in UHV at a temperature of 900°C, measured with an optical pyrometer. The films were grown using elemental sources. Lanthanum, aluminum, and molecular oxygen (99.994% purity) at a background pressure of 6×10^{-8} Torr were codeposited at a thermocouple temperature of ~100°C onto the clean 2×1 Si surface. The lanthanum and aluminum fluxes were each 2×10^{13} atoms/cm^2s. As with the $LaScO_3$, the thicknesses of the $LaAlO_3$ films were calibrated assuming the films had the density of bulk single crystal material, in this case, single crystal $LaAlO_3$.

Chapter 5

High-k Dielectric

5.1 $LaScO_3$

5.1.1 Results and Discussion of MBD $LaScO_3$

Within the UV/Visible wavelength range, the films are transparent. A Sellmeir model was used for the fit with film thickness as the other parameter. The Sellmeir fit is defined by: $n^2 = A_n + (B_n 8^2 / (8^2 – C_n^2))$, $k = 0$; the values we obtain for these parameters are shown in Table 1. The index parameter values agree within error bars. For an example of the fit, a comparison of theory and experiment is shown in Figure 9 for the thick sample. Figure 10 shows the index of refraction for both films.

Table 1: Sellmeir parameters for MBD $LaScO_3$

Film	Thickness (nm)	An	Bn	Cn (nm)
Thin	39.6 ± 0.2	3.42	0.32	245.58
Thick	141.3 ± 2	3.26	0.48	229.76

By extending our energy range we saw both the transparent and absorbing behavior of the MBD $LaScO_3$ films on Si, and therefore a Sellmeir fit would no longer give an accurate account of the dielectric response. We instead fit the data point-by-point. For the initial analysis, the dielectric response was assumed to be identical to that of single-crystalline $LaAlO_3$[44]. The next step was to fix the thickness and let *n* and *k* vary from the single-crystalline values to better fit the experimental values. In this way, since we measured data at N wavelengths, we calculate 2N parameters (n and k) from our 2N data points (tanΨ(8) and cosΔ(8)). Note that we must fix thickness to avoid

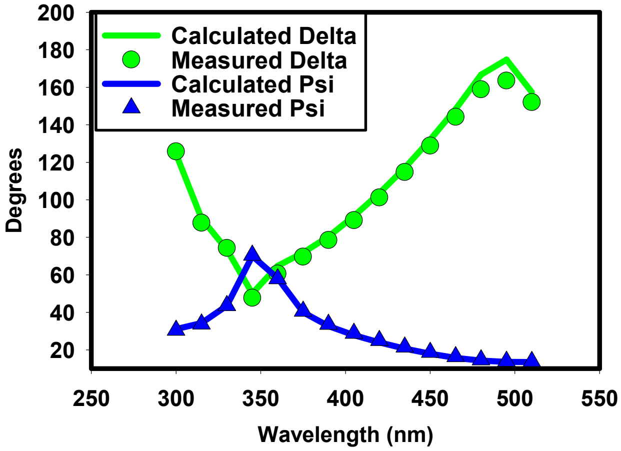

Figure 9. Calculated (solid) and measured (symbols) ellipsometric parameters for the nominally 100 nm thick LaScO3/Si film using a Sellmeir fit for the refractive index.

having more unknowns than data points. This was done under various assumptions, including a single layer of amorphous $LaScO_3$ on Si, a mixed interface between the amorphous $LaScO_3$ and the Si substrate, a SiO_2 interlayer between the amorphous $LaScO_3$ and the Si substrate, and a reduced density surface layer on the amorphous $LaScO_3$. By assuming a single layer of amorphous $LaScO_3$ the comparison between data and simulation is fairly good as seen in Figure 11. With every point calculated independently,

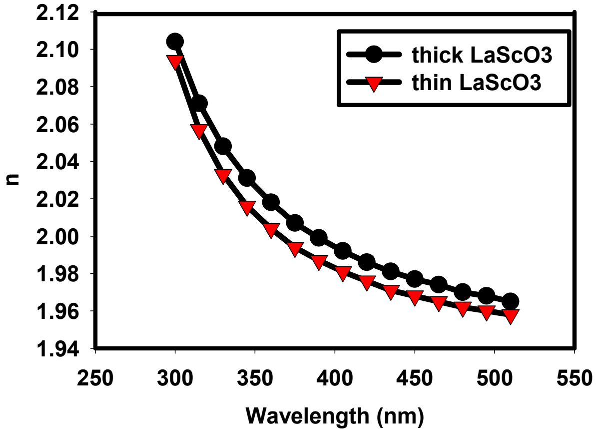

Figure 10. Best fit refractive index for the nominally 30 nm and the nominally 100 nm LaScO3/Si films using a Sellmeir fit.

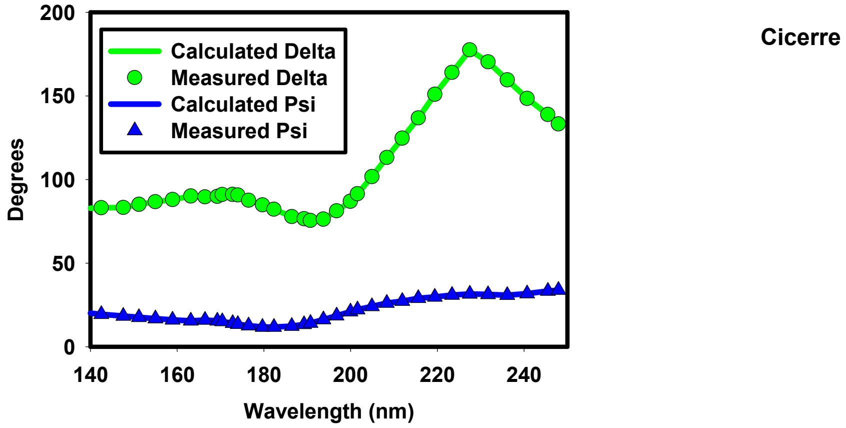

Figure 11. Measured (solid) and calculated (symbols) ellipsometric angles for the nominally 30 nm LaScO3 film assuming 34 nm thickness.

accurate results are shown as a smooth and continuous dielectric constant. An incorrect thickness will result in discontinuous inferred dielectric response and/or the imposition of critical points of the substrate upon the dielectric response inferred for the overlayer[45-46]. Such an approach does not force Kramers-Kronig consistent results, however, as would be the case for fitting to some model dielectric function. For the thinner films, this approach worked very well, and we calculated a thickness that is 5 nm less than was inferred by the Sellmeir fit.

The thick film required more than just a single layer model in our analysis of the high photon energy data. To get an adequate result a surface layer of reduced density was added. The layer model was: Si substrate, then an 85 nm thick full material density layer, and top layer was 40.58 nm thick with a void fraction of 18%. Therefore the total thickness came to 125.6 nm. This differs significantly from the value of 141 nm that the visible spectrum alone gave us.

These two analyses resulted in discrepancies in the thickness for both the thin and thick films. For the thin film there was an 11% difference and for the thick film there was a 13% difference. This may be explained by the fact that the visible spectrum method failed to recognize the second, lower density layer. As defined by its bulk, crystalline density the thin film had a nominal thickness of 30 nm, which is 15% less than what was found. The thick film was predicted by its bulk crystalline density to have a thickness of 100 nm which was again 18% less than what was found.

The next step in our analysis was to determine the band gap. We use the results of these fits to obtain k as a function of wavelength, and then calculate alpha (∀ = 4B k/8). In Figure 12 alpha for both the thin and thick films are shown; notice that for energies under 6 eV the values for the thin film are larger than those for the thick film.

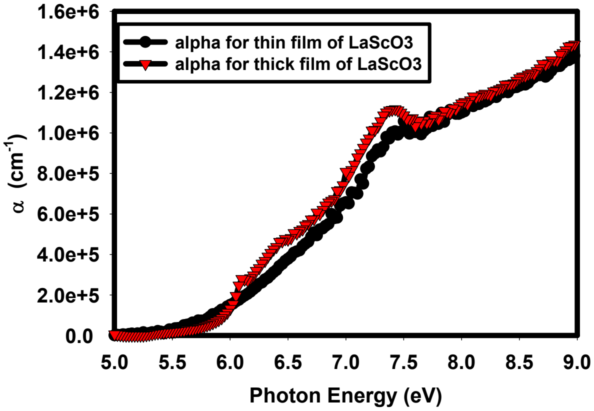

Figure 12. Absorption coefficient for the nominally 30 nm, and the nominally 100 nm films of LaScO3 films on Si.

With a direct band gap material, a plot of $\forall^2$ *versus* photon energy should give us a line that intercepts the energy axis at the value of the band gap. The results from the thin film indicate that there are two linear ranges that lead to band gaps of 5.5 eV and 5.99 eV. With the thick film we only observe a linear region leading to the higher band gap of 5.96 eV. These results imply that the thinner film has the lower band gap of 5.5 eV, and that both the thin and thick films have a strong absorption band gap at around 6 eV. In Figure 13, $\forall^2$ and the linear fit to

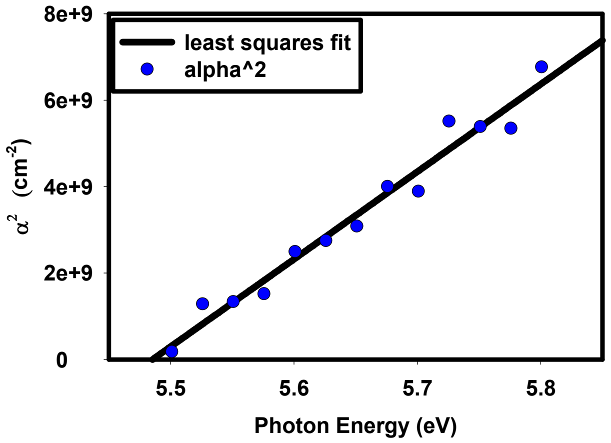

Figure 13. α² (•) *versus* photon energy for the nominally 30 nm $LaScO_3$ film. Also plotted is the least squares fit line (solid) leading to E_G = 5.50 eV.

∀² for the lower band gap of the thin film is shown. In Figure 14, the higher bandgap for the thin film and the bandgap for the thick film are shown.

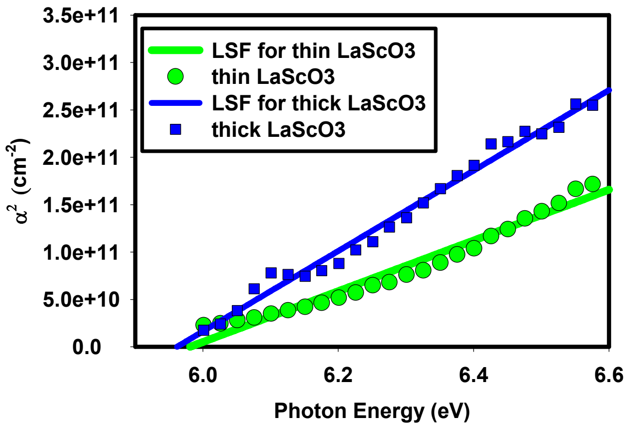

Figure 14. α² *versus* photon energy for both the nominally 30 nm (•) and the nominally 100 nm (▪) $LaScO_3$ films. Also plotted are the least squares fit lines (solid) leading to E_G ≈ 6 eV for both films.

5.1.2 Results and Discussion of PLD $LaScO_3$ on MgO

In addition to the films on Si substrates, we also studied both epitaxial and amorphous $LaScO_3$ films deposited on MgO by pulsed laser deposition[47]. Both films were 1.5 μm thick; epitaxial films were deposited on substrates at elevated temperature whereas the amorphous films were deposited on substrates held at room temperature. Transmission of these films was measured from 2 eV to 6.2 eV. As shown in Figure 15, the transmission measurements show that the two

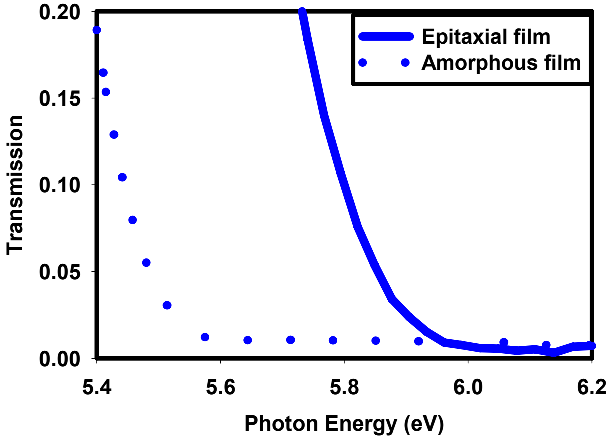

Figure 15. Transmission spectra of nominally 1.5 micron thick films of epitaxial (solid) and amorphous (dotted) LaScO3 deposited upon MgO substrates by pulsed laser deposition.

films have different band gaps. The onset of transmission for the epitaxial film is over 5.8 eV, as compared to the amorphous film that has an onset around 5.5 eV. At this thickness a transmission of 20% implies a an absorption coefficient $\alpha = 10^4$ cm^{-1}, which means the onset of visible transmission occurs in the region of $10^4 < \alpha < 10^5$ cm^{-1}.

5.1.3 Results and Discussion of PLD $LaScO_3$ on $LaAlO_3$

The PLD $LaScO_3$ data was fitted point-by-point as discussed in section 5.1.1, with the thick $LaScO_3$ film dielectric response used for the initial analysis.

For this film it was essential to use a multilayer system for the analysis of the high photon energy data. To get an adequate result a surface layer of reduced density was added. The layer model was: $LaAlO_3$ substrate, then a 400.0 nm thick full material density layer, and top layer was .12 nm thick with a void fraction of 30%. Figure 16 shows the comparison between the measured and calculated data. The

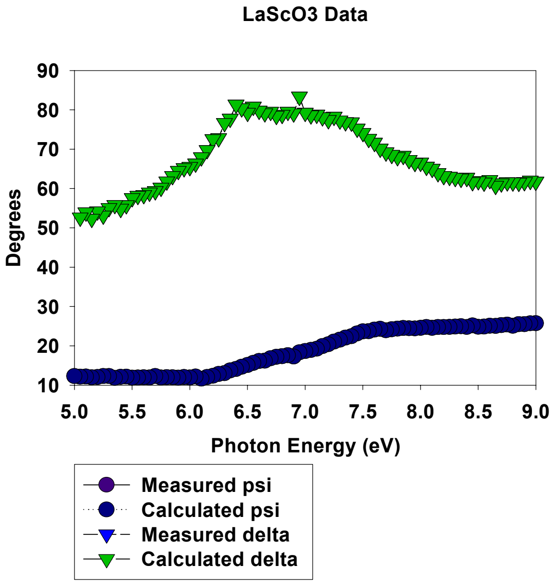

Figure 16. Comparison between calculated and measured data for the $LaScO_3$ film on Single Crystal $LaAlO_3$ substrate

real (n) and imaginary (k) parts of the complex refraction index are shown in Figure 17. The linear fit to α^2 shows a bandgap of 5.72eV, this is shown in

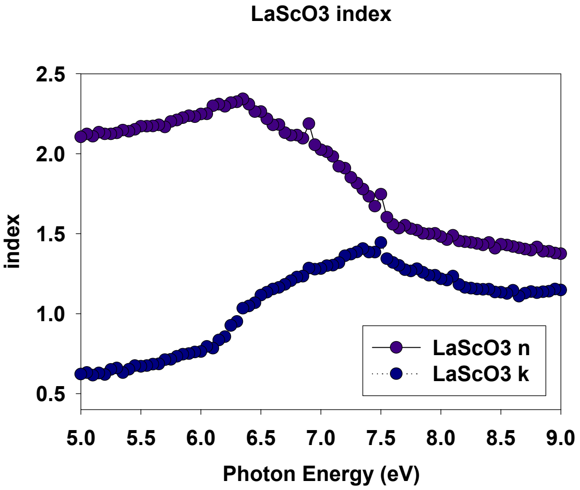

Figure 17. Complex refractive index for $LaScO_3$ film on $LaAlO_3$ single crystal substrate.

Figure 18, which is concurrent with the bandgap value obtained from the transmission measurement done on the previous epitaxial film.

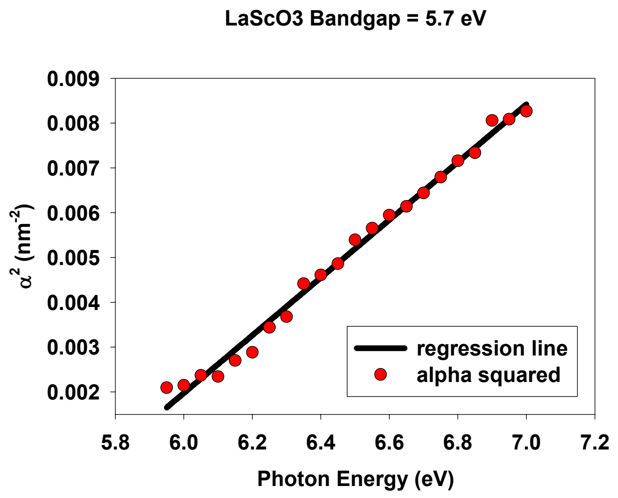

Figure 18. α^2 (●) *versus* photon energy for the $LaScO_3$ film on $LaAlO_3$. Also plotted is the least squares fit line (solid) leading to E_G = 5.7 eV.

5.1.4 Results and Discussion of PLD $LaScO_3$/$LaAlO_3$ alloy

A true $LaScO_3$/$LaAlO_3$ alloy was deposited on the single crystal $LaAlO_3$ substrate. The point-by-point analysis technique was used, assuming the initial dielectric respond was identical to the $LaScO_3$ film on $LaAlO_3$ substrate. The analysis showed that the film was 144 nm with a surface roughness layer of 12 nm with a 42 % void fraction. Figure 19 shows the comparison between the measured and calculated data. The real

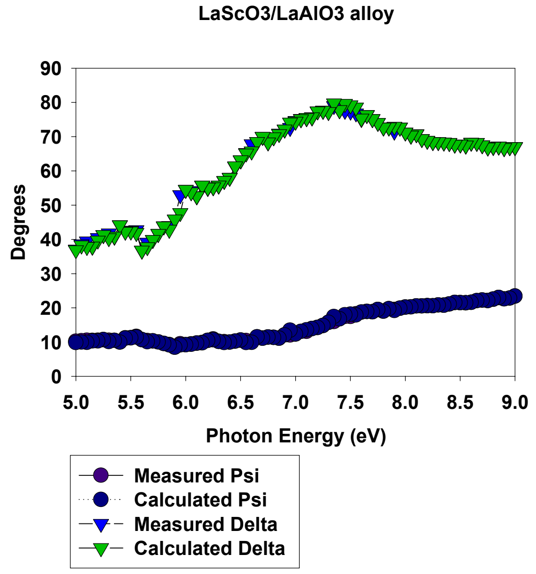

Figure 19. Comparison between calculated and measured data for the $LaScO_3$/$LaAlO_3$ alloy film on Single Crystal $LaAlO_3$ substrate

(n) and imaginary (k) parts of the complex refraction index are shown in Figure 20. The linear fit to α^2 shows a bandgap of 6.8 eV, this is shown in Figure 21.

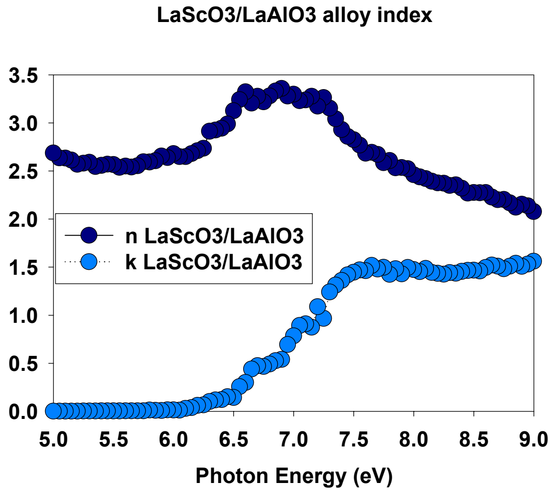

Figure 20. Complex refractive index for $LaScO_3$ / $LaAlO_3$ alloy film on $LaAlO_3$ single crystal substrate.

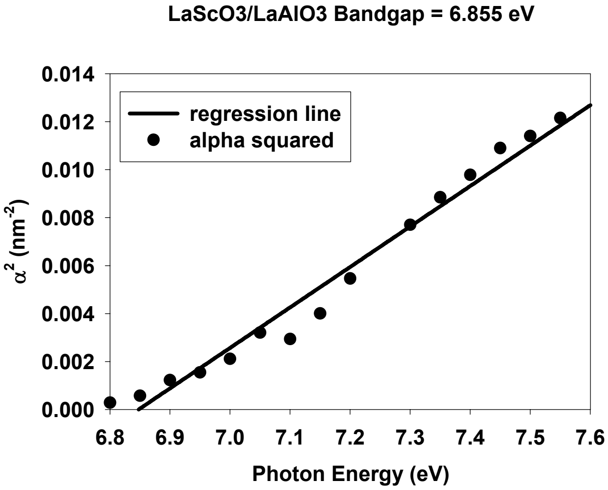

Figure 21. α^2 (•) *versus* photon energy for the $LaScO_3$ /$LaAlO_3$ alloy film on $LaAlO_3$. Also plotted is the least squares fit line (solid) leading to E_G = 6.855 eV.

The next set of graphs, Figure 22 and 23, compare the index values of the $LaScO_3/LaAlO_3$ alloy with the $LaScO_3$ film and the $LaAlO_3$ substrate values.

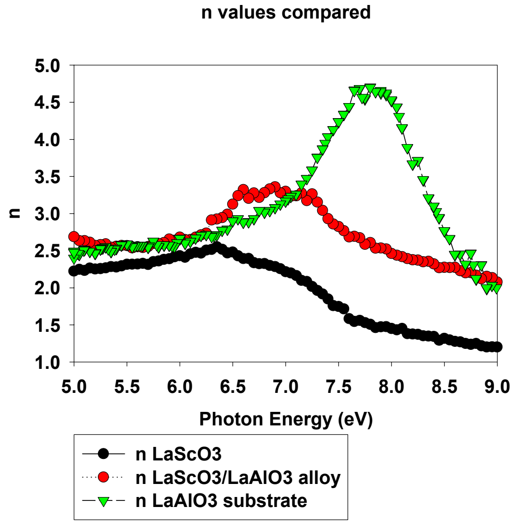

Figure 22. n values compared for $LaScO_3$ / $LaAlO_3$ alloy film, $LaScO_3$ and the $LaAlO_3$ single crystal substrate.

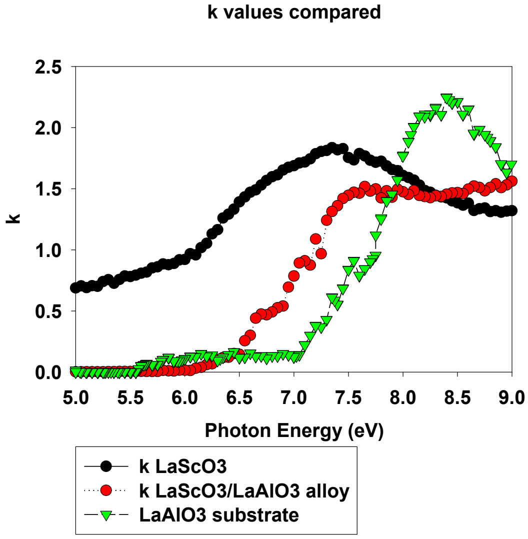

Figure 23. k values compared for $LaScO_3$ / $LaAlO_3$ alloy film, $LaScO_3$ and the $LaAlO_3$ single crystal substrate.

5.2 $LaAlO_3$

5.2.1 Results and Discussion of MBD $LaAlO_3$

We will now discuss thin films of amorphous $LaAlO_3$, which were grown by molecular beam deposition[48] on a silicon substrate. The first sample we studied was an amorphous $LaAlO_3$ film on silicon with a nominal thickness of 300 nm. For the initial analysis, we fit the data point-by-point as described previously in the Results and Discussion section of MBD $LaScO_3$. The comparison between data and simulation is fairly good as seen in Figure 24.

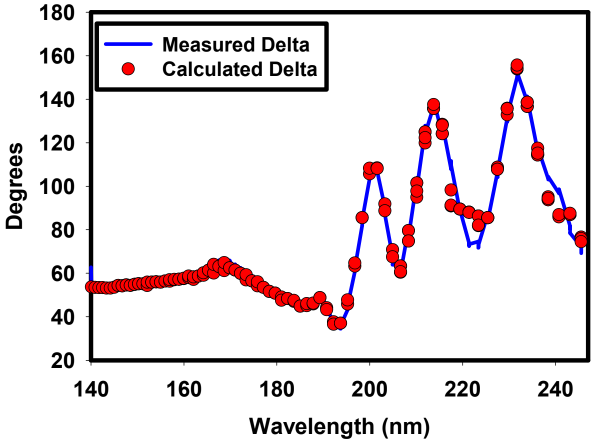

Figure 24. Comparison between calculated(●) and measured (solid) data for the nominally 300 nm thick LaAlO3/Si sample.

The real (n) and imaginary (k) parts of the complex refractive index is shown in Figure 25. Using this fit we can again determine the band gap. In Figure 26 we show a plot of α^2 vs. photon energy which indicates a direct band gap of 6.33 eV.

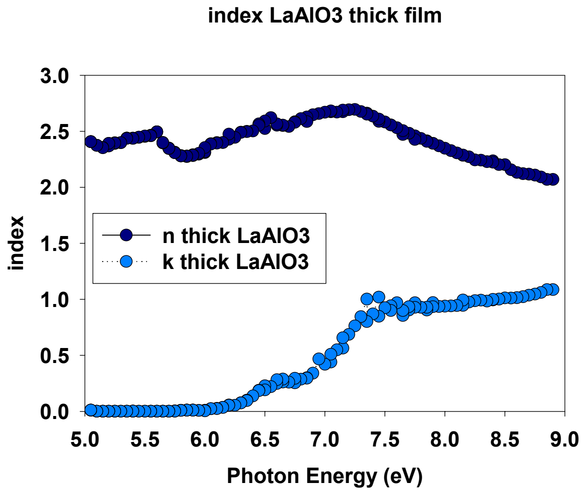

Figure 25. Complex refractive index for $LaAlO_3$ nominally 300 nm thick film

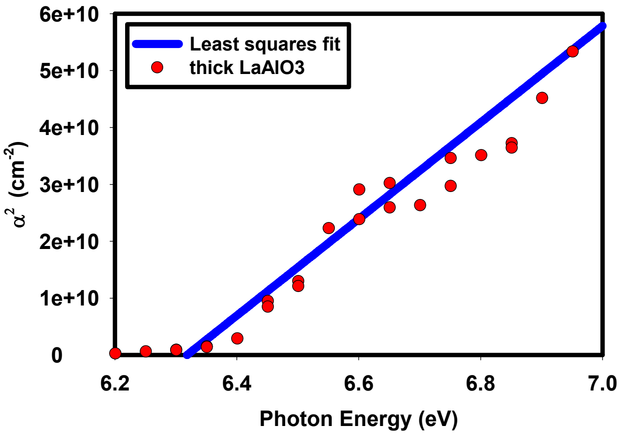

Figure 26. Least squares fit (solid) to data (●) for the nominally 300 nm thick LaAlO3/Si assuming a band gap of 6.33 eV.

This value is in reasonable agreement with Lu *et al.*[49], who found a band gap of 6.55 eV for amorphous $LaAlO_3$ on fused silica.

The final sample we discuss is a 30 nm amorphous $LaAlO_3$ film on Si. The comparison between model and experiment was fairly good as seen in Figure 27. The real (n) and imaginary (k) parts of the complex refractive index is shown in Figure 28.

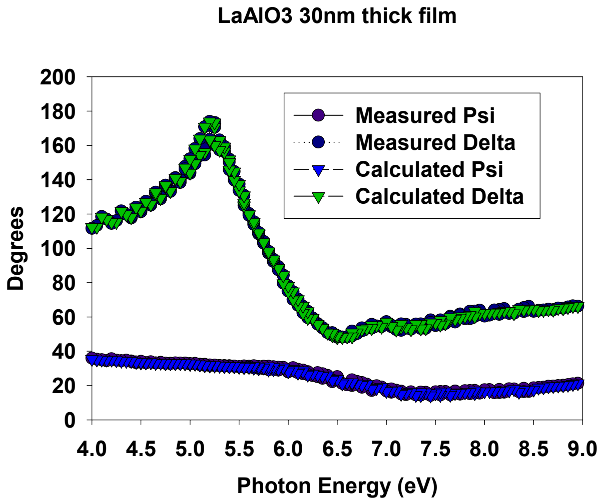

Figure 27. Comparison between calculated and measured data for the nominally 30 nm thick LaAlO3 on Si sample.

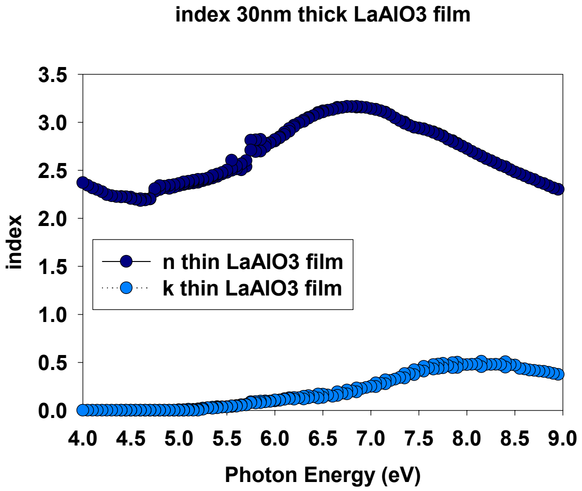

Figure 28. Complex refractive index for $LaAlO_3$ nominally 30 nm thick film

Again we calculate alpha (∀ = 4B k/ 8) to determine the band gap, and attempt to fit $\forall^2$ to a straight line. Using the lower energy points, we attempt to fit a band gap value close to those of bulk $LaAlO_3$ which is 5.8 eV. We find a good linear fit for a band gap of 5.84 eV. This is substantially less than we found for the thick film.

We investigated further, and added tests for indirect band gaps to our studies. In this case, we sought linear regions for a plot of $\alpha^{1/2}$ *versus* photon energy. We found a region with a good fit to $\alpha^{1/2}$ for this thin film leading to an inferred indirect bandgap of 5.0 eV, seen in Figure 29.

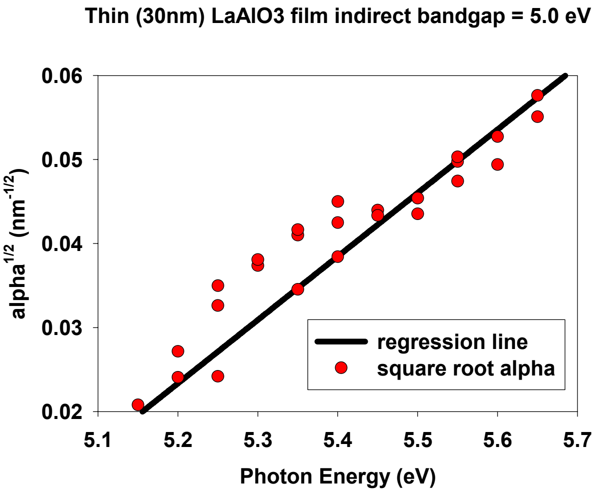

Figure 29. Least squares fit (solid) to data (•) for the nominally 30 nm thick LaAlO3/Si leading to indirect bandgap of 5.0 eV.

We also found a fit for an indirect bandgap of 5.7 eV for the thick film, seen in Figure 30, although the standard deviation was twice as great in this case. The absorption coefficient magnitude (in the photon energy range in which we are

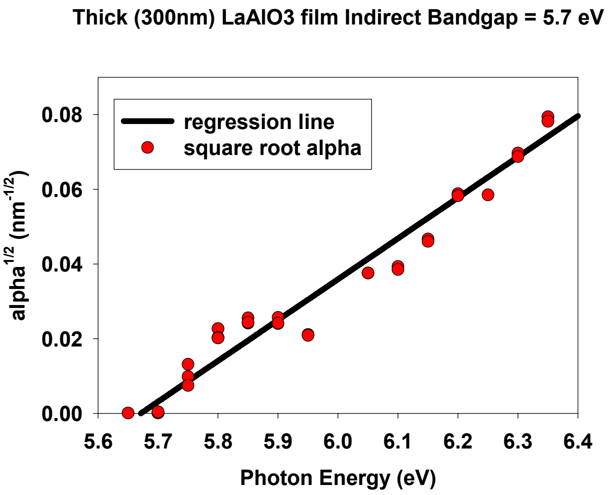

Figure 30. **Least squares fit (solid) to data (•) for the nominally 300 nm thick LaAlO3/Si leading to indirect bandgap of 5.7 eV.**

fitting) is typically over 10,000 cm^{-1}; this magnitude is similar to that observed for GaAs at 1.5 eV[50,51]. We note that C. K. Kwok and C. R. Aita[52] observed an indirect band gap in ZrO$_2$ with similar levels of absorption. Their data was taken by transmission and reflectance spectroscopy.

As shown in Figure 31, we see differences in α between thin and thick

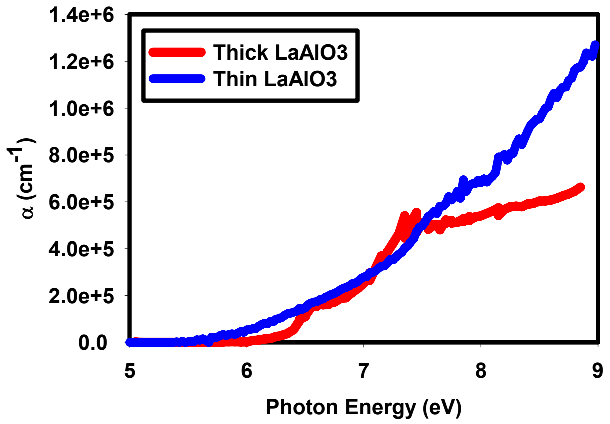

Figure 31. Absorption coefficient for the nominally 30 nm and 300 nm thick films of LaAlO3 films of Si.

films that are quite similar to those discussed earlier for the $LaScO_3$ films and illustrated in Figure 12; in both cases the thinner film exhibits higher absorption at the lowest energies, whereas the thicker films become more absorbing at higher photon energies. We must conclude that the optical response of these films also depends significantly upon the thickness. We note that the scandate films did NOT exhibit indirect band gaps.

5.2.2 Results and Discussion of Single Crystal $LaAlO_3$ substrate

The substrate used as a substrate for many of the scandate materials studied in this chapter, is (100) $LaAlO_3$ Single Crystal. We fit the data point-by-point. For the initial analysis, the dielectric response was assumed to be identical to that of single-crystalline $LaAlO_3$[44]. We found that a single substrate layer was not giving sufficient results, by adding a surface roughness layer to the model adequate results were found, as seen in Figure 32. The surface roughness layer was found to be approximately 9nm with a 22% void fraction. The index values obtain for the single crystal $LaAlO_3$ substrate were then compared to the index values of both

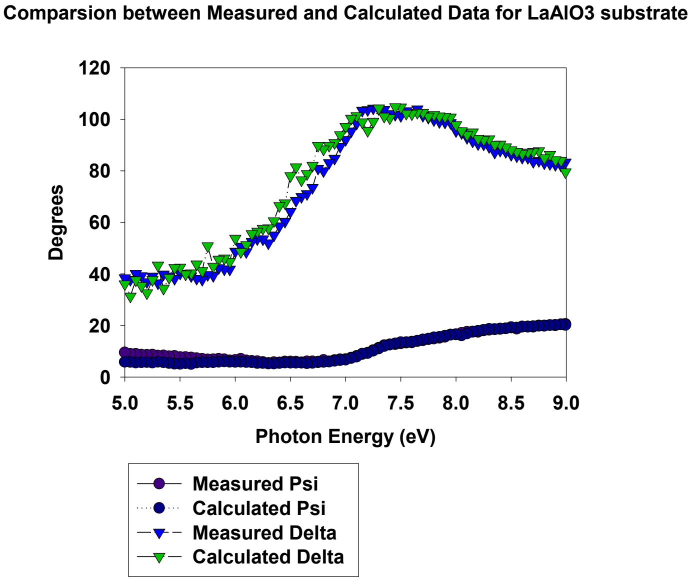

Figure 32. Comparison between calculated and measured data for Single crystal (100) LaAlO3 substrate.

$LaAlO_3$ film and also from a single crystal $LaAlO_3$ bulk sample[44]. The index comparisons are shown in Figures 33 and 34.

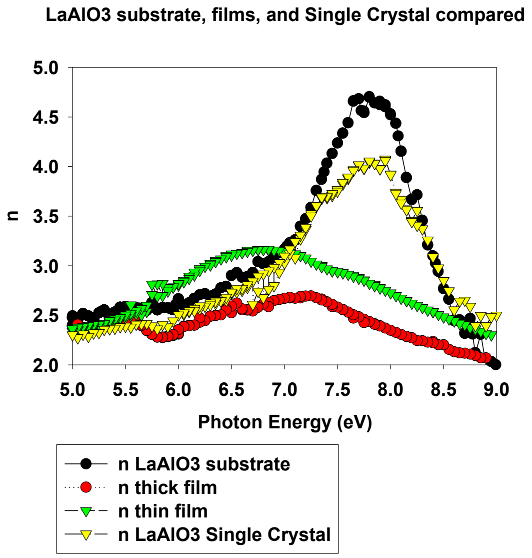

Figure 33. n value for LaAlO3 substrate compared with the n values of the thick (300nm) film, thin (30nm) film, and the single crystal bulk sample.

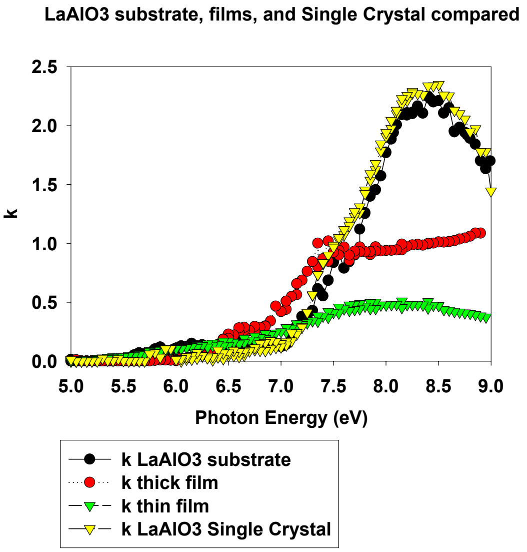

Figure 34. k value for LaAlO3 substrate compared with the k values of the thick (300nm) film, thin (30nm) film, and the single crystal bulk sample.

5.3 $HoScO_3$

5.3.1 Results and Discussion for PLD $HoScO_3$ on $LaAlO_3$

For the $HoScO_3$ film sample we found that the measured data was difficult to fit due to interference fringes at energies below 6.5 eV. To deal with this we incorporated two different models. For energies between 5-6.5 eV we used the Lorentz Oscillator model to compensate for the fringes, and for energies above 6.5 eV a standard NK model was used, with the initial analysis using the dielectric responds of $LaScO_3$. The Lorentz Oscillator model was then converted to a NK model and the two regions were then combined to give the total dielectric response. The measured and calculated data is shown in Figure 35, and the dielectric response is shown in Figure 36. From the model we determined a film thickness of 210.8 nm with a surface roughness layer 15.2 nm with a 56 % void fraction.

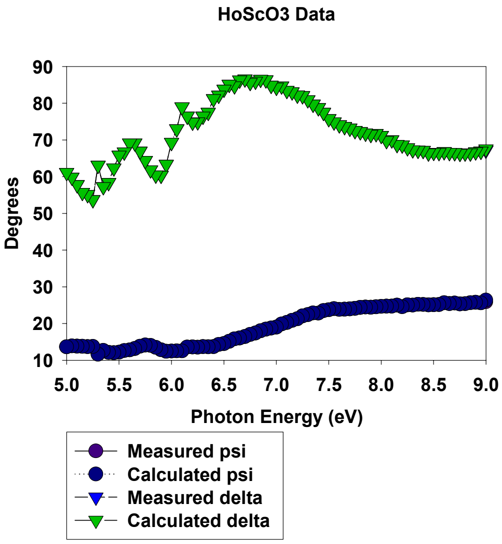

Figure 35. Comparison between calculated and measured data for the HoScO3 film on Single crystal (100) LaAlO3 substrate.

The absorption coefficient alpha (∀) is calculated to determine the band gap. We find a good linear fit to $\forall^2$ leading to a band gap of nearly 5.95 eV, shown in Figure 37.

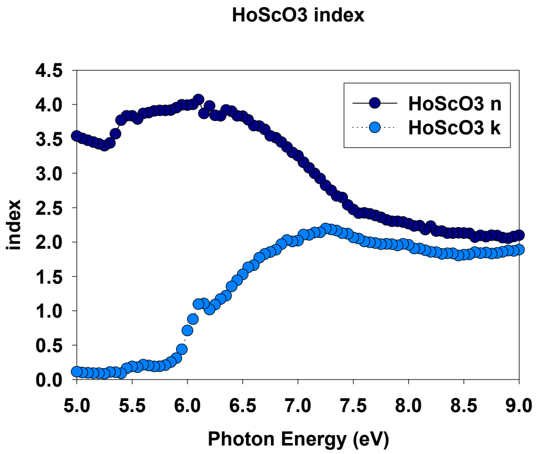

Figure 36. Complex refractive index for $HoScO_3$

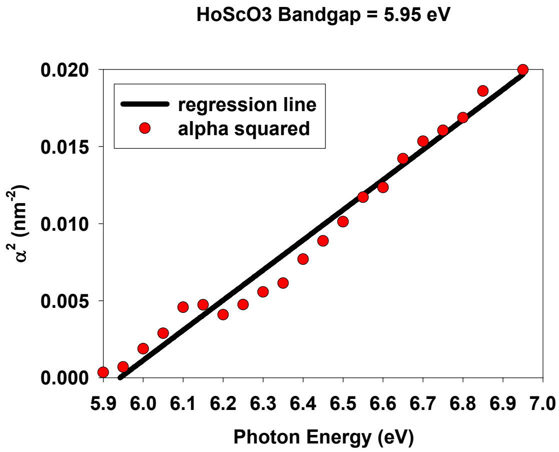

Figure 37. Least squares fit (solid) to data (•) for the HoScO3 film leading to direct bandgap of 5.95 eV.

5.4 $TbScO_3$

5.4.1 Results and Discussion for PLD $TbScO_3$ on $LaAlO_3$

For the $TbScO_3$ film sample we found that the measured data had some slight interference fringes at the lower photon energies, these fringes were not as strong as the ones we saw with the $HoScO_3$ sample. To deal with this we again incorporated two different models. For energies between 5-6.0 eV we used the Lorentz Oscillator model to compensate for the fringes, and for energies above 6.0 eV a standard NK model was use, with the initial analysis using the dielectric responds of $LaScO_3$. The Lorentz Oscillator model was then converted to a NK model and the two regions were then combined to give the total dielectric response. The measured and calculated data is shown in Figure 38, and the dielectric response is shown in Figure 39. From the model we determined a film thickness of 296.2 nm with a surface roughness layer 15.1 nm with a 30 % void fraction. The thinner film thickness may be the reason for the less intense interference fringes, as compared with the fringes seen with the HoScO3 sample.

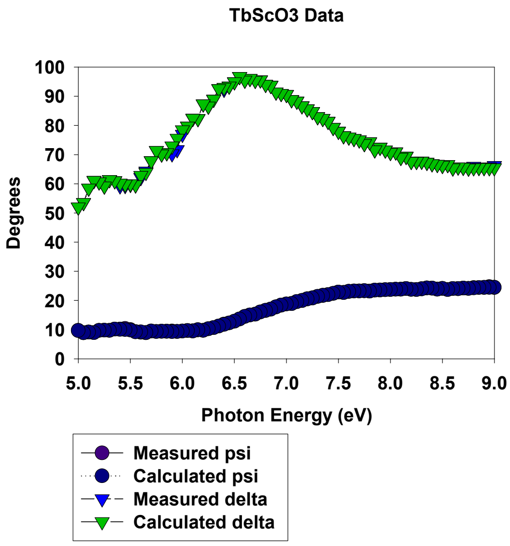

Figure 38. Comparison between calculated and measured data for the TbScO3 film on Single crystal (100) LaAlO3 substrate.

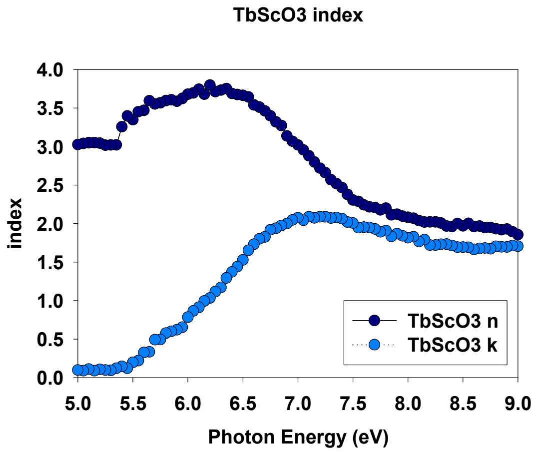

Figure 39. Complex refractive index for $TbScO_3$

The absorption coefficient alpha (∀) is calculated to determine the band gap. We find a good linear fit to $\forall^2$ leading to a band gap of approximately 5.6 eV, shown in Figure 40.

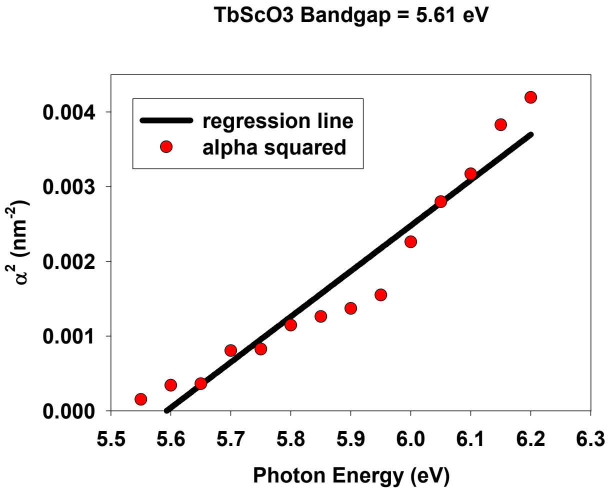

Figure 40. Least squares fit (solid) to data (•) for the TbScO3 film leading to direct bandgap of 5.6 eV.

5.5 $PrScO_3$

5.5.1 Results and Discussion for PLD $PrScO_3$ on $LaAlO_3$

We did not see the low energy interference fringes in the $PrScO_3$ sample as we had for some of the other scandate films on $LaAlO_3$. This may be associated with the thinner film thickness. Using the NK model with the initial analysis assuming a dielectric respond identical to that of $LaScO_3$ we determine a film thickness of 332.4 nm with a surface roughness layer 17.7 nm with a 50 % void fraction. The measured and calculated data is shown in Figure 41, and the dielectric response is shown in Figure 42.

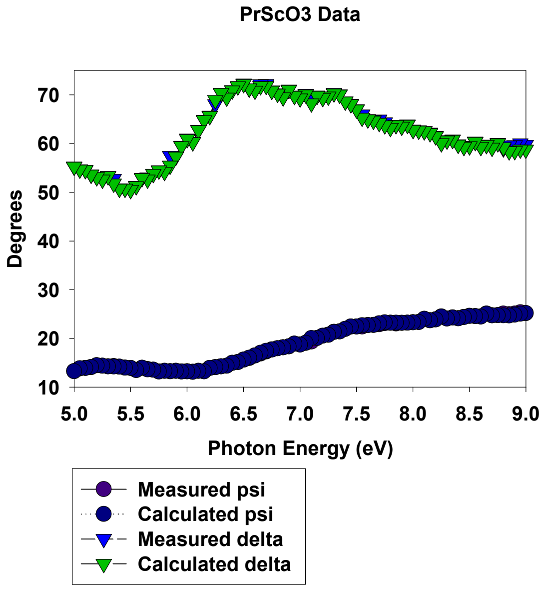

Figure 41. Comparison between calculated and measured data for the PrScO3 film on Single crystal (100) LaAlO3 substrate.

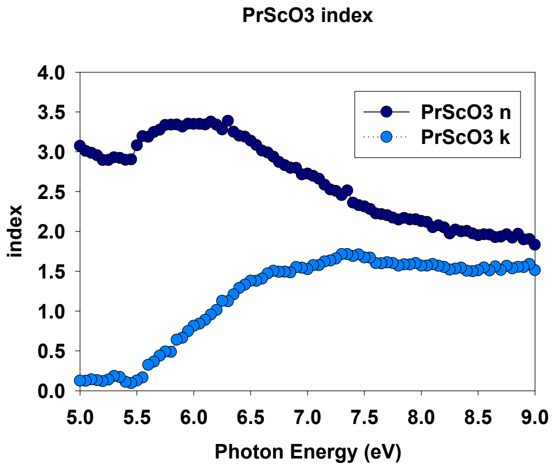

Figure 42. Complex refractive index for $PrScO_3$

The absorption coefficient alpha (∀) is calculated to determine the band gap. We find a good linear fit to $\forall^2$ leading to a band gap of approximately 5.7 eV, shown in Figure 43.

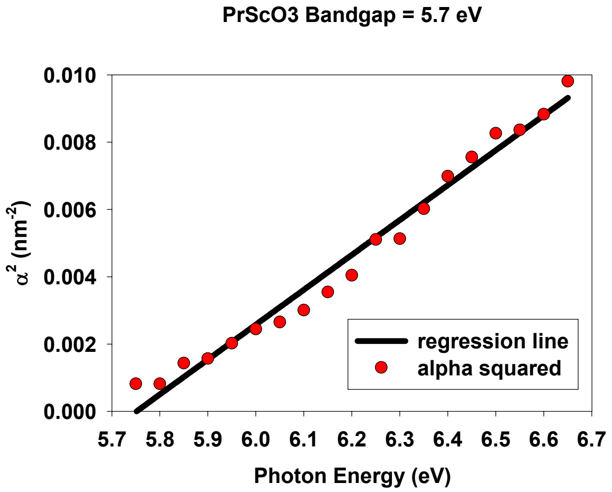

Figure 43. Least squares fit (solid) to data (•) for the PrScO3 film leading to direct bandgap of 5.7 eV.

5.6 $NdScO_3$

5.6.1 Results and Discussion for PLD $NdScO_3$ on $LaAlO_3$

For the $NdScO_3$ film sample we found that the measured data had some slight interference fringes at the lower photon energies, similar to the ones seen from the $TbScO_3$ film. To deal with this we again incorporated two different models. For energies between 5-5.8 eV we used the Lorentz Oscillator model to compensate for the fringes, and for energies above 5.8 eV a standard NK model was use, with the initial analysis using the dielectric responds of $LaScO_3$. The Lorentz Oscillator model was then converted to a NK model and the two regions were then combined to give the total dielectric response. The measured and calculated data is shown in Figure 44, and the dielectric response is shown in Figure 45. From the model we determined a film thickness of 292.6 nm with a surface roughness layer 16.2 nm with a 35 % void fraction. Again we assume the thinner film thickness results in less intense interference fringes.

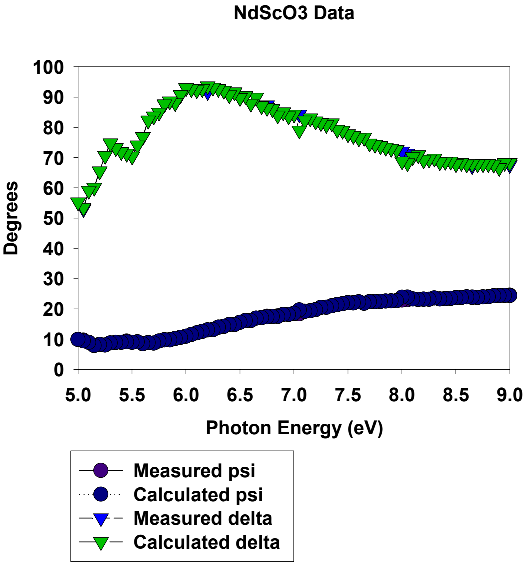

Figure 44. Comparison between calculated and measured data for the NdScO3 film on Single crystal (100) LaAlO3 substrate.

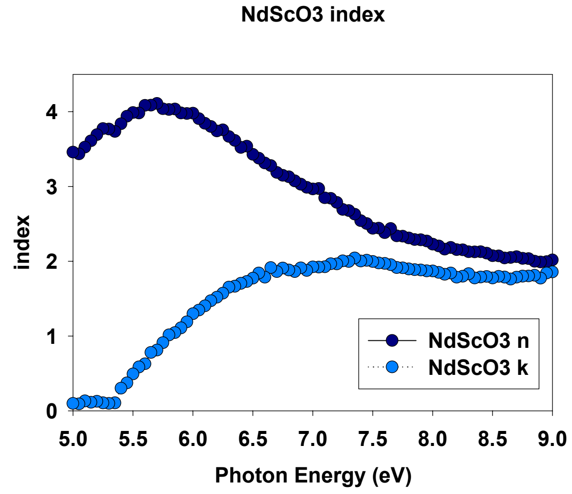

Figure 45. Complex refractive index for $NdScO_3$

The absorption coefficient alpha (∀) is calculated to determine the band gap. We find a good linear fit to $\forall^2$ leading to a band gap of approximately 5.5 eV, shown in Figure 46.

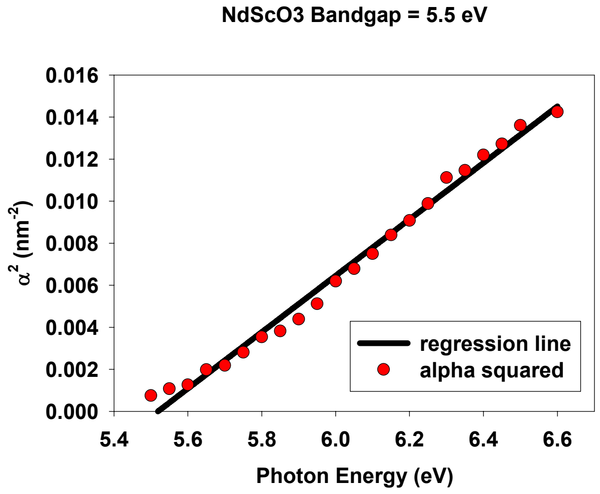

Figure 46. Least squares fit (solid) to data (•) for the NdScO3 film leading to direct bandgap of 5.5 eV.

5.7 $SmScO_3$

5.7.1 Results and Discussion for PLD $SmScO_3$ on $LaAlO_3$

The measured data for the $SmScO_3$ film sample show intense interference fringes at the lower photon energies. The Lorentz Oscillator model was used for energies between 5-6 eV, and for energies above 6 eV the NK model was used. After the conversion of the Oscillator model to the NK values the total dielectric responds was found. The measured and calculated data is shown in Figure 47, and the dielectric response is shown in Figure 48. From the model we determined a film thickness of 355.9 nm with a surface roughness layer 16.3 nm with a 28 % void fraction.

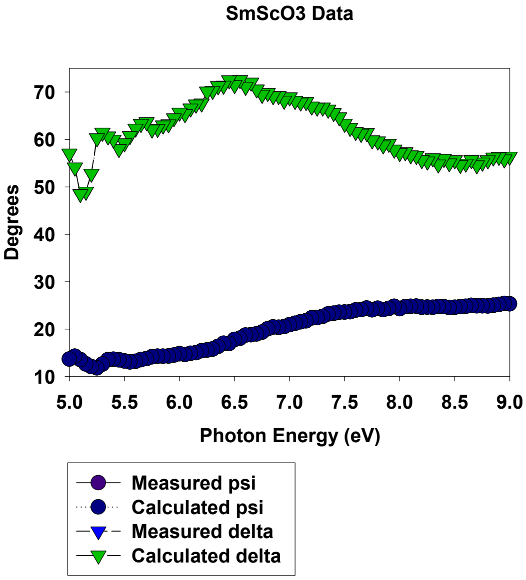

Figure 47. Comparison between calculated and measured data for the SmScO3 film on Single crystal (100) LaAlO3 substrate.

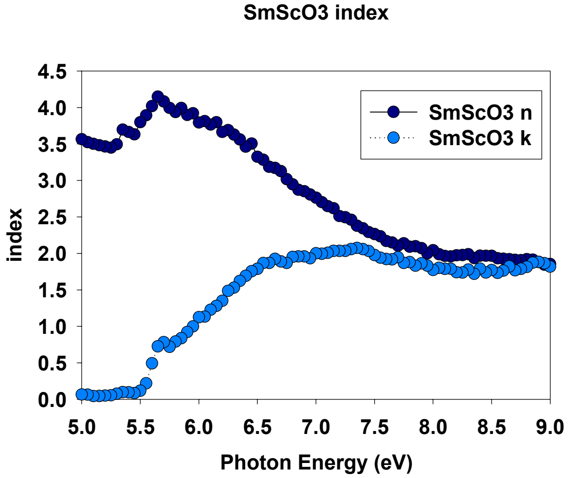

Figure 48. Complex refractive index for $SmScO_3$

$SmScO_3$ data was also taken by Seung-Gu Lim[44]. The sample studied was single crystal $SmScO_3$, and ellipsometric measurements were taken from 5-9 eV. He found that the dielectric function ε_2 did not go to zero as expected. He speculated that this may be due to back scattering (reflection from the back surface, which had not been roughened), therefore the band gap was extrapolated from the higher energy results. The band gap was estimated to be between 5.5 and 6.0 eV. Our results indicate that the $SmScO_3$ film sample has a band gap of approximately 5.55 eV, shown in Figure 49. This value does concur with the bandgap value range predicted but Lim.

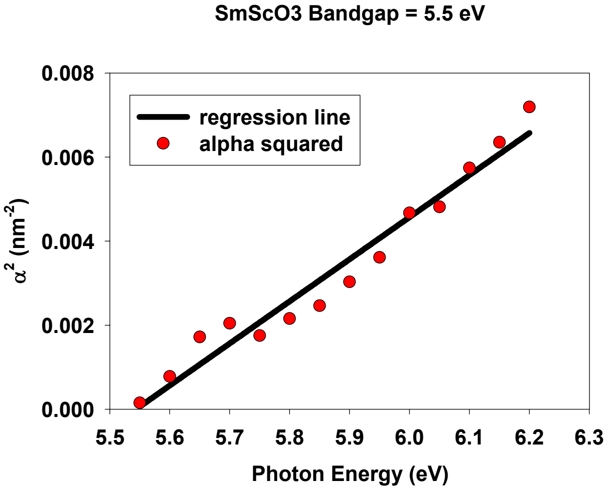

Figure 49. Least squares fit (solid) to data (•) for the SmScO3 film leading to direct bandgap of 5.5 eV.

5.7.2 Transmission Measurements of Single Crystal $SmScO_3$

Transmission measurements were preformed on single crystal $SmScO_3$. The results are seen in Figure 50. The onset of transmission occurs at approximately 5.4 eV. This value is in close agreement with the band gap obtained from the ellipsometric measurements done on the $SmScO_3$ film.

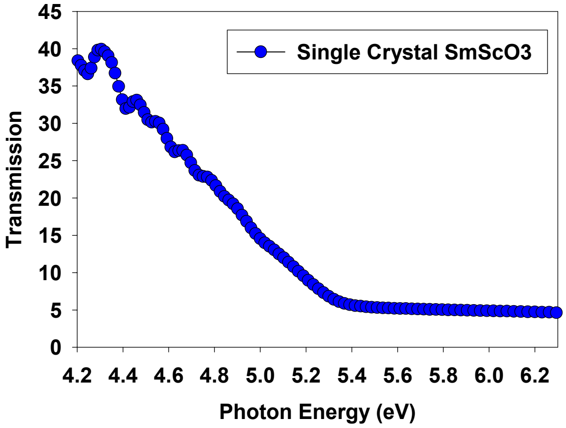

Figure 50. Transmission measurement of Single Crystal SmScO3

5.8 LaMgZrO/$LaAlO_3$ alloy

5.8.1 Results and Discussion for PLD LaMgZrO/$LaAlO_3$ alloy on $LaAlO_3$

A true LaMgZrO/$LaAlO_3$ alloy was deposited on the single crystal $LaAlO_3$ substrate. To deal with the interference fringes the data was broken down into two sections: for energies between 5-6.5 eV the Lorentz Oscillator model was used, and for energies above 6.5 eV the NK model was used. The point-by-point analysis technique was used, assuming the initial dielectric response was identical to the $LaScO_3$ film on $LaAlO_3$ substrate. The analysis showed that the film was 140 nm with a surface roughness layer of 14 nm with a 57 % void fraction. Figure 51 shows the comparison between the measured and calculated data.

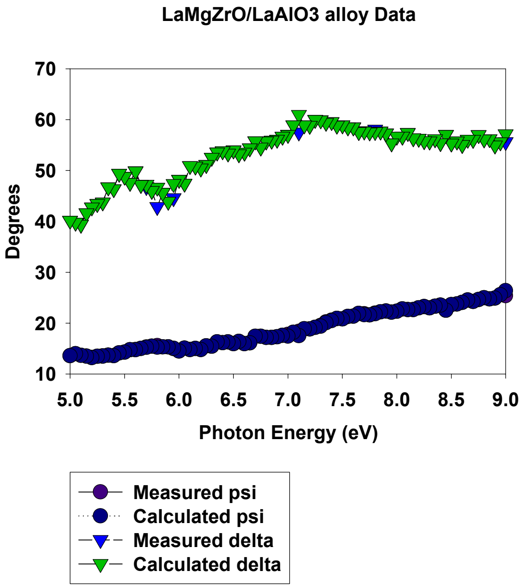

Figure 51. Comparison between calculated and measured data for the LaMgZrO/LaAlO3 alloy film on Single crystal (100) LaAlO3 substrate.

The real (n) and imaginary (k) parts of the complex refraction index are shown in Figure 52. The linear fit to α^2 shows a bandgap of 6.7 eV, this is shown in Figure 53.

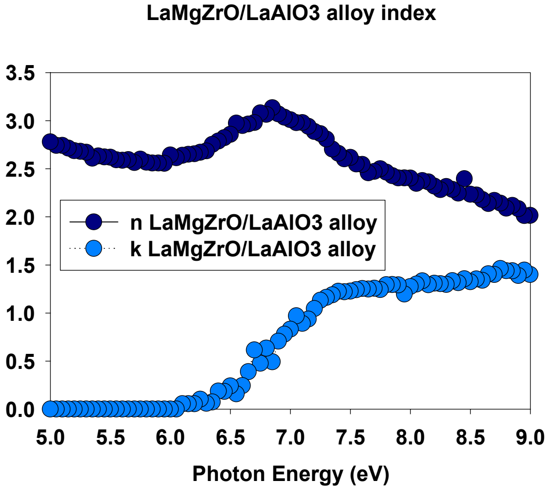

Figure 52. Complex refractive index for LaMgZrO/LaAlO$_3$

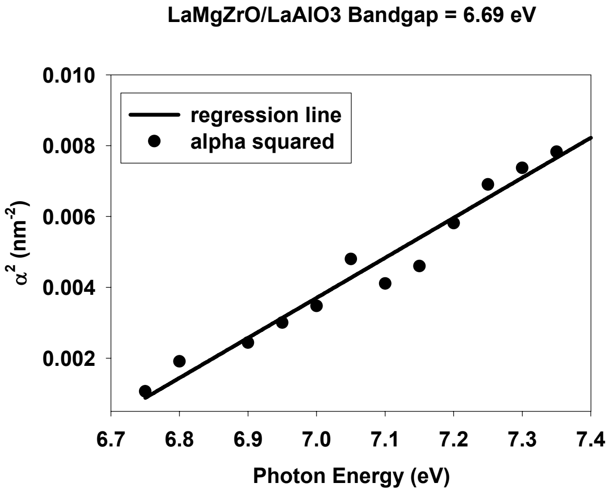

Figure 53. Least squares fit (solid) to data (•) for the LaMgZrO/LaAlO3 film Leading to direct bandgap of 6.7 eV.

The next set of graphs, Figure 54 and 55, compare the index values of the LaMgZrO/$LaAlO_3$ alloy with the $LaAlO_3$ substrate values.

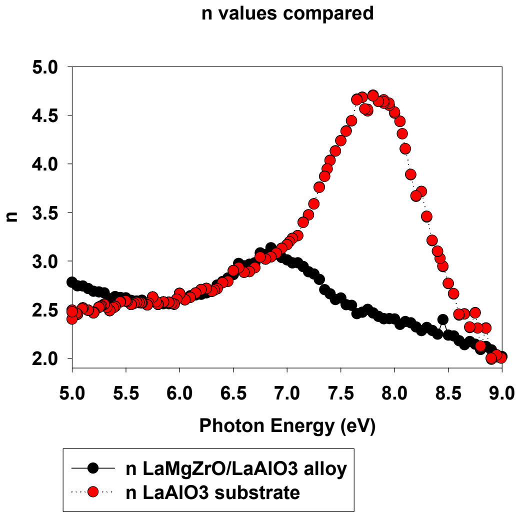

Figure 54. n values compared for LaMgZrO/ $LaAlO_3$ alloy film, and the $LaAlO_3$ single crystal substrate.

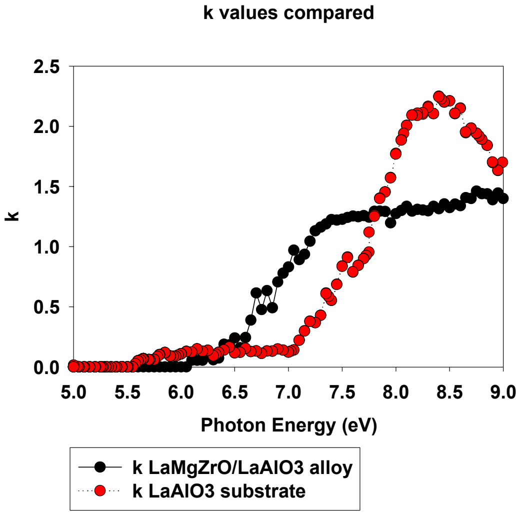

Figure 55. k values compared for LaMgZrO/ $LaAlO_3$ alloy film, and the $LaAlO_3$ single crystal substrate.

5.9 $SrTiO_3/LaAlO_3$ alloy

5.9.1 Results and Discussion for PLD $SrTiO_3/LaAlO_3$ alloy on $LaAlO_3$

The data from the $SrTiO_3/LaAlO_3$ alloy did not show any interference fringes, therefore the data was treated as a standard NK model with the initial analysis assuming the dielectric respond as LaMgScO/$LaAlO_3$ alloy. The point-by-point analysis showed that the film was 153 nm with a surface roughness layer of 12 nm with a 50 % void fraction. Figure 56 shows the comparison between the measured and calculated data. The real (n) and imaginary (k) parts of the complex refraction index are shown in Figure 57.

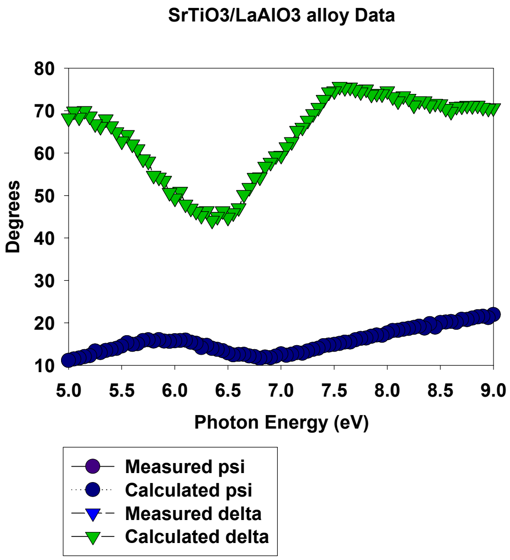

Figure 56. Comparison between calculated and measured data for the SrTiO3/LaAlO3 alloy film on Single crystal (100) LaAlO3 substrate.

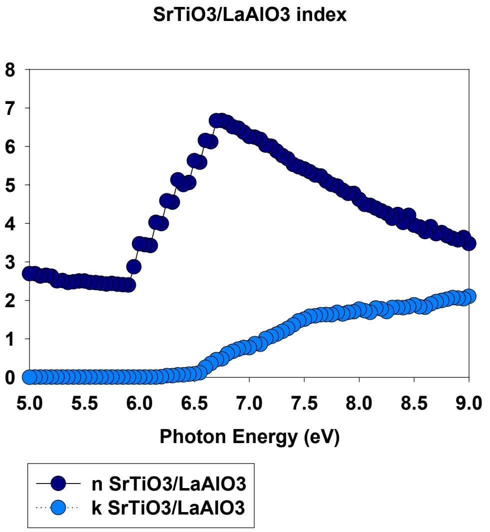

Figure 57. Complex refractive index for $SrTiO_3/LaAlO_3$

The linear fit to α^2 shows a bandgap of 6.5 eV, this is shown in Figure 58.

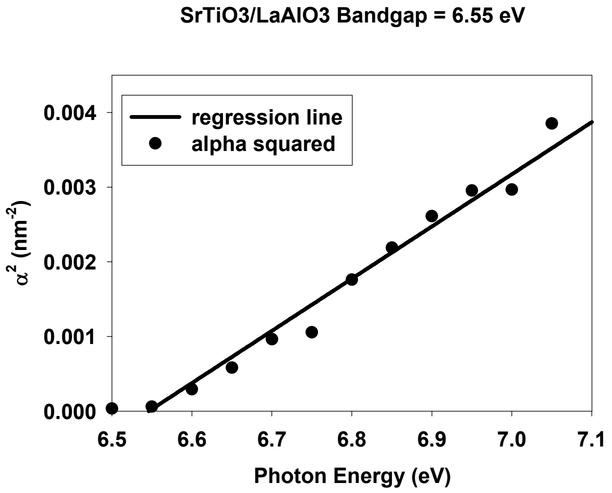

Figure 58. **Least squares fit (solid) to data (•) for the SrTiO3/LaAlO3 film Leading to direct bandgap of 6.5 eV.**

The next set of graphs, Figure 59 and 60, compare the index values of the $SrTiO_3/LaAlO_3$ alloy with the $LaAlO_3$ substrate values.

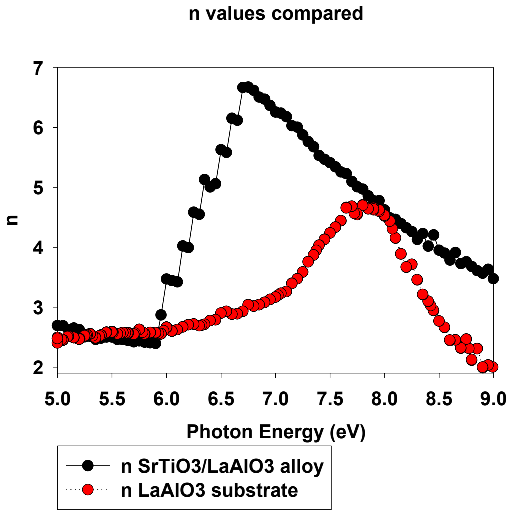

Figure 59. n values compared for $SrTiO_3$/ $LaAlO_3$ alloy film, and the $LaAlO_3$ single crystal substrate.

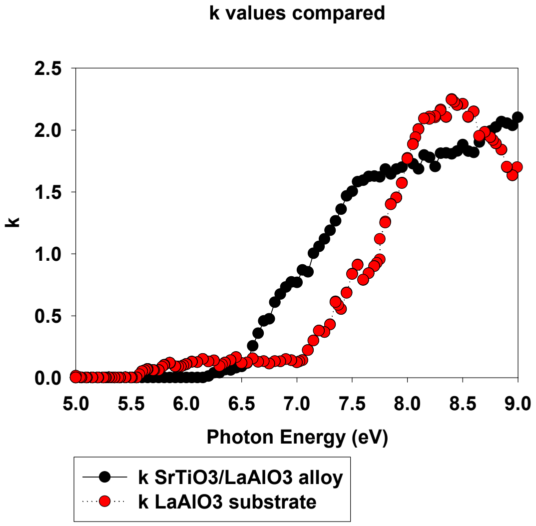

Figure 60. k values compared for $SrTiO_3$/ $LaAlO_3$ alloy film, and the $LaAlO_3$ single crystal substrate.

5.10 $DyScO_3$

5.10.1 Results and Discussion for PLD $DyScO_3$ on $LaAlO_3$

The $DyScO_3$ film on LaAlO3 was found to have a thickness of 199.2 nm with a 15.2 nm surface roughness layer at 37 % Void fraction. The fit, which again had to be divided into sections so that the energy range between 5.0-6.5 eV could be treated as an Oscillator Model, can be seen in Fig(61). The Dielectric response is shown in Fig(62).

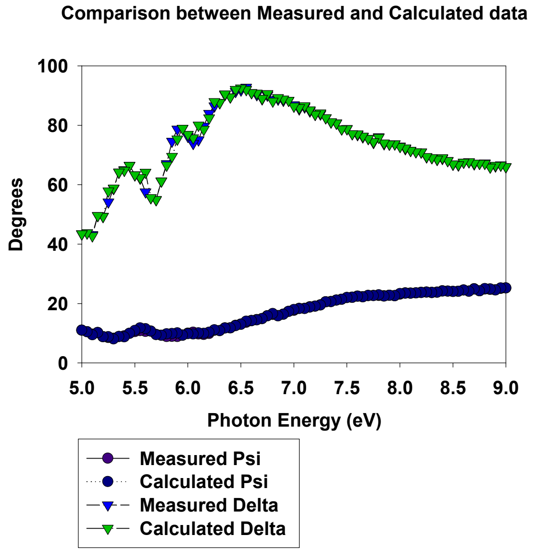

Figure 61. Comparison between calculated and measured data for the DyScO3 film on Single crystal (100) LaAlO3 substrate.

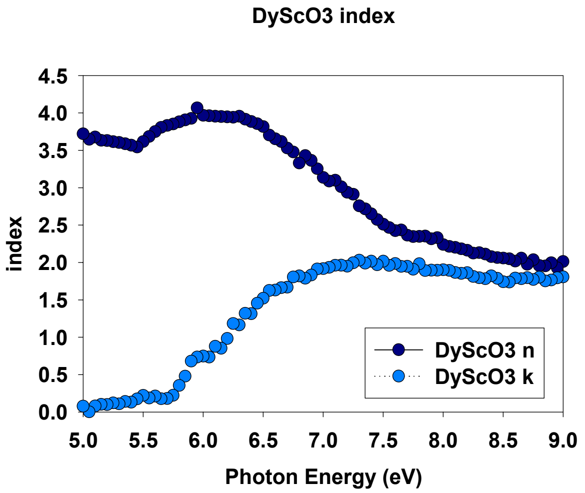

Figure 62. Complex refractive index for DyScO3

We found two linear regions leading to bandgaps of 5.95 eV and 5.73 eV, seen in Figs(63) and (64). Single Crystal DyScO$_3$ was also measured with both Ellipsometry and Transmission, this will be discussed in Anisotropic Single Crystal Section.6.6.1.

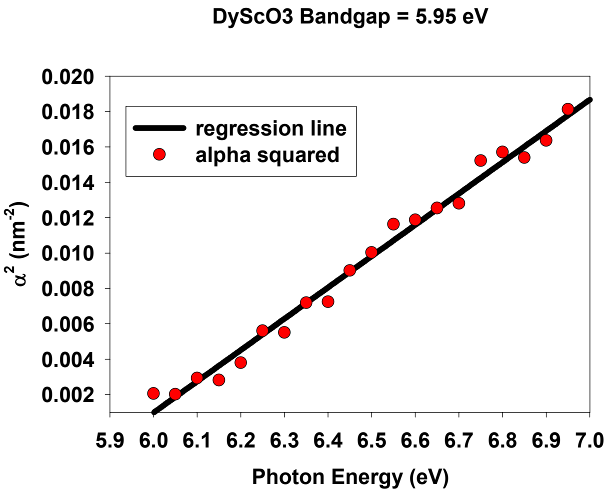

Figure 63. Least squares fit (solid) to data (•) for the DyScO3 film Leading to direct bandgap of 5.95 eV.

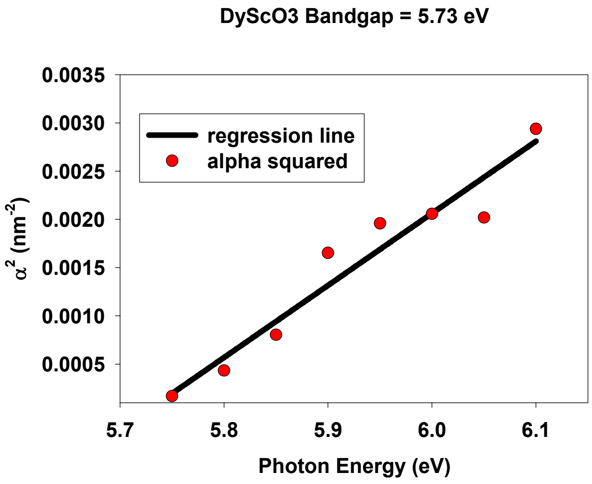

Figure 64. Least squares fit (solid) to data (●) for the DyScO3 film Leading to direct bandgap of 5.73 eV.

5.10.2 Transmission of $DyScO_3$ films and single crystal

Transmission measurements were preformed on an amorphous and epitaxial film of $DyScO_3$. As seen in Fig(65) the amorphous film has an onset of transmission at approximately 5.5 eV, and the epitaxial films shows an onset of transmission close to 6.0 eV. This value is in close agreement with the band gap obtained from the ellipsometric measurements done on the $DyScO_3$ film.

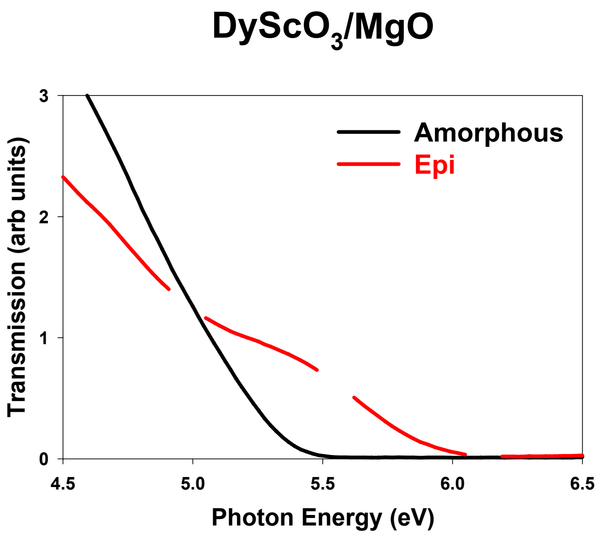

Figure 65. Transmission measurement on Amorphous and Epitaxial films

Single crystal bulk $DyScO_3$ was also measured with transmission. As seen in Fig(66) the onset of transmission for the single crystal sample is approximately 5.3 eV.

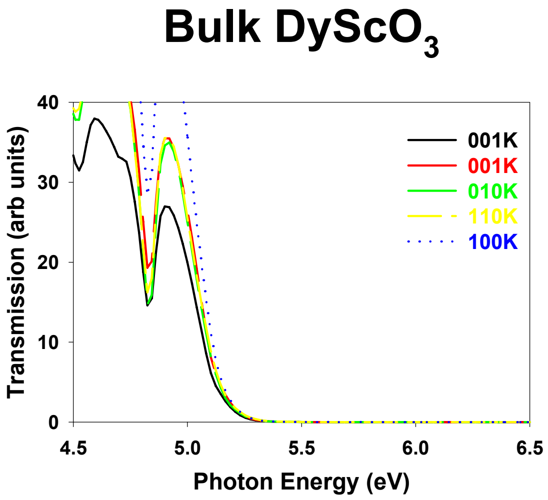

Figure 66. **Transmission measurement on Single Crystal DyScO3**

5.11 $GdScO_3$

5.11.1 Results and Discussion for PLD $GdScO_3$ on $LaAlO_3$

The $GdScO_3$ film on $LaAlO_3$ was found to have a thickness of 692.0 nm with a 13.1 nm surface roughness layer at 29 % Void fraction. The fit, which again had to be divided into sections so that the energy range between 5.0-5.8 eV could be treated as an Oscillator Model, can be seen in Fig(67). The Dielectric response is shown in Fig(68). One linear region leading to a bandgap of 6.12 eV, seen in Fig(69). Single Crystal $GdScO_3$ was also measured with both Ellipsometry and Transmission, this will be discussed in Anisotropic Single Crystal Section.6.6.2 and in section 5.11.2.

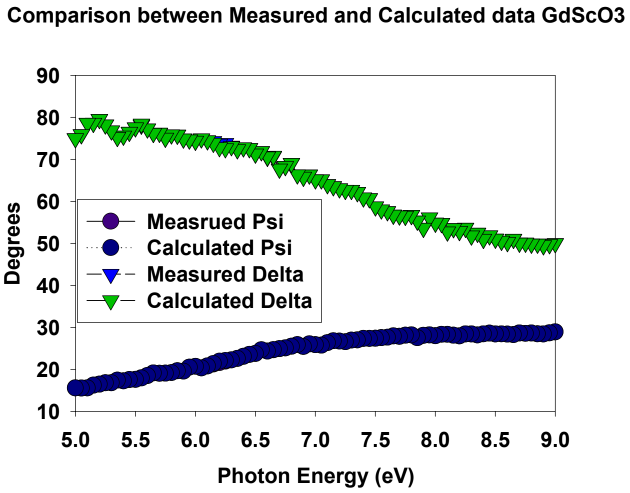

Figure 67. Comparison between calculated and measured data for the GdScO3 film on Single crystal (100) LaAlO3 substrate.

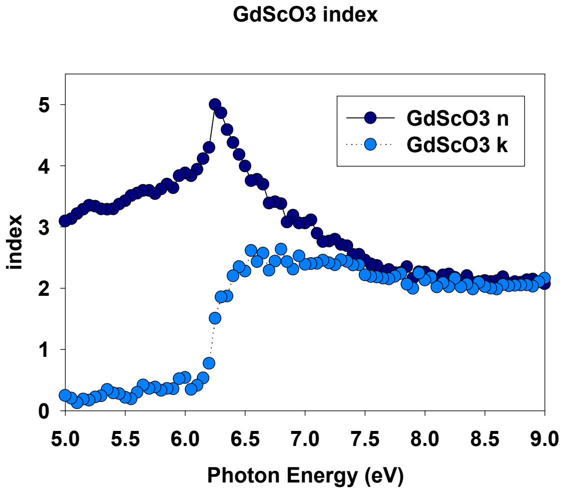

Figure 68. Complex refractive index for GdScO3

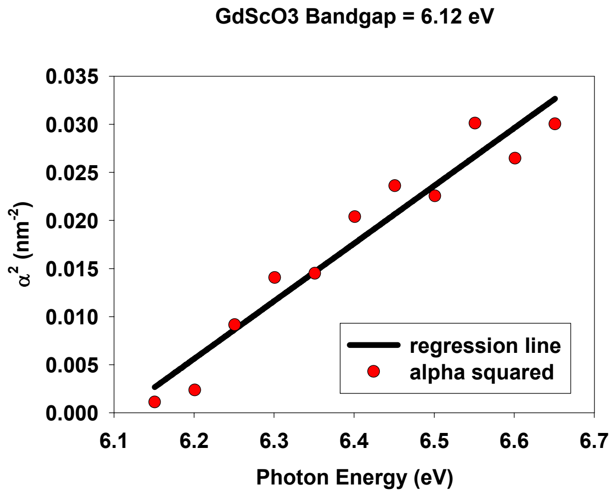

Figure 69. **Least squares fit (solid) to data (●) for the GdScO3 film Leading to direct bandgap of 6.12 eV.**

5.11.2 Transmission of $GdScO_3$ films and single crystal

Transmission measurements were preformed on an amorphous and epitaxial film of $GdScO_3$. As seen in Fig(70) the amorphous film has an onset of transmission at approximately 5.5 eV, and the epitaxial film shows an onset of transmission close to 5.7 eV. As with the $DyScO_3$ films we see a larger bandgap on the epitaxial film. This value is in close agreement with the band gap obtained from the ellipsometric measurements done on the $GdScO_3$ film. Single crystal bulk $GdScO_3$ was also measured with transmission. As seen in Fig(71) the onset of transmission for the single crystal sample is approximately 5.2 eV, which is where transmission exceeds 1% through this 1mm sample, so α may exceed 100 cm^{-1}. There has been some controversy[53] regarding the bandgap of $GdScO_3$, it has been proposed that the bandgap is actually where the transmission increases markedly for photon energies around 3.5 eV, i.e., where α is perhaps 10 cm^{-1} and not accessible to measurement by ellipsometry on thin films. Our measurements cannot resolve this issue. Since the relevant gap is a one-electron transition and involves such low levels of absorption, it must be addressed by such electronic measurements as photoconductivity in bulk material or internal photoemission in a gate dielectric structure.

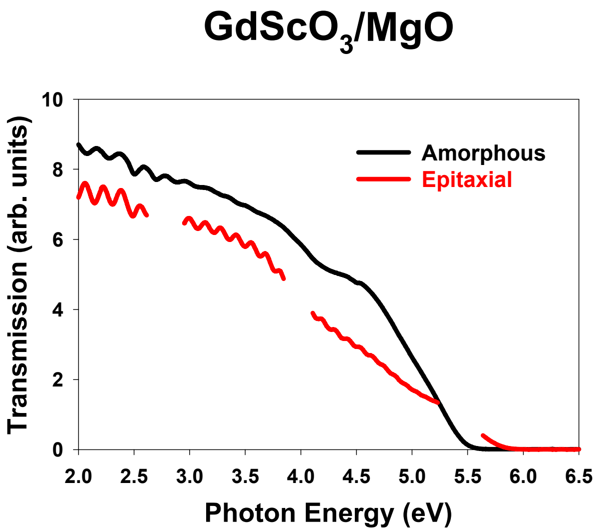

Figure 70. Transmission measurement on Amorphous and Epitaxial films

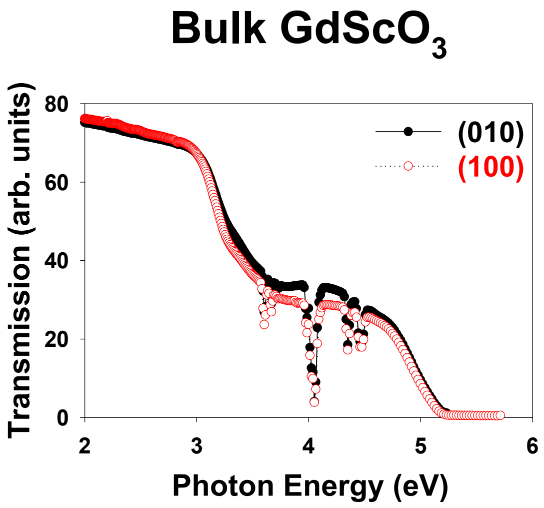

Figure 71. Transmission measurement on Single Crystal GdScO3

Chapter 6

Single Crystal Anisotropic Analysis

6.1 Introduction

Both the single crystal $DyScO_3$ and the single crystal $GdScO_3$ samples required a new approach to determine the optical constants. These crystals are orthorhombic at room temperature; because of this anisotropic structure, the standard isotropic analysis technique is not sufficient. As discussed in Sections 1.2.2 and 1.2.3 these samples generate nondiagonal Jones matrix elements as seen in Eq(8), therefore the Fourier coefficients α and β become more complicated as shown in Eq.(18). This anisotropy was manifest in our experimental results, which clearly depended upon the crystal orientation with respect to the plane of incidence, which should not happen with an isotropic sample. The observed anisotropy was consistent with observed anisotropy in the static dielectric constant. For both $GdScO_3$ and $DyScO_3$ the dielectric constant measured along the [100] and [010] orientation had a value of approximately 20 compared with the value obtain from the [001] orientation of around 30[54]. Therefore, it was necessary to develop a way to determine the optical constant tensor from an anisotropic material.

6.2 Alignment of the samples

The samples were aligned and measured along the axis, in the plane of incidence. The calibration procedure described in section 1.4.1 allowed a way to determine that the axis of the sample was precisely aligned in the plane of incidence. As mentioned in section 6.1 the crystals measured were orthorhombic therefore the three axes a, b, and c are orthogonal to each other but of unequal lengths as seen in Fig(72). If a crystal axis was not aligned with the plane of incident for the calibration, then the electrical signal I'(t) from Eq.(23) would not show maximum modulation with the Fourier coefficients as ($\alpha'^2 + \beta'^2 = 1$).

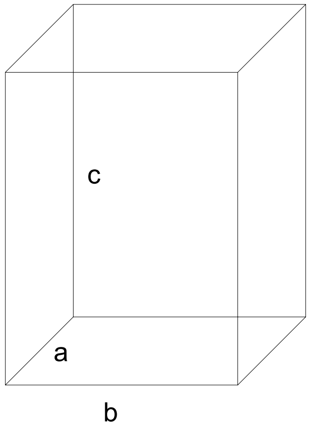

Figure 72 :orthorhombic crystal; orthogonal and a≠b≠c

6.3 Optical Constants of Anisotropic Crystals

The first approach used to determine the optical constants of our anisotropic samples was laid out by R.H.W. Graves[55]. In his paper he presents methods of determining the principal optical constants of biaxial and uniaxial crystals using either ellipsometric or reflectance measurements. For our area of interest, the ellipsometric techniques for a biaxial crystal were of importance.

Following the convention used by Graves, we define the plane of incidence as the *xz* plane and the medium boundary as the *xy* plane. Therefore the *z*-axis is normal to the boundary, as is shown in Fig(73). Given a crystal with three orthogonal principal axes *a*,*b*,*c* we would represent a crystal orientation with the *a* axis lying along the *x* direction, the *b* axis along the *y* direction, and the *c* axis along the *z* direction as *axbycz*.

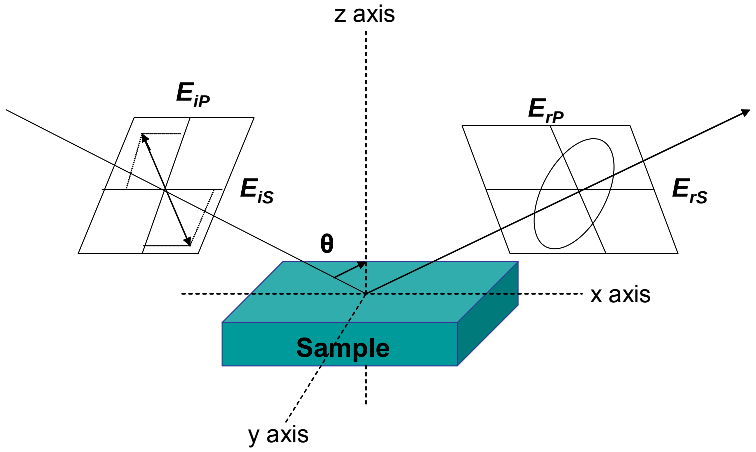

Figure 73 :Graves convention, with the plane of incidence as the *xz* plane and the medium boundary as the *xy* plane, therefore the *z*-axis is normal to the boundary

The complex amplitude reflection coefficients are determined with regards to this coordinate system as:

$$r_{\parallel} = \frac{(\varepsilon_z - \sin^2\theta)^{1/2} - (\varepsilon_x\varepsilon_z)^{1/2}\cos\theta}{(\varepsilon_z - \sin^2\theta)^{1/2} + (\varepsilon_x\varepsilon_z)^{1/2}\cos\theta} \tag{172}$$

$$r\perp = \frac{\cos\theta - (\varepsilon_y - \sin^2\theta)^{1/2}}{\cos\theta + (\varepsilon_y - \sin^2\theta)^{1/2}} \tag{173}$$

with $r_{\parallel}$ and $r\perp$ representing the reflection coefficients parallel and perpendicular to the plane of incidence, and θ representing the angle of incidence. The complex dielectric constant in the *m* direction is defined as $\varepsilon_m = \varepsilon_m' - i\varepsilon_m''$.

As discussed in Section 1.2.1 the ellipsometric angles Ψ and Δ are related to the complex amplitude reflection coefficients as:

$$\rho e^{i\Delta} = \frac{r_p}{r_s} \tag{174}$$

with,

$$\rho = \tan\Psi$$

Expanding this equation with the results found in Eqs. (172) and (173) we find:

$$\rho e^{i\Delta} = \frac{r_p}{r_s} = \frac{[\gamma_z - (\varepsilon_x\, \varepsilon_z)^{1/2}\cos\theta][(\cos\theta + \gamma_y]}{[\gamma_z - (\varepsilon_x\, \varepsilon_z)^{1/2}\cos\theta][(\cos\theta - \gamma_y]}$$

with

$$\gamma_{z,y} = (\varepsilon_{z,y} - \sin^2\theta)^{1/2}$$

and therefore

$$\frac{1 - \rho e^{i\Delta}}{1 + \rho e^{i\Delta}} = \frac{\cos\theta[\gamma_z - \gamma_y (\varepsilon_x\, \varepsilon_z)^{1/2}]}{(\varepsilon_x\, \varepsilon_z)^{1/2}\cos^2\theta - \gamma_y\gamma_z} \tag{175}$$

In the Graves paper Eq.(175) is written incorrectly as $(1+\rho e^{i\Delta})/\ (1-\rho e^{i\Delta})$, however after re-examining the algebra we found that the correct expression in this equation is $(1-\rho e^{i\Delta})/\ (1+\rho e^{i\Delta})$. By solving for $(\varepsilon_x\, \varepsilon_z)^{1/2}$ with $\phi = (1-\rho e^{i\Delta})/\ (1+\rho e^{i\Delta})$ we find:

$$(\varepsilon_x\, \varepsilon_z)^{1/2} = \left(\frac{\cos\theta + \phi\gamma_y}{\phi\cos\theta + \gamma_y}\right)\frac{\gamma_z}{\cos\theta}$$

so that:

$$\varepsilon_x = \left(\frac{\cos\theta + \phi\gamma_y}{\phi\cos\theta + \gamma_y}\right)^2 \frac{(\varepsilon_z - \sin^2\theta)}{\varepsilon_z \cos^2\theta}$$

$$= f_1(\varepsilon_y) \cdot f_2(\varepsilon_z) \tag{176}$$

With $f_1(\varepsilon_y)$ as a function of ε_y and the experimentally determined parameters and $f_2(\varepsilon_z)$ as a function of ε_z and θ.

To proceed with the Graves approach, we measured ρ and Δ for several crystal orientations: *axbycz, aybxcz,* and *aybzcx*, and formed three versions of Eq.(176):

$$\varepsilon_a = f_1(\varepsilon_b) \cdot f_2(\varepsilon_c) \tag{177a}$$

$$\varepsilon_b = f_1(\varepsilon_a) \cdot f_2(\varepsilon_c) \tag{177b}$$

$$\varepsilon_c = f_1(\varepsilon_a) \cdot f_2(\varepsilon_b) \tag{177c}$$

A simple iterative technique was used to solve for ε_a , ε_b , and ε_c.

We developed a Matlab program to utilize this technique, however the results were not correct. We concluded that this technique was not sufficient. This approach does not take into account the possibility of an overlayer, and our samples have a large overlayer. Therefore a modification to this technique that includes an overlayer was necessary.

6.4 Optical Constants of Anisotropic Crystals with Overlayer

To update the program to include an overlayer, we implemented a three-phase system including a substrate, ambient, and a single overlayer. As described by D.E. Aspnes[56], in this model the corresponding dielectric functions are given by ε_s, ε_{am}, ε_o, and the complex reflectances are written as

$$r'_p = \frac{Zr_{p,os} + r_{p,amo}}{Zr_{p,amo}r_{p,os} + 1} \tag{178a}$$

$$r'_s = \frac{Zr_{s,os} + r_{s,amo}}{Zr_{s,amo}r_{s,os} + 1} \tag{178b}$$

with

$$Z = \exp(4\pi i n_{O\perp} d/\lambda) \tag{178c}$$

the overlayer thickness d was determined by analyzing the measured data with our standard analyzing tool Filmwizard, by holding the index values constant and letting the overlayer thickness and the overlayer material properties vary. The term $n_{O\perp}$ is described by

$$n_{O\perp} = (\varepsilon_o - \varepsilon_{am}\sin^2\varphi)^{1/2} \tag{178d}$$

The two-phase reflectances $r_{p,ij}$ and $r_{s,ij}$ are described by

$$r_{p,ij} = \frac{\varepsilon_j n_{i\perp} + \varepsilon_i n_{j\perp}}{\varepsilon_j n_{i\perp} - \varepsilon_i n_{j\perp}} \tag{179a}$$

$$r_{s,ij} = \frac{n_{i\perp} - n_{j\perp}}{n_{i\perp} + n_{j\perp}} \tag{179b}$$

with

$$n_{i\perp} = n_i \cos\varphi \tag{179c}$$

$$n_{j\perp} = (\varepsilon_j - \varepsilon_i \sin^2\varphi)^{1/2} \tag{179d}$$

where ε_j , and ε_i are the respective dielectric functions. Note that Eqs.(179c) and (179d) have similar form to terms in Eqs.(172) and (173) with the assumption that $n_{am} = 1$.

To incorporate the Graves techniques into the Aspnes model we needed to define r'_p and r'_s from Eq.(178) for the three orientations of the anisotropic crystal. The first step was to determine $r_{p,amo}$ and $r_{s,amo}$, the two-phase reflectances for the ambient-overlayer system. To find these values we use Eqs.(179a) and (179b), with i = am, and j = o, therefore

$$r_{p,amo} = \frac{\varepsilon_o n_{am\perp} + \varepsilon_{am} n_{o\perp}}{\varepsilon_o n_{am\perp} - \varepsilon_{am} n_{o\perp}} \tag{180a}$$

$$r_{s,amo} = \frac{n_{am\perp} - n_{o\perp}}{n_{am\perp} + n_{o\perp}} \tag{180b}$$

with

$$n_{am\perp} = n_{am} \cos\theta \tag{181a}$$

$$n_{o\perp} = (\varepsilon_o - \varepsilon_{am}\sin^2\theta)^{1/2} \tag{181b}$$

Where θ is the angle of incidence.

The equations for the two-phase reflectances for the overlayer-substrate system, $r_{p,os}$ and $r_{s,os}$, also need to be determined. From Eqs.(179a) and (179b) we find

$$r_{p,os} = \frac{\varepsilon_o n_{am\perp} + \varepsilon_{am} n_{o\perp}}{\varepsilon_o n_{am\perp} - \varepsilon_{am} n_{o\perp}} \tag{182a}$$

$$r_{s,os} = \frac{n_{o\perp} - n_{s\perp}}{n_{o\perp} + n_{s\perp}} \tag{182b}$$

To determine $r_{p,os}$ and $r_{s,os}$ for the three crystalline orientation, we must incorporate Eqs.(172) and (173) into Eqs.(182a) and (182b). Now the two-phase reflectances for the overlayer-substrate system become

$$r_{p,os} = \frac{\varepsilon_o (\varepsilon_z - \sin^2\varphi)^{1/2} - (\varepsilon_x\varepsilon_z)^{1/2}(\varepsilon_o - \sin^2\theta)^{1/2}}{\varepsilon_o (\varepsilon_z - \sin^2\varphi)^{1/2} + (\varepsilon_x\varepsilon_z)^{1/2}(\varepsilon_o - \sin^2\theta)^{1/2}} \tag{183a}$$

$$r_{s,os} = \frac{(\varepsilon_o - \sin^2\theta)^{1/2} - (\varepsilon_y - \sin^2\varphi)^{1/2}}{(\varepsilon_o - \sin^2\theta)^{1/2} + (\varepsilon_y - \sin^2\varphi)^{1/2}} \tag{183b}$$

Where φ is the complex angle of incidence between the overlayer and the substrate. With these terms defined we are now able to determine r'_p and r'_s from Eqs.(178a) and (178b) for the ambient-overlayer-substrate system. Following the Graves approach we write Eq.(174) using r'_p and r'_s in three versions, with the first version letting the dielectric function for the "a" orientation vary to agree with the experimentally determined ρ function. The next two functions utilize the same process for the "b" and "c" orientations using the new values for the dielectric functions determined in the minimization processes. To initiate the process we give the program starting values for the dielectric functions of the three orientations, then iterated several times until it converges and a solution is found. The matlab code for this program can be found in Appendix 1.

6.5 Testing the anisotropic-overlayer program

To test the anisotropic ambient-overlayer-substrate process, the program was used to determine the dielectric constants of a Si substrate with a SiO_2 overlayer. Since the dielectric constants of this system are well known it would be easy to compare the results we obtain from the program and the true values of the dielectric response. For starting values the dielectric function of $LaAlO_3$ was used as seen in Fig(74). Running the Si-SiO2 system through the program we find that the Si dielectric results match up to the actual values for Si as seen in Figs(75) and (76).

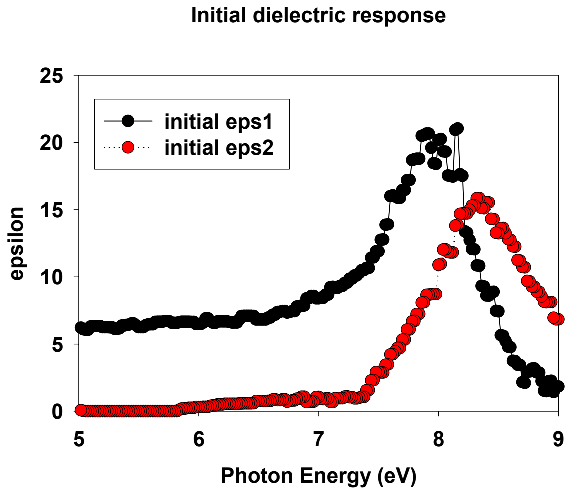

Figure 74. Initial dielectric response used in the Si/SiO_2 test run.

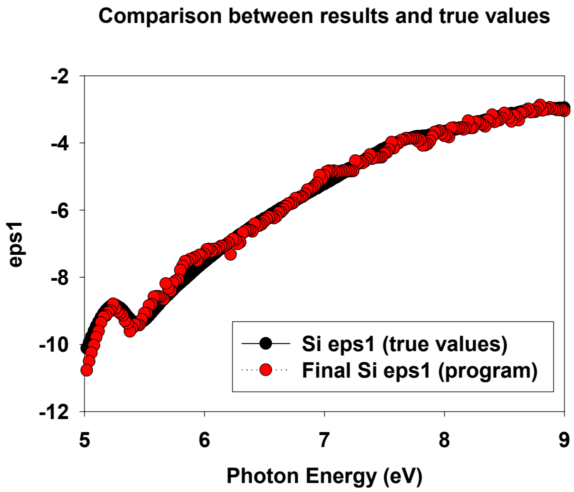

Figure 75. **Comparison between results obtain by anisotropic overlayer program and the true dielectric response of Si**

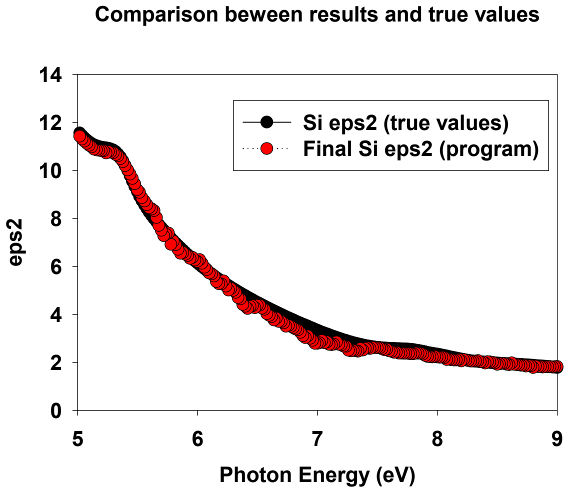

Figure 76. **Comparison between results obtain by anisotropic overlayer program and the true dielectric response of Si**

6.5 Other approaches to anisotropic analysis

It is important to mention another approach to anisotropic analysis that was developed by Mathias Schubert and John A. Woollam[57], and how it compares to our approach. In this alternative approach the Fourier Coefficients described in Eq.(18) are determined at one set of wavelength, sample orientation, and incidence angle for many polarizer settings. The unknown normalized reflection matrix elements defined in Eq.(8) are found by minimizing the mean-square error function and using Eq.(18) and the experimentally determined standard deviations $\delta\alpha$ and $\delta\beta$

$$\mathrm{MSE} = \frac{1}{N}\sum_{i=1}^{N}\left\{\left(\frac{\alpha_i^{m} - \alpha_i^{\mathrm{calc}}(R_{pp}, R_{ps}, R_{sp}{:}P)}{\delta\alpha_i^{m}}\right)^2 + \left(\frac{\beta_i^{m} - \beta_i^{\mathrm{calc}}(R_{pp}, R_{ps}, R_{sp}{:}P)}{\delta\beta_i^{m}}\right)^2\right\}$$

from the fit combining the R_{pp}, R_{ps}, R_{sp} data acquired at different sample orientations and incidence angles, the optical constants could be found. Due to the use of multiple sample orientations, the number of parameters to be determined at each wavelength is much less that the number of data points acquired at each wavelength.

Both the Schubert/Woollam approach and our approach measure the sample at various sample orientations, and both use a minimization process to determine the unknown parameters. However, as with the Graves approach the Schubert/Woollam approach does not account for a large overlayer.

6.6 Results

The dielectric response of an anisotropic crystal was explored using the Graves/Overlayer approach. We had two samples of single crystal GdScO3, with surface normal of (001) and (010), grown by Professor Darrell Schlom and colleagues at Penn State University.

6.6.1 GdScO3 Results

To determine the crystalline orientation, the GdScO3 samples were sent to Penn State and measured by X-Ray analysis. The resulting orientations are shown in Fig.(75). The surface normal orientations are shown in parenthesis ( ) and the crystalline orientations are shown in brackets [ ].

In the Graves/Overlayer program the [001] orientation was used for the “a” orientation, and the [100] and [010] orientation were used for the “b” and “c” orientations. Therefore with regards to Fig.(77) the axbycz orientation would be associated with the (010) sample in the vertical direction, the aybxcz would be the (010) sample in the horizontal direction, and the aybzcx would be the (100) sample in the vertical direction.

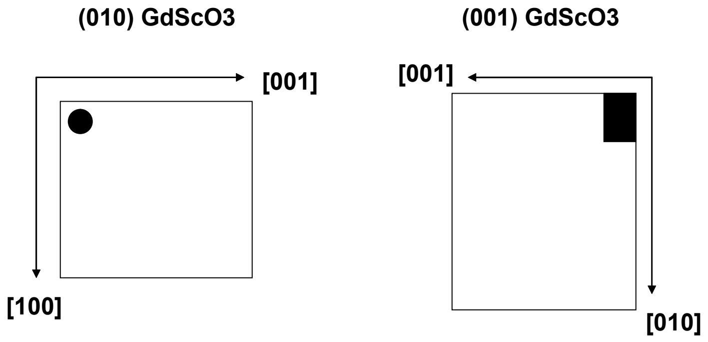

Figure 77. **GdScO3 crystal orientations**

The data measured from the crystals was originally put through our normal analysis technique, which did not compensate for the anisotropic behavior. These results can be seen in Figs.(78) and (79).

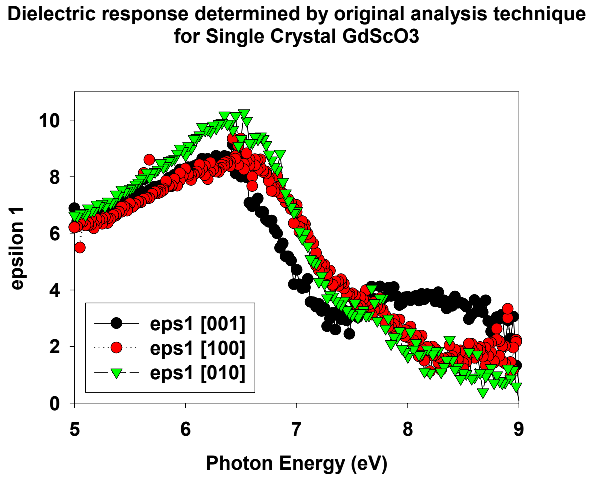

Figure 78. epsilon1 results obtained by original analysis technique

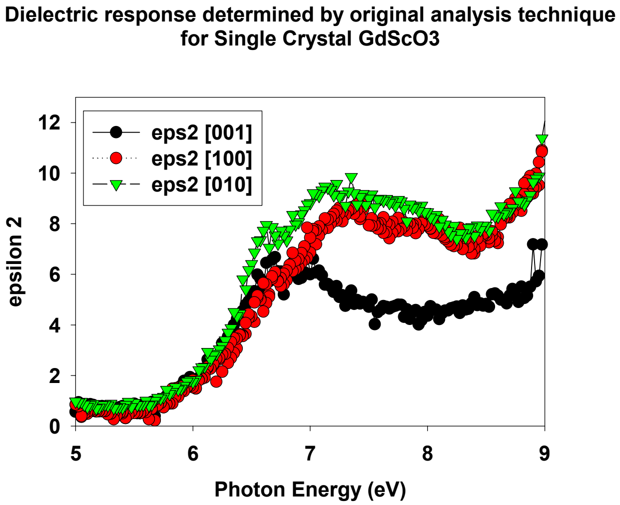

Figure 79. epsilon2 results obtained by original analysis technique

With our Graves/Overlayer approach we can account for the anisotropic structure and the results are shown in Figs.(80) and (81).

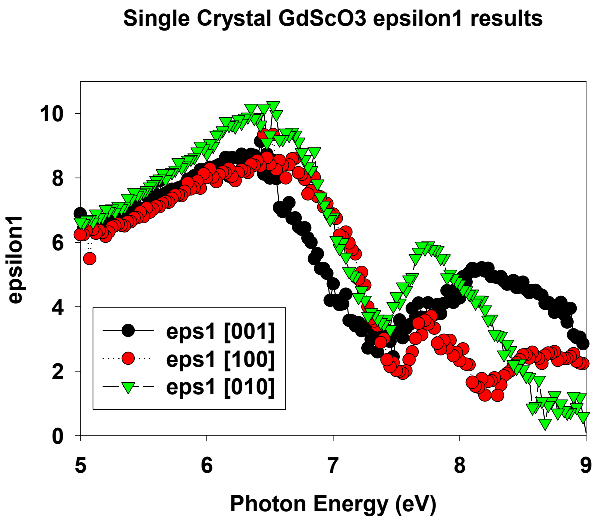

Figure 80. epsilon1 results obtained by anisotropic analysis technique

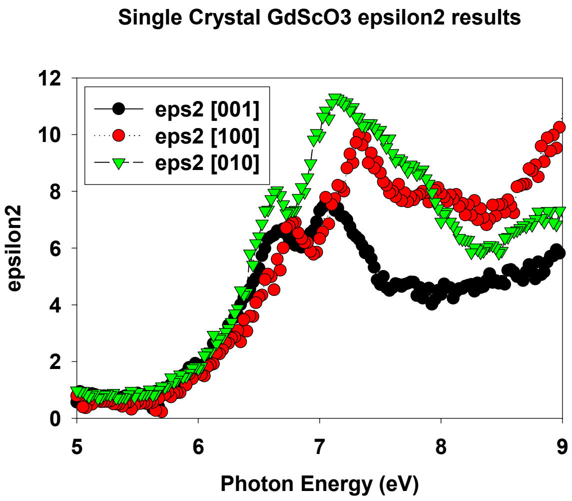

Figure 81. epsilon2 results obtained by anisotropic analysis technique

By comparing Figs.(78) to (80) and Figs.(79) to (81) we can see the effect the anisotropic analysis has on the final results. Without the Graves/Overlayer analysis technique the dielectric response would not be correct.

Chapter 7

Conclusion

The optical properties of several high-K samples of bulk crystalline, epitaxial films, and amorphous films, were determined using a custom fabricated far UV spectroscopic ellipsometer. Some also were investigating by visible-near UV optical transmission measurements. These materials are possible replacements for SiO_2 as gate dielectrics in aggressively scaled silicon devices. The spectroscopic data and results provide information that is needed to select viable alternative dielectric candidate materials with adequate band gaps, and additionally to provide an optical metrology for gate dielectric films on silicon substrates.

The proposed Graves/Overlayer analysis technique provides a way to determine the optical response of anisotropic crystals that have an overlayer of surface damage. This technique proves to be more accurate than the conventional analysis techniques that does not compensate for anisotropic structure. Therefore a more precise dielectric response can be determined. To continue this work, additional measurements need to be taken on single crystal $DyScO_3$ to obtain all required orientations for the program.

Bibliography

[1] Drude, P. Bestimmung optischer Konstanten der Metalle. *Ann. Physik Chemie* 32 (1887), 584-595.

[2] Drude, P. Physik des Äthers auf elektromagnetischer Grundlage. *Ann. Physik Chemie* 34 (1888), 489-501.

[3] Drude, P. Optische Eigenschaften und Elektronentheorie. *Ann. Physik Chemie* 38 (1890) 481-491.

[4] Palik, E.D. *Handbook of Optical Constants.* Academic Press, 1985.

[5] Palik, E.D. *Handbook of Optical Constants II.* Academic Press, 1991.

[6] Palik, E.D. *Handbook of Optical Constants III.* Academic Press, 1997.

[7] Rothen, A., Passaglia, E., Stromberg R.R., Kruger J. Ellipsometry in the Measurement of Surfaces and Thin Films. *Natl. Bur. Std. Misc. Publ*. 256 (1964), 7-15.

[8] Hall, A.C. A century of ellipsometry, *Surf. Sci.* 16 (1969), 1-13.

[9] Vedam, K. Spectroscopic ellipsometry: a historical overview, *Thin Solid Films* 313-314 (1998), 1-9.

[10] Tronstad, L. The investigation of thin surface films on metals by mean of reflected polarized light. *Trans. Faraday Soc.* 29 (1933), 502-514.

[11] Kent C.V., J. Lawson. Photometric instrumentation, *J. Opt. Soc. Am.* 27 (1937), 117-123.

[12] Rothen A., The Ellipsometer, an Apparatus to Measure Thicknesses of Thin Surface Films. *Rev. Sci. Instrum.* 16 (1945), 26-30.

[13] Faucher J. A., G.M. McManus, H.J. Turnit. Investigation of thin surface films by Ellipsometry. *J. Opt. Soc. Am.* 48 (1958) 51-58.

[14] Passaglia E., R.R. Stromberg, J. Kruger (Eds.), *Ellipsometry in the Measurement of Surfaces and Thin Films*. Natl. Bur. Std. Misc. Publ, (1964).

[15] Hauge P.S., F.H. Dill A rotating-compensator fourier ellipsometer. *Opt. Commun*. 14 (1975) 431-437.

[16] Opsal J., J. Fanton, J. Chen, J. Leng, L Wei, C. Uhrich, M. Senko, C. Zaiser, D.E.

Aspnes. Broadband spectral operation of a rotating-compensator ellipsometer. *Thin Solid Films* 313-314 (1998) 58-61.

[17] Thompson R.C., J.R. Bottinger, E.S. Fry. Measurement of polarized light interactions via the Mueller matrix. *Appl. Opt.* 19 (1980) 1323-1331.

[18] Drevillon B., Control and monitoring of optical thin films deposition in a Matrix Bistributed Electron Cyclotron Resonance reactor. *Prog. Cryst. Growth* 27 (1993) 1-6.

[19] Jellison Jr G.E., E.A. Modine. Two-modulator generalized ellipsometry: experiment and calibration. *Appl. Opt.* 36 (1997) 8184-8189.

[20] Benferhat R.,Ellipsometry study of poly thin films. *Vide* 47 (1991) 264-268.

[21] Hauge P.S., F.H. Dill, Design and Operation of ETA, an Automated Ellipsometer. *IBM L. Res. Dev.* 17 (1973) 472-478.

[22] Aspnes D.E. Fourier transform detection systerm for rotating-analyzer ellipsometers. *Opt. Commun.* 8 (1973) 222-225.

[23] Wöhler H., M. Fritsch, G. Haas, D.A. Mlynski. Characteristic matrix method for stratified anisotropic media: optical properties of special configurations. *J. Opt. Soc. Am. A* 8, (1991) 536-540.

[24] Seya M., F. Masuda. Extreme Ultraviolet Spectroscopic Optics. *Sci. Light* 12, (1963) 9-12.

[25] Samson J.A.R. *Techniqiues of Vacuum Ultraviolet Spectroscopy* Wiley, New York, (1967) Chap.7.

[26] Ammonn E.O., G. A. Massey. High precision scanning ellipsometer. *J. Opt, Soc Am.* 58, (1968) 1427-1431.

[27] Aspnes D.E. Quantitative ellipsometric microscopy at the galss-water interface. *J. Opt. Soc. Am.* 64, (1974) 639-643.

[28] Nayak S. Presented at Rensselaer Polytechnic Institute, NY, 2001 (graduate course).

[29] J.D. Jackson, *Classical Electrodynamics Third Edition*, John Wiley and Sons, New York, (1998) Ch. 7.

[30] Yu P.Y., M. Cardona, *Fundamentals of Semiconductors: Physics and Materials Properties,* Springer, Berlin, (1996) 121-149.

[31] Cohen M.L., J.R. Chelikowsky, *Electronic Structure and Optical Properties of Semiconductors,* Springer-Verlag, New York, (1988) 201-234.

[32] N.W. Ashcroft and N.D. Mermin, *Solid State Physics,* Saunders College Publishing, New York, (1976) 189-220.

[33] Cohen M.L., J.R. Chelikowsky, *Electronic Structure and Optical Properties of Semiconductors,* Springer-Verlag, New York, (1988) 91-158.

[34] Rohlfing M., S.G. Louie, Electron-Hole Excitation in Semiconductors and Insulators. *Phys. Rev. Lett.* 81, (1998) 2312-2315.

[35] Albrecht S., L. Reining, R. Del Sole, and G. Onida. *Ab Initio* Calculation of Excitonic Effects in the Opitcal Spectra of Semiconducotrs. *Phys. Rev. Lett.* 80**,** (1998) 4510-4513.

[36] Yan M., B. Harnich, J.T. Robinson, Z. Pei, O. Ramström, Phase Properties of Carbon-Supported Gold-Platinum Nanoparticles with Different Bimetallic Compositions. *Chem, Mater.* 12 (2005) 3086-3091.

[37] Pierce D.T., and W. E. Spicer. Electronic Sturcture of Amorphous Si from Photoemission and Optical Studies. *Phys. Rev. B* 5, (1972) 3017-3029.

[38] Mott N.F. and E. A. Daves, *Electronic Processes in Non-Crystalline Materials* Clarendon, Oxford, (1979) 198-242.

[39] Davis E.A., and N.F. Mott, The universal dielectric response. *Phil Mag.* 22, (1970) 903-910.

[40] Tauc J., *Optical Properties of Solids,* edited by F. Abelès. North-Holland, Amsterdam, (1972), 277-331.

[41] Tauc J., R. Grigorovici, and A. Vancu. Optical dispersion relations for amorphous. *Phys. Status Solidi* 15, (1966) 627-631.

[42] Haeni J.H., J. Lettiere, S. Trolier-McKinstry, D.G. Schlom, S-G. Lim, T.N. Jackson, M.M. Rosario, J.L. Freeouf, R. Uecker, P. Reiche, A. Ven Graitis, and C.D. Brandle, Dielectric functions and optical bandgap of high-K dielectrics for metal-oxide-semiconductor field-effect transistors. *J. Appl. Phys* 91, (2002) 4500-4503.

[43] Edge L.F., D. G. Schlom, S. A. Chambers, E. Cicerrella, J. L. Freeouf, B. Holländer, and J. Schubert. Measurement of the band offsets between amorphous LaAlO3 and silicon. *Appl. Phys. Lett.* 84, (2004) 726-728.

[44] Lim S.J., S. Kriventsov, T.N. Jackson, J.H. Haeni, D.G. Schlom, A.M.

Balbashov, R. Uecker, P. Reiche, J.L. Freeouf, and G. Lucovsky, Dielectric functions and optical bandgaps of high-K dielectrics for metal-oxide-semiconductor field effect transistors by far ultraviolet spectroscopic ellipsometry. *J. Appl. Phys.* 91, (2002) 4500-4505.

[45] Aspnes D.E., A. A. Studna, and E. Kinsbron, Dielectric properties of heavily doped crystalline and amorphous silicon from 1.5-6.0 eV. *Phys. Rev. B* 29**,** (1984) 768-779.

[46] Rossow U. and W. Richter, in *Optical Characterization of Epitaxial Semiconductor Layers,* edited by G.Bauer and,W. Richter. Springer-Verlag Berlin Heidelberg (1996) 96-108.

[47] Schubert J., M. Siegert, M. Fardmanesh, W. Zander, M. Prömpers, Ch. Buchal, Judit Lisoni, and C. H. Lei, Superconducting and electro-optical thin films prepared by pulsed laser deposition technique. *Appl. Surf. Sci.* 168, (2000) 208-214.

[48] Lu X., Z. Liu, Y. Wang, Y. Yang, X. Wang, H. Zhou, B. Nguyen, Structure and dielectric properties of amorphous $LaAlO_3$ and $LaAlO_xN_y$ films as alternative gate dielectric materials. *J. Appl. Phys.* 94, (2003) 1229-1234.

[49] Munoz M., K. Wei, F.H. Pollak, J.L. Freeouf, C.A. Wang, and G.W. Charache. Opitcal constants of $Ga_{1-x}In_xAs_ySb_{1-y}$ lattice matched to GaSb(001):Experiment and modeling. *J. Appl. Phys.* 87, (2000) 1780-1787.

[50] Aspnes D.E., S. M. Kelso, R. A. Logan, and R. Bhat. Optical properties of $Al_xGa_{1-x}As$. *J. Appl. Phys.* 60, (1986) 754-767.

[51] Aspnes D.E., and A. A. Studna. Dielectric functions and optical parameters of Si, Ge, GaP, GaAs, GaSb, InP, InAs, and InSb from 1.5 to 6.0 eV. *Phys. Rev.* B 27**,** (1983) 985-1009.

[52] Kwok C.K., and C. R. Aita. Indirect band gap in α-ZrO_2. *J. Vac. Sci. Technol. A.* 8**,** (1990) 3345-3346.

[53] Lucovsky G., C.C. Fulton, Y.Zhang Y. Zou, J. Luning, L.F. Edge, J.L. Whitten, R.J. Nemanich, H. Ade, D.G. Schlom, V.V. Afanase'v, A. Stemsmans, S. Zollner, D. Triyoso, and B.R. Rogers. Conduction band-edge States associated with the removal of d-state degeneracies by the Jahn-Teller effect. *IEEE Transactions on Device and Materials Reliability*, **5**, No.1, March (2005) 65-83.

[54] Haeni J.H., J. Lettieri, S. Trolier-McKinstry, and D. G. Schlom, S-G. Lim, T. N. Jackson, M. M. Rosario, E. Ciccerrella, J. L. Freeouf, R. Uecker and P Reiche. Growth and Properties of Epitaxial Rare-Earth Scandate Thin Films. to be published.

[55] Graves R.H.W., Determination of Opitical Constants of Anisotropic Crystals. *J. Opt. Soc. Am.* 59, (1969) 1225-1231.

[56] Aspnes D.E., *Spectroscopic Ellipsometry of Solids,* Academic Press (1991) 809-845.

[57] Schubert M., B. Rheinländer, J.A. Woollam, B. Johs, and C.M. Herzinger. Extension of rotating-analyzer ellipsometry to generalized ellipsometry: determination of the dielectric function tensor from uniaxial TiO2. *J. Opt. Soc Am. A* 13, (1996) 875-879.

Appendix 1

```
%Find rp,ao and rs,ao
%First import excel file with: col(1) = energy, col(2) = esp1, col(3) =
%esp2, these were determined from overlayer information (Filmwizard)
[a,descr] = xlsfinfo('File name')

a = xlsread('File name')

%Now define the output matrix

Final_Ref = ones(161,7)

%define theta, angle of incident

Theta = 70.00*3.14159/180

%Now begin iterations through all energies

for wl = 1:161

eps1 = a(wl, 2)
eps2 = a(wl, 3)

%Now let's calculate rp,ao and rs,ao
%assume angle of incidence is 70 degrees

Epso = complex(eps1,eps2)

rp = ((Epso*cos(Theta)) - (Epso-(sin(Theta))^2)^.5)/((Epso*cos(Theta)) + (Epso -
(sin(Theta))^2)^.5)
rs = (cos(Theta) - (Epso - (sin(Theta))^2)^.5)/(cos(Theta) + (Epso - (sin(Theta))^2)^.5)

Final_Ref(wl,1) = a(wl,1)
Final_Ref(wl,2) = real(rp)
Final_Ref(wl,3) = imag(rp)
Final_Ref(wl,4) = real(rs)
Final_Ref(wl,5) = imag(rs)
Final_Ref(wl,6) = rp
Final_Ref(wl,7) = rs

end
```

```
function b = overlayerall5_var(v,wl,a)
x1 = v(1);
x2 = v(2);

Theta = 70*3.14159/180;
d = 12.71;

%iterate for all energies
Initial = ones(16,6)

%for wl = 1:161

eps1b = a(wl,13);
eps2b = a(wl,14);

eps1c = a(wl,15);
eps2c = a(wl,16);

%Define overlayer complex dielectric function

epsO1 = a(wl, 2);
epsO2 = a(wl, 3);

EpsO = complex(epsO1,epsO2);

Initial(wl,1) = a(wl,1);
Initial(wl,2) = EpsO;

%Define Ambient/Overlayer Reflection Coefficents

Rpao1 = a(wl,4);
Rpao2 = a(wl,5);
Rsao1 = a(wl,6);
Rsao2 = a(wl,7);

Rpao = complex(Rpao1,Rpao2);
Rsao = complex(Rsao1,Rsao2);

Initial(wl,3) = Rpao;
Initial(wl,4) = Rsao;

%Define Z equation 3.18

nO = (EpsO - (sin(Theta))^2)^.5;

lamda = a(wl,8);
```

```
Z = exp((4*3.14159*i*nO*d)/(lamda));

Initial(wl,5) = Z;

%Define phi complex angle

phi1 = a(wl,9);
phi2 = a(wl,10);

Phi1 = phi1 * sin(Theta);
Phi2 = phi2 * sin(Theta);

phi = complex(Phi1,Phi2);

Initial(wl,6) = phi;

%Calculate Rposa and Rsosa

Rposa = ((EpsO*((eps1c+(eps2c*i)) - (sin(phi))^2)^.5) -
((((x1+(x2*i))*(eps1c+(eps2c*i)))^.5)*(EpsO - (sin(Theta))^2)^.5))/((EpsO*((eps1c+(eps2c*i)) -
(sin(phi))^2)^.5) + ((((x1+(x2*i))*(eps1c+(eps2c*i)))^.5)*(EpsO - (sin(Theta))^2)^.5));
Rsosa = (((EpsO - (sin(Theta))^2)^.5) - (((eps1b+(eps2b*i)) - (sin(phi))^2)^.5))/(((EpsO -
(sin(Theta))^2)^.5) + (((eps1b+(eps2b*i)) - (sin(phi))^2)^.5));

b = (((Z*Rposa) + Rpao)*((Z*Rsao*Rsosa) + 1))/(((Z*Rpao*Rposa)+1)*((Z*Rsosa) + Rsao));

%end
Initial
```

```
function b = overlayerall6_var(p,wl,a)
y1 = p(1);
y2 = p(2);

Theta = 70*3.14159/180;
d = 12.71;


Initial = ones(16,6)


%Define overlayer complex dielectric function

eps1a = a(wl,11);
eps2a = a(wl,12);

eps1c = a(wl,15);
eps2c = a(wl,16);

epsO1 = a(wl, 2);
epsO2 = a(wl, 3);

EpsO = complex(epsO1,epsO2);

Initial(wl,1) = a(wl,1);
Initial(wl,2) = EpsO;

%Define Ambient/Overlayer Reflection Coefficents

Rpao1 = a(wl,4);
Rpao2 = a(wl,5);
Rsao1 = a(wl,6);
Rsao2 = a(wl,7);

Rpao = complex(Rpao1,Rpao2);
Rsao = complex(Rsao1,Rsao2);

Initial(wl,3) = Rpao;
Initial(wl,4) = Rsao;

%Define Z equation 3.18

nO = (EpsO - (sin(Theta))^2)^.5;

lamda = a(wl,8);
```

```
Z = exp((4*3.14159*i*nO*d)/(lamda));

Initial(wl,5) = Z;

%Define phi complex angle

phi1 = a(wl,9);
phi2 = a(wl,10);

Phi1 = phi1 * sin(Theta);
Phi2 = phi2 * sin(Theta);

phi = complex(Phi1,Phi2);

Initial(wl,6) = phi;

Rposb = ((EpsO*((eps1c+(eps2c*i)) - (sin(phi))^2)^.5) -
((((eps1a+(eps2a*i))*(eps1c+(eps2c*i)))^.5)*(EpsO -
(sin(Theta))^2)^.5))/((EpsO*((eps1c+(eps2c*i)) - (sin(phi))^2)^.5) +
((((eps1a+(eps2a*i))*(eps1c+(eps2c*i)))^.5)*(EpsO - (sin(Theta))^2)^.5));
Rsosb = (((EpsO - (sin(Theta))^2)^.5) - (((y1+(y2*i)) - (sin(phi))^2)^.5))/(((EpsO -
(sin(Theta))^2)^.5) + (((y1+(y2*i)) - (sin(phi))^2)^.5));

b = (((Z*Rposb) + Rpao)*((Z*Rsao*Rsosb) + 1))/(((Z*Rpao*Rposb)+1)*((Z*Rsosb) + Rsao));

%end
Initial
```

```
function b = overlayerall7_var(k,wl,a)
z1 = k(1);
z2 = k(2);

Theta = 70*3.14159/180;
d = 12.71;


Initial = ones(16,6)


%Define overlayer complex dielectric function

eps1a = a(wl,11);
eps2a = a(wl,12);

eps1b = a(wl,13);
eps2b = a(wl,14);

epsO1 = a(wl, 2);
epsO2 = a(wl, 3);

EpsO = complex(epsO1,epsO2);

Initial(wl,1) = a(wl,1);
Initial(wl,2) = EpsO;

%Define Ambient/Overlayer Reflection Coefficents

Rpao1 = a(wl,4);
Rpao2 = a(wl,5);
Rsao1 = a(wl,6);
Rsao2 = a(wl,7);

Rpao = complex(Rpao1,Rpao2);
Rsao = complex(Rsao1,Rsao2);

Initial(wl,3) = Rpao;
Initial(wl,4) = Rsao;

%Define Z equation 3.18

nO = (EpsO - (sin(Theta))^2)^.5;
```

```
lamda = a(wl,8);

Z = exp((4*3.14159*i*nO*d)/(lamda));

Initial(wl,5) = Z;

%Define phi complex angle

phi1 = a(wl,9);
phi2 = a(wl,10);

Phi1 = phi1 * sin(Theta);
Phi2 = phi2 * sin(Theta);

phi = complex(Phi1,Phi2);

Initial(wl,6) = phi;

Rposc = ((EpsO*((z1+(z2*i)) - (sin(phi))^2)^.5) - ((((z1+(z2*i))*(eps1a+(eps2a*i)))^.5)*(EpsO -
(sin(Theta))^2)^.5))/((EpsO*((z1+(z2*i)) - (sin(phi))^2)^.5) +
((((z1+(z2*i))*(eps1a+(eps2a*i)))^.5)*(EpsO - (sin(Theta))^2)^.5));
Rsosc = (((EpsO - (sin(Theta))^2)^.5) - (((eps1b+(eps2b*i)) - (sin(phi))^2)^.5))/(((EpsO -
(sin(Theta))^2)^.5) + (((eps1b+(eps2b*i)) - (sin(phi))^2)^.5));

b = (((Z*Rposc) + Rpao)*((Z*Rsao*Rsosc) + 1))/(((Z*Rpao*Rposc)+1)*((Z*Rsosc) + Rsao));

%end
Initial
```

```
%First import excel file with: col(1) = energy, col(2) = esp1, col(3) =
%esp2, col(4) = Re(Rpao), col(5) = Im(Rpao), col(6) = Re(Rsao),
%col(7) = Im(Rsao), col(8) = Wavelength, col(9) = Re(phi), col(10) =
%Im(phi), col(11) = esp1a, col(12) = eps2a, col(13) = eps1b, col(14) =
%eps2b, col(15) = eps1c, col(16) = eps2c

[a,descr] = xlsfinfo('DyScO3_overlayer.xls')

a = xlsread('DyScO3_overlayer.xls')

Final = ones(161,6)

for wl = 1:161
%determine initial guess for Epsa,Epsb,Epsc from Filmwizard file

eps1a = a(wl,11);
eps2a = a(wl,12);

eps1b = a(wl,13);
eps2b = a(wl,14);

eps1c = a(wl,15);
eps2c = a(wl,16);

for i = 1:6

v = [eps1a eps2a];
Final(wl,1:2) = fminsearch(@(v) overlayerall5_var(v,wl,a),v)
a(wl,11) = eps1a;
a(wl,12) = eps2a;

p = [eps1b eps2b];
Final(wl,3:4) = fminsearch(@(p) overlayerall6_var(p,wl,a),p)
a(wl,13) = eps1b;
a(wl,14) = eps2b;

k = [eps1c eps2c];
Final(wl,5:6) = fminsearch(@(k) overlayerall7_var(k,wl,a),k)
a(wl,15) = eps1c;
a(wl,16) = eps2c;

end
end
```